# Transduction and feedback regulation in morphodynamic signaling networks

**Dissertation**

zur Erlangung des akademischen Grades Doktor der Naturwissenschaften (Dr. rer. nat.) an der Fakultät Chemie und Chemische Biologie der Technischen Universität Dortmund

vorgelegt von

**Carolin Gierse**

[redacted]

im November 2025 in Dortmund

technische universität dortmund

IMPRS for Living Matter
INTERNATIONAL MAX PLANCK RESEARCH SCHOOL

The work presented in this thesis was performed from October 2021 to November 2025 in the laboratory of Priv.-Doz. Dr. Leif Dehmelt, at the Faculty of Chemistry and Chemical Biology, TU Dortmund University, Germany.

In the context of this work, the Bachelor thesis of Jennifer Hanemann was conducted. Corresponding sections were marked accordingly.

Fist Examiner: Priv.-Doz. Dr. Leif Dehmelt, TU Dortmund

Second Examiner: Prof. Dr. Britta Trappmann, TU Dortmund

# Publications

Results presented in this thesis contributed to the following publications:

Gierse, C., J. Hanemann, and L. Dehmelt. 2025a. Non-muscle Myosin II acts as a negative feedback mediator to control cell contraction dynamics. bioRxiv https://doi.org/10.1101/2025.09.12.675762

Gierse, C., I. R. Vetter, and L. Dehmelt. 2025b. The ROCK1 PHC1 domain interacts with active Rho to transduce cell contraction signals. bioRxiv https://doi.org/10.1101/2025.09.12.675761

Schmitt, C., Mauker, P., Vepřek, N.A., Gierse, C., Meiring, J.C.M., Kuch, J., Akhmanova, A., Dehmelt, L., and Thorn-Seshold, O. (2024). A Photocaged Microtubule-Stabilising Epothilone Allows Spatiotemporal Control of Cytoskeletal Dynamics. Angewandte Chemie (International ed. in English) *63,* e202410169. 10.1002/anie.202410169. https://onlinelibrary.wiley.com/doi/10.1002/anie.202410169

# Acknowledgement

I would like to start by saying a huge thank you to Leif, my supervisor and mentor during my PhD. You quickly recognized that I enjoy working independently and with a lot of enthusiasm. That's why you were able to support me in my ideas, conclusions, and new projects in such a way that I was able to develop myself further and quickly develop my independence. I am extremely grateful that you helped me immediately whenever I was stuck and stood by me with your years of expertise. Working in your lab taught me a lot and was also a lot of fun. Thank you very much.

Next, I would like to thank Prof. Trappmann. Thank you very much for immediately accepting the role of my second examiner and for now reviewing my work.

I would also like to thank my Thesis Advisory Committee (TAC) members Prof. Peter Bieling and Prof. Rudolf Merkel for giving very constructive feedback.

And, of course, I would like to thank my colleagues! Special thanks to Arya and Ricarda, who made my time here wonderful. Even during very stressful times, we managed to support each other and continue to laugh a lot together. We also always discussed our projects together and looked for solutions when one of us got stuck. Luisa, you supported us all greatly. Before you, Daria did your job, and I would like to thank you both. You both managed and organized the lab and thereby greatly supported us in our workflows. At the end of my PhD journey, Lara is now taking over this role, and I can already tell that you will do a great job, too. Thank you. I would also like to thank you, Ric, Arya, and Luisa, for the great cooking evenings outside of our working hours. Together, we really enjoyed some delicious meals! I hope that we will stay in touch after graduation.

I would also like to express my gratitude to Jenni. You were an outstanding Bachelor's student with enthusiasm and a passion for your work. Thank you very much.

I would also like to express my heartfelt thanks to the Summerer lab. Having lunch with you, celebrating birthdays and graduations has been a great pleasure for me. I am glad to have gotten to know each and every one of you. All those who have already graduated have more than earned their degrees, and I wish all the others only the best and, of course, a successful completion of their doctorates.

Another thanks you goes to Peri and her entire lab. Not only did we have great discussions during our joint lab meetings, but we also spent some very enjoyable afternoons and evenings barbecuing together.

I thank Anja Biesemann (TU Dortmund) who generated the PtK1 cell line stably expressing GFP-tubulin and Suchet and Dominic for helping me to get started in the lab.

I would also like to thank Department II at MPI. I completed my Bachelor's and Master's theses in Christian's lab and had the opportunity to meet some great people, especially those in Christian's and Peter's subgroups. I was still part of Department II during my first year of my PhD. Some of you have become friends with whom I keep in touch even after my time at Department II. Thank you.

I would like to take this opportunity to thank my friends and family from the bottom of my heart. Not only did you stick with me during the good times, you also always listened to my complaints. At the top of the list, of course, is my partner Kai. Thank you so much for your active support, both mentally and by taking on more household tasks than you should have had to while I was writing my thesis and the accompanying publications.

My sister Quiche also always supported me energetically, encouraged me, and even sent me groceries once so that Kai and I would have less to do. Thank you, sis. And my brother-in-law Paul and, above all, their two super cute sons always gave me a mental boost. Thank you. But of course, my mother and my other sister Esa also supported me. Here, too, I was always able to share my complaints, but also my moments of joy. Thank you.

Now, my best friends, Tati and Jana, and Isa. You have ensured that I take time for myself and you and don't completely overwork myself. Thank you. To us remaining friends for life.

And my final, very personal thanks go to my fellow students. Especially the "Harter Kern" consisting of Kim, Britta, Jan, Jens, Hannes, Niko, and Sarah. Without you, my studies would have been a lot less fun and also a lot more difficult for me. Thank you for continuing to be such good friends and supporting each other. Hopefully, we will never lose touch and remain part of each other's lives.

# 1 Contents

# Zusammenfassung

Viele grundlegende Prozesse in der Funktion von Zellen und Geweben hängen von dynamischen Veränderungen der Zellform ab. Beispielsweise müssen einzelne Zellen Änderung in ihrer Form während der Gewebemorphogenese oder der gerichteten Migration in der Immunantwort koordinieren. Diese Prozesse müssen räumlich und zeitlich eng aufeinander abgestimmt sein. Fehler bei der Koordination von Zellformänderungen können zu schweren Erkrankungen wie Krebsmetastasen beitragen. Zellen erzeugen dynamische Formänderungen durch intrazelluläre Kräfte, welche entweder zu Kontraktionen oder zu Ausstülpungen der Zellmembran führen können. Außerdem können Zellen Kontraktionskräfte nutzen, um mechanische Eigenschaften ihrer Umgebung zu erfassen. Dieser Prozess wird als Mechanotransduktion bezeichnet.

In früheren Studien wurde bereits ein Signalnetzwerk identifiziert, welches an diesem Prozess beteiligt ist und welches hochdynamische, mechanosensitive Kontraktionspulse erzeugt. Diese Kontraktionspulse werden durch oszillierende Signalnetzwerkdynamiken des Zellkontraktionsregulators Rho angetrieben. Rho ist eine kleine GTPase, welche die Bildung kontraktiler Zytoskelettstrukturen stimuliert. Diese Strukturen bestehen aus Aktinfilamenten, die durch den molekularen Motor non-muscle Myosin II intermolekular vernetzt sind. Die oszillierenden Netzwerkdynamiken entstehen aus einer Kombination von schneller positiver und langsamer negativer Rückkopplungsregulation von Rho. Die positive Rückkopplung ist bereits gut verstanden, der genaue Mechanismus der negativen Rückkopplung ist jedoch noch unklar. Frühere Studien legen nahe, dass diese Rückkopplung über einen relativ langsamen Prozess vermittelt wird, an dem kontraktile Aktin- und Myosin-basierte Strukturen oder hiermit assoziierte Proteine beteiligt sind. Das primäre Ziel dieser Arbeit war es, diesen Mechanismus genauer zu untersuchen. Im ersten Schritt wurden numerische Simulationen eines vereinfachten quantitativen Modells des oszillierenden Signalnetzwerks durchgeführt. Diese sagten voraus, dass die Dynamik der Zellkontraktionssignale durch die konstitutive Aktivierung von Myosin II stark gehemmt wird. Diese Vorhersage wurde experimentell durch die konstante Aktivierung von Myosin II durch Überexpression einer konstitutiv aktiven Mutante des Myosin-II-Aktivators Rho-assoziierte Coiled-Coil-Kinase 1 (ROCK1) bestätigt. Darüber hinaus führte eine lichtinduzierte schnelle Rekrutierung von ROCK1 an die

Plasmamembran zu einer starken Anreicherung von Myosin II an der Plasmamembran und überraschenderweise auch zu einer Verringerung von Aktin. Diese Veränderung im Verhältnis von Myosin II zu Aktin führte zu einer Hemmung der basalen und dynamischen Rho-Aktivität an der Plasmamembran. Dies zeigt eindeutig, dass Myosin II oder Myosin II assoziierte Proteine - und nicht Aktin - als Rho Inhibitor und Vermittler der negativen Rückkopplungsregulation in adhärenten Säugetierzellen wirkt.

Die Entwicklung der lichtinduzierten schnellen Rekrutierung von ROCK1 an die Plasmamembran wurde zunächst durch unerwartete Beobachtungen erschwert, die darauf hindeuteten, dass der Mechanismus der ROCK1-Regulierung komplexer war als ursprünglich angenommen. Durch eine detaillierte Analyse des molekularen Mechanismus der Aktivierung von Myosin durch ROCK, wurde eine neue Rho-Bindungsstelle am C-Terminus von ROCK1 innerhalb seiner PHC1-Domäne identifiziert. Diese Domäne allein ist ausreichend, um ROCK1 in Bereiche des Zellkortex mit erhöhter Rho-Aktivität zu rekrutieren. Mutagenese basierend auf AlphaFold2-Vorhersagen deuten auf eine direkte Wechselwirkung zwischen der PHC1-Domäne und Rho hin. Funktionelle Untersuchungen zeigten, dass die PHC1-Domäne für eine effiziente Rekrutierung von ROCK zu aktivem Rho unverzichtbar ist und dass sie zur Transduktion der Rho-Aktivität auf Myosin durch ROCK1 beiträgt. Die neu identifizierte Rho-Bindungsstelle am C-Terminus von ROCK1 liefert neue Erkenntnisse über den Mechanismus der ROCK1-Aktivierung und kann Widersprüche auflösen, die zwischen früheren biochemischen und strukturellen Studien beobachtet wurden.

Zusammenfassend lässt sich sagen, dass neue Mechanismen identifiziert wurde, welche die negative Rückkopplungsregulation im Zellkontraktionsnetzwerk vermitteln und die Transduktion von Rho-Signalen zur Myosin-Aktivierung durch ROCK1 detaillierter beschreiben. Diese Arbeit liefert somit neue Perspektiven auf den grundlegenden Prozess der Zellkontraktion und dessen Regulation und kann dadurch zu einem besseren Verständnis biologischer Prozesse beitragen, die von Zellkontraktion abhängig sind, wie beispielsweise die Zellmigration oder die Gewebemorphogenese.

# Abstract

Many fundamental processes in the function of cells and tissues are dependent on dynamic cell shape changes. For example, individual cells must coordinate changes in their shape during tissue morphogenesis or during directional migration in the immune response. These processes have to be coordinated tightly in space and time, and failures in this coordination can contribute to serious diseases, such as cancer metastasis. Dynamic cell shape changes are based on forces that are generated by cells that can either lead to contractions or protrusions of the plasma membrane. Conversely, cells can use contractile forces to sense mechanical properties of their environment in a process that is called mechanotransduction.

Previous studies identified a signaling network involved in this process that generates highly dynamic, mechanosensitive contraction pulses. These contraction pulses are driven by oscillatory signal network dynamics of the cell contraction master regulator Rho. Rho is a small GTPase signaling molecule that is well known to stimulate the generation of contractile cytoskeletal structures that are composed of cytoskeletal actin filaments, which are crosslinked by the molecular motor non-muscle Myosin II. The oscillatory signal network dynamics emerge from a combination of rapid positive and slow negative feedback regulation of Rho. The rapid positive feedback is already well understood, however, the exact mechanism, how negative feedback is mediated is still unclear. Previous studies suggest that negative feedback regulation is mediated via a relatively slow process that involves contractile actin- and Myosin-based structures, or proteins that are associated with these components. The primary objective of this thesis was to investigate this mechanism in more detail. In the first step, numerical simulations of a simplified quantitative model of the oscillatory signal network predicted that the dynamics of cell contraction signals are strongly inhibited by constitutive activation of Myosin II. This prediction was experimentally confirmed by the constant activation of Myosin II by over-expression of a constitutively active mutant of the Myosin II activator Rho associated coiled-coil kinase 1 (ROCK1). In addition, a light-induced rapid plasma membrane recruitment of the Myosin II activator ROCK1 induced a strong accumulation of Myosin II at the plasma membrane, and surprisingly also lead to a reduction of actin. This change in the relative abundance of Myosin II vs actin resulted in the inhibition of basal and dynamic Rho activity at the plasma membrane. This clearly shows that Myosin II

or Myosin II associated proteins and not actin act as a Rho inhibitor and negative feedback mediator in adherent mammalian cells.

The development of the light-induced rapid plasma membrane recruitment of ROCK1 was initially hampered by unexpected observations that suggested that the mechanism of ROCK1 regulation was more complex than originally anticipated. A detailed analysis of the molecular mechanism by which ROCK1 activates Myosin, revealed a novel Rho binding site at the extreme C-terminus of ROCK1 within its PHC1 domain. This domain was sufficient to recruit ROCK1 to regions of the cell cortex exhibiting increased Rho activity. Mutagenesis guided by AlphaFold2 predictions supports a direct interaction between the PHC1 domain and Rho. Functional investigations demonstrated that the PHC1 domain is indispensable for effective recruitment to active Rho, and that it contributes to the transduction of Rho activity through ROCK1 leading to Myosin II activation. The newly identified Rho binding site at the ROCK1 C-terminus provides novel insights into the mechanism of ROCK1 activation, and it can resolve inconsistencies that were observed between prior biochemical and structural studies.

In conclusion, a Myosin II dependent process was identified that mediate negative feedback regulation in the cell contraction network, and novel insights into the regulation of ROCK1 and its mechanism of transducing Rho signals to Myosin II were uncovered. This thesis therefore provides new perspectives on the fundamental process of cell contraction and its regulation and thereby can help to gain a better understanding of the biological processes that are dependent on cell contraction, such as cell migration or tissue morphogenesis.

# List of abbreviations

| Abbreviation | Meaning | Abbreviation | Meaning |
|---|---|---|---|
| **ΔCAAX** | deleted CAAX motif in protein with C mutated to S | **M** | molar |
| **$\Delta^{PHC1}$** | PHC1 deletion mutant of ROCK1 | **Myosin (II)** | non-muscle Myosin II |
| **ΔRnd3** | S288R, N292D mutant of ROCK1 | **m** | slope |
| **°C** | degrees Celsius | **m** | mili |
| **µ** | micro | **MA** | Mass action |
| **10S** | inactive, folded Myosin II conformation | **MAP** | Molecular Activity Painting |
| **6S** | active, extended Myosin II conformation | **min** | minute(s) |
| **a.u.** | arbitrary unit | **MLCK** | Myosin light chain kinase |
| **ADF** | actin depolymerizing factors | **mm** | milimeter |
| **ADP** | adenosine diphosphate | **MRCK** | myotonic dystrophy kinase-related Cdc42-binding kinase |
| **Arp2/3** | actin-related-protein 2/3 | **mutAPH** | A1291R ROCK1 mutant |
| **ATP** | adenosine triphosphate | **mutBPH** | F1174A, L1199A, E1203K ROCK1 mutant |
| **bp** | base pairs | **mutCPH** | A1291R, F1174A, L1199A, E1203K ROCK1 mutant |
| **C1** | cysteine-rich zinc finger-like motif 1 | **mutRBD** | Asn1004Tyr, Lys1005Tyr mutant of ROCK1 |
| **CA** | constitutively active | **Myo9b** | Myosin9b |
| **CAAX** | C: Cysteine, A: aliphatic amino acids, X: random amino acid | **Myosin II** | non-muscle Myosin II |
| **CA-MAP** | Cell Adhesion Area - MAP | **n** | nano |
| **Cdc42** | Cell division cycle 42, small RhoGTPase | **nm** | nanometer |
| **CFP** | cyan fluorescent protein | **NMHC** | non-muscle Myosin heavy chain |
| **CMV** | cytomegalovirus | **Nvoc-TMP-Cl** | 6-nitroveratroyloxycarbonyl |
| **CouEpo** | Cou-epothilone (C7 caged Epothilione) | **ODE** | ordinary differential equations |

| | | | |
|---|---|---|---|
| **Da** | Dalton | **p190RhoGAP** | p190 Rho GTPase-activating protein |
| **Dbl GEF** | diffuse B-cell lymphoma GEF | **PA** | photo-activation |
| **dd** | double distilled | **PCR** | Polymerase chain reaction |
| **delCMV** | deleted CMV | **PH** | Pleckstrin homology |
| **DH** | Dbl homology | **PHC1** | PH + C1 tandem domain of ROCK1 |
| **Dia** | diaphanous | **Pi** | Phosphate |
| **(dimerizer-)PARC** | (dimerizer-) presenting artificial receptor constructs | **PIP** | phosphatidylinositol phosphates |
| **DMEM** | Dulbecco's modified eagle's medium | **PISA** | Protein Interfaces, Surfaces and Assemblies |
| **DMSO** | dimethyl sulfoxide | **POI** | protein of interest |
| **DNA** | Desoxyribonucleic acid | **prefix d** | dimeric |
| **DPBS** | Dulbecco's phosphate-buffered saline | **prefix m** | monomeric |
| **E** | Enzymatic | **Ptk1** | Potorous tridactylus kidney epithelial cells |
| **E.** | Escherichia | **R** | Rho |
| **e.g.** | exempli gratia | **r** | Pearson correlation coefficient |
| **eDHFR** | Escherichia coli dihydrofolate reductase | **Rac** | Ras-related C3 botulinum toxin substrate |
| **EDTA** | ethylene diamine tetraacetic acid | **RBD** | Rho binding domain |
| **ELC** | essential light chain | **Rev** | Reverse |
| **EMC** | Extracellular matrix | **RGA3/4** | Rho GTPase-Activating Protein 3 and 4 |
| **F-actin** | Filamentous actin | **Rho (small) GTPases** | Rho family of small GTPases |
| **FBS** | fetal bovine serum | **RhoA** | Ras homolog family member A |
| **FHOD** | formin-homology domain | **RID** | Rho-interacting domain |
| **FRET** | Fluorescence resonance energy transfer | **RLC** | Regulatory light chain |
| **Fwd** | Forward | **Rnd3** | Rho Family GTPase 3 |

| | | | |
|---|---|---|---|
| **G** | GEF-H1 | **ROCK** | Rho-associated coiled-coil containing protein kinase |
| **GAP** | GTPase-activating protein | **ROI** | region of interest |
| **GBD** | GTPase-binding domain | **Rok** | ROCK homologue in Drosophila |
| **GDI** | GTP-dissociation inhibitor | **rpm** | revolutions per minute |
| **GDP** | guanosine diphosphate | **rt** | room temperature |
| **GEF** | GTP-exchange factor | **S** | Serine |
| **GFP** | Green Fluorescent Protein | **s** | second(s) |
| **GTP** | Guanosine-triphosphate | **SBD** | Shroom-binding domain |
| **GTPases** | GTP hydrolysing proteins | **SD** | standard deviation |
| **h** | hour(s) | **SDE** | stochastic differential equations |
| **H2O** | Water | **SEM** | standard error of the mean |
| **HaloTag** | HaloTag protein tag (modified haloalkane dehalogenase) | **SLF-TMP** | Synthetic Ligand for FKBP - Trimethoprim |
| **HEPES** | 4-(2-hydroxyethyl)-1-piperazineethanesulfonic acid | **SOC** | Super Optimal broth with Catabolite repression |
| **HR1** | homology region 1 | **t** | Time |
| **ipTM** | interface predicted template modeling score | **TIRF** | total internal reflection fluorescence |
| **k** | kilo | **U** | enzyme unit |
| **k** | rate constant | **U2OS** | Uppsala 2 - Osteosarcoma |
| **kb** | kilo base pairs | **UV** | ultra violet |
| **Km** | Michaelis constant | **wt** | wild type |
| **l** | liter | **Y27632** | ROCK inhibitor |
| **LB** | Luria-Bertani | **YFP** | Yellow fluorescent protein |
| **LOV2** | light-oxygen-voltage-sensing 2 | **Zdk1** | Z dark-keeper 1 |
| **LOVTRAP** | light-oxygen-voltage-sensing 2 domain TRAPing method | **ZK-Epo** | ZK-epothilone |

# 1 Introduction

## 1.1 Cellular information processing by signaling networks

All cells, both in higher organisms and unicellular organisms, must interpret information presented by their environment in conjunction with intracellular processes. The extracellular inputs may be chemical or physical in nature and can originate from the extracellular matrix or from other cells. These inputs are typically sensed by transmembrane receptors that connect the extracellular and intracellular space and then processed by intracellular signaling systems (Grecco et al., 2011).

Classically, cellular signal transduction is often visualized as a linear process, in which external signals are communicated along a linear pathway (Seger and Krebs, 1995). However, it is now well-established that such linear pathways are insufficient to explain most aspects of cellular information processing (Saez-Rodriguez et al., 2015). Instead, signals received by cells are integrated and processed by highly interconnected signaling networks, that include non-linear causalities, such as positive and negative feedback loops (Bray, 1995; Ferrell, 2002; Chen et al., 2010)

Such non-linear signaling networks can process input signals to generate diverse output signals. The dynamics of such outputs can even be spontaneously and autonomously generated, for example as regular oscillations in the absence of external inputs (Tyson et al., 2003). To achieve this, a relatively small number of interlinked components is sufficient, as it was shown in reconstituted, synthetic dynamic signal systems (Elowitz and Leibler, 2000). Due to their non-linear causalities, it is often difficult to intuitively predict or understand the function of such interlinked signaling networks. For example, the same network of signal proteins can generate qualitatively distinct output dynamics, if only the rate constant of one reaction is altered (Tyson et al., 2003; Mangan and Alon, 2003; Novák and Tyson, 2008). To investigate such networks, it is very useful to describe them by mathematical models, for example using ordinary differential equations (ODEs), that are based on the underlying biochemical reactions. Mathematical analysis and numerical simulations based on these equations can be used to predict the dynamics of signal outputs of such networks, and how

they are influenced by changes in their parameters or changes in signal inputs (Bray, 1995; Novák and Tyson, 2008).

To develop a model based on ODEs, it is essential to understand how signals are transduced between the different components of the signal network (Bray, 1995; Tyson et al., 2003; Novák and Tyson, 2008; Chen et al., 2010). This can be achieved by examining how a perturbation in one component of a signal network is propagated to other signal network components. To directly extract meaningful information from interconnected, non-linear signal networks, it is essential, that the perturbation and response readouts occur at a similar or faster timescale compared to the signal processing events of the network (Kamps and Dehmelt, 2017). Otherwise, rapid adaptation dynamics in the signal network can be overlooked, which might provide the most critical information about signal processing. Experimental investigations of such perturbation-response relationships can be used to construct hypothetical network topologies and ODE-based mathematical models, which can then be validated by comparing their predictions with further experiments (Bray, 1995; Novák and Tyson, 2008).

### 1.1.1 Activity dynamics in networks with feedback loops

An interesting feature of many signaling networks is feedback. In signal networks, feedback is based on a closed loop, in which the output feeds back to influence its own cause. Feedback loops are primarily distinguished based on the sign of the loop, i.e. positive or negative (UMBARGER, 1961; Tyson et al., 2003; Novák and Tyson, 2008). Conceptually, negative feedback can arise either through self-inhibition of a single component, or via the activation of an intermediate, inhibitory component (Figure 1A). This feedback typically leads to homeostasis, i.e. self-limiting regulation, which is often found in biosynthesis. In the example shown in Figure 1A (left), the activity of a signal network component A can activate another signal network component I, which in turn inhibits A. Figure 1A (right) also shows a simulation of such a system, in which negative feedback regulation drives the activity of A and I to a stable steady-state, even if the system is transiently perturbed (green arrow). If the negative feedback and the associated adaptation kinetics have a substantial time delay, such systems can also autonomously generate oscillating outputs (Novák and Tyson, 2008).

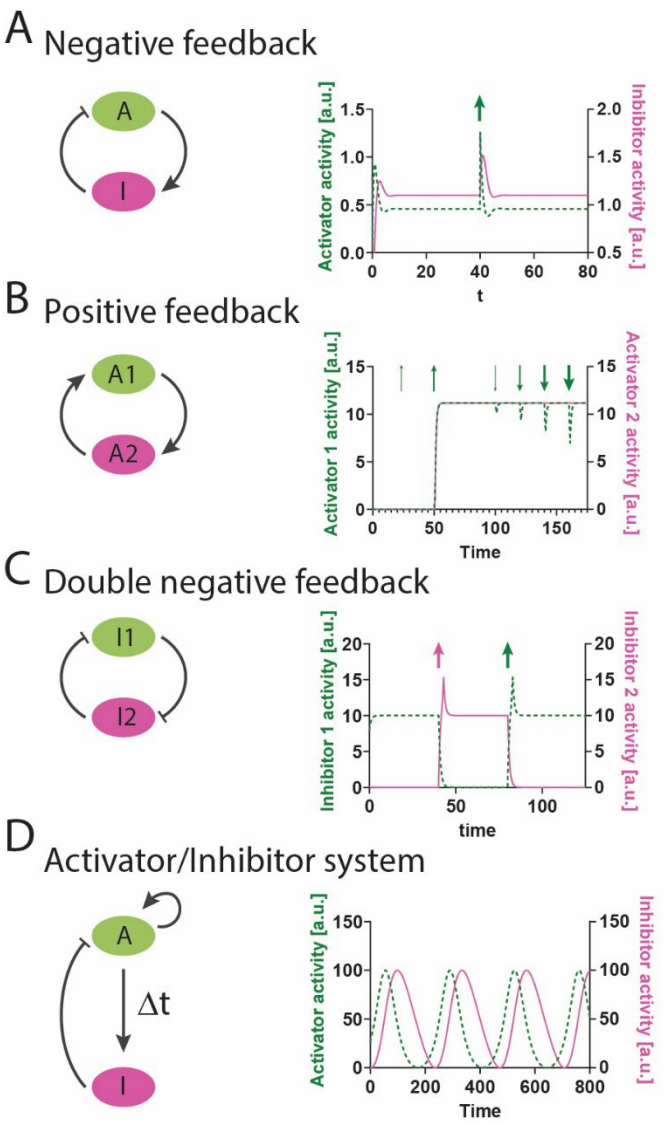


*Figure 1: Signal dynamics in networks that include feedback regulation. (A-D) Schematic depiction of distinct signal network topologies (left) and corresponding simulations of signal network dynamics and their response to external perturbations (right). (A) A simple negative feedback network topology that generates homeostasis. The activity states of the activator A and inhibitor I quickly develop into a stable steady-state. An externally introduced perturbation in either component (here in component A, marked by a green upward arrow) quickly goes back to steady-state levels. (B) Mutual activation between two-components. Even a small perturbation (green upwards arrows) can trigger an irreversible switch in the activity states of this system. After switching, even very strong perturbations in the opposite direction cannot switch this system off again (green downwards arrows). (C) Mutual inhibition between two-components or double negative feedback network motif. The signaling molecules in this system can reversibly switch between two distinct steady states. (D) Activator/Inhibitor network topology. Even in the absence of external signals, the activity of the components of such systems can oscillate autonomously. Numerical simulations shown in A-C were based on systems of ordinary differential equations (ODEs), which were computed using Python scripts, that were generated by chatGPT5. The simulation shown in D was based on a system of ODEs that will be described in more detail in section 1.3.5, and was computed using Matlab.*

Positive feedback can arise in several distinct ways: in the case of a single component via self-activation, or in the case of two components, via mutual activation (Figure 1B) or mutual inhibition (Figure 1C) (Tyson et al., 2003; Novák and Tyson, 2008). A typical property of such positive feedback systems is that they can generate discontinuous, switch-like activation responses (Figure 1B-C, right). For example, in mutual activation, the signal network component activator A1 can activate another signal network component A2, and reciprocally, A2 activates A1, closing a positive feedback loop (Figure 1B). The simulation of such a system shows that the components can amplify even a very small, transient perturbation. Once a certain activity threshold for such a perturbation is reached (slightly larger upwards green arrow), there is an abrupt increase in A1 and A2 activity. After their activation, A and B remain at their maximum level, and a perturbation of similar or higher strength is not sufficient to reverse this process to switch back to the initial conditions (see perturbations in simulation in Figure 1B right). Such irreversible switches in network activity are essential for many physiological processes that require a permanent change, such as during cell differentiation in development (Ferrell and Machleder, 1998; Cappell et al., 2016) or in controlled cell-death (Gülcüler Balta et al., 2019).

While mutual inhibition also generates positive feedback, the dynamics of these systems are quite different from those of systems with mutual activation. In the example shown in Figure 1C, a signal network component I1 inhibits another signal network component I2, and I2 reciprocally inhibits I1. The loop therefore corresponds to the inhibition of an inhibitor, which in combination has a positive effect, resulting in a positive feedback loop. However, the resulting system is bistable and generates the dynamics of a so-called toggle switch (Figure 1C, right). The system can exist either in a state where I1 is high, and I2 is low or vice versa. In contrast to the mutual activation, the system can be switched between these two states with a sufficiently large perturbation (Novák and Tyson, 2008). Such bistable systems that act like toggle switches play important roles in many contexts, for example in the regulation of the cell cycle (Ferrell and Ha, 2014), in stem cell differentiation (Stanoev et al., 2021) and in growth factor sensing (Stanoev et al., 2018).

In cells, signaling networks often include a larger number of interconnected components, which then can generate more complex dynamics. One motif that plays important roles in several cellular processes is the so-called activator/inhibitor network (Figure 1D), which is

based on interlinked positive and negative feedback loops. In the example shown in Figure 1D, a signal network component A rapidly amplifies its own activity and slowly activates its inhibitor I. Similar to a simple time delayed negative feedback, such systems can generate oscillations, however, these oscillations are typically more robust due to the efficient and rapid amplification in the coupled positive feedback loop. Such oscillatory activator/inhibitor networks are of great physiological importance, for example in circadian clocks (Dunlap, 1999; Hogenesch and Herzog, 2011) or the regulation of the eukaryotic cell cycle by oscillations of Cyclin-dependent kinases (Csikász-Nagy et al., 2006). Depending on the parameters of the underlying biochemical reactions, activator/inhibitor networks can also be excitable. Such systems are typically stable in their unperturbed, low activity state but are activated very strongly in a pulse-like fashion even via a small perturbation. Shortly after their activation they are typically insensitive to another stimulation for a short period of time ("refractory period"), until they go back to their initial, excitable state. Typical examples for excitability in biological systems are the propagation of action potentials in neurons, or in the heart muscle (HODGKIN and Huxley, 1952; NOBLE, 1962).

## 1.2 Generation and Regulation of Forces that Drive Cell Morphodynamics

Feedback-based signaling networks as those described above control many aspects of cellular function. A particular focus of this thesis was their role in controlling cell shape changes. Morphological changes at the level of individual cells are essential for many physiological processes. For example, they are necessary for wound healing (Alanko et al., 2023), embryonic development (Horwitz and Webb, 2003; Scarpa and Mayor, 2016), but also play a major role in pathophysiological processes such as cancer metastasis (Holle et al., 2019; Hanahan, 2022). Conceptually, cell shape changes can be broadly divided into two categories: cell protrusions, which push the cell edge forward, and retractions or contractions, which can pull back the cell or squeeze its environment (Nalbant and Dehmelt, 2018). Together, these processes of cell contraction and cell protrusion drive morphological changes in cell shape, which in turn can drive tissue rearrangements and cell migration (Cooper, 2000). Both cell protrusion and cell retraction are powered by dynamic rearrangements of specialized, filamentous structures that

are collectively called the cytoskeleton. In addition, the cytoskeleton can also confer structural stability to maintain and stabilize the shape of cells (Cooper, 2000; Wollrab et al., 2018).

### 1.2.1 Generation of pushing forces by polymerization of actin filaments

Cell protrusion is primarily driven by the directional polymerization of one specialized cytoskeletal component, which is called actin. Actin is an enzyme that can hydrolyze a bound adenosine triphosphate (ATP) molecule to adenosine diphosphate (ADP) and it can exist either in a monomeric, globular form (G-actin), or in a polymerized, filamentous form (F-actin) (Wegner, 1976).

Actin filaments are asymmetrical, with a helical twist and they have two structurally distinct filament ends that differ in their affinity for the addition of monomers. The polymerization of actin occurs predominantly at the so-called plus-end of an actin filament, where the binding of ATP-bound actin monomers is strongly preferred compared to ADP-bound monomers (Wegner, 1976). This polymerization-based extension is supported by profilin, which binds actin monomers and catalyzes the exchange of ADP to ATP (Carlsson et al., 1977). While the plus-end of an actin filament represents its growing end, the minus-end corresponds to the shrinking end of said filament. After their incorporation into filaments, ATP hydrolysis to ADP is stimulated, which results in filament destabilization (Wegner, 1976). Near the minus-end, actin binding proteins of the Cofilin and actin depolymerizing factor (ADF) families promote the disassembly and subsequent depolymerization of actin filaments (Carlier et al., 1997). The resulting combination of rapid polymerization and rapid depolymerization ensures that structures that are based on actin filaments can be highly dynamic and can be quickly rearranged within cells.

Such a dynamic rearrangement of actin structures is particularly important during rapid cell shape changes, for example during cell migration. In particular, at their leading edge, migrating cells form a specialized, flat, protrusive structure, the so-called lamellipodium, which is based on a branched network of actin filaments. This branched network is generated by the nucleation of new actin filaments on already existing filaments by the actin-related protein 2/3 (Arp2/3) complex. These new filaments collectively polymerize towards the cell edge and generate a polymerization force that pushes the cell membrane forward (Pollard and Borisy, 2003; Bieling and Rottner, 2023).

### 1.2.2 Generation of contractile forces by actomyosin

As described above, cell protrusion is driven by a force that is generated by the collective and directional polymerization of actin filaments. The retraction or contraction of the cell body is also driven by a mechanism that is dependent on actin filaments. However, this process is not driven by changing the length of individual filaments but rather driven by the action of a molecular motor, which is called Myosin II, and which can slide aligned arrays of multiple actin filaments towards opposite directions, effectively shorting these filament arrays (Spudich, 2001; Aguilar-Cuenca et al., 2014).

Myosin II is best known for its function in muscle cells, where it is organized together with actin filament arrays into specialized structures called sarcomeres (Adelstein et al., 1971). Within these structures, Myosin II is the molecular motor that generates the force that drives muscle contraction by shortening the actin filament arrays. Non-muscle cells can generate such contractile forces as well, however, the specialized non-muscle Myosin II isoforms (hereafter simply referred to as Myosin II or Myosin) form smaller structures that can re-localize more dynamically within cells (Adelstein et al., 1971; Aguilar-Cuenca et al., 2014).

Cells can form several distinct but related structures that are based on Myosin II and actin filaments, which are collectively referred to as actomyosin. These structures include a largely homogenous contractile layer below the plasma membrane, called the actin cortex (Truong Quang et al., 2021), more concentrated bundles of actomyosin called stress fibers (Hotulainen and Lappalainen, 2006) (Figure 2), the contractile lamella region that is found in more central cell areas next to lamellipodia (Ponti et al., 2004), and more specialized structures, such as the contractile ring that drives cell separation during cytokinesis (Matsumura, 2005).

On the molecular level, Myosin II is an ATP driven motor protein (Spudich, 2001). Each non-muscle Myosin II molecule is comprised of six subunits, including two heavy chains (non-muscle Myosin II heavy chain, NMHCII) that interact via their large, extended coiled-coil central domains, as well as two regulatory light chains (RLCs) and two essential light chains (ELCs).

The oligomerization of non-muscle Myosin II leads to the formation of antiparallel filaments (so-called mini-filaments, Figure 2B) that contain 28-30 hexamers (Niederman and Pollard, 1975; Billington et al., 2013). The formation of mini-filaments is only possible if Myosin II is in

the activated, extended (6S) conformation. In the inactive, folded (10S) conformation, the Myosin head and tail interact intramolecularly to prevent both filament assembly and F-actin association (Trybus et al., 1982; Ikebe, 2008). The conformational change from the 10S to the 6S form of Myosin depends on the phosphorylation of S19 on RLCs, which disrupts the head-tail interaction (Smith et al., 1983). Several kinases can phosphorylate S19 on RLC, in particular the Rho-associated protein kinase (ROCK), the Myosin light chain kinase (MLCK), and the myotonic dystrophy kinase-related Cdc42-binding kinase (MRCK) (Garrido-Casado et al., 2021). T18 phosphorylation has been shown to further increases Myosin II filament stability and ATPase activity (Ikebe, 2008; Vicente-Manzanares and Horwitz, 2010). The inactivation, or the conformational change from 6S to 10S, is facilitated by the dephosphorylation of the these residues by the protein phosphatase MYPT1 (Kimura et al., 1996).

Active Myosin head domains within mini-filaments bind to actin filaments and can generate a force by their motor activity. The force is generated by sequential steps in the activity state of the Myosin head domain: 1) ATP-bound Myosin has a very low affinity to actin and is therefore not associated with actin filaments. 2) The process of hydrolysis of the ATP to ADP+$P_i$ allows for the binding of the Myosin head to actin (Rayment et al., 1993). 3) The release of the phosphate ($P_i$) from the ATPase domain triggers a conformational change, exerting a force on the associated actin filament. 4) The cycle is closed as ADP is exchanged for ATP (Huxley, 1974).

Non-muscle Myosin is a so-called “non-processive” molecular motor, meaning that a single motor domain cannot produce a force on a single actin filament, as the motor domain would dissociate in step 1 of the sequence above. Effective force generation is only possible when multiple Myosin motors within a mini-filament act together on the associated actin filament (Sweeney and Houdusse, 2010). In typical actomyosin structures within cells, multiple actin filaments act together with multiple Myosin mini-filaments, to slide actin filaments with opposite orientation (i.e. “anti-parallel” orientation, see Figure 2B) against each other to produce a contractile force (Hotulainen and Lappalainen, 2006). In the example of stress fibers shown in Figure 2B, this process is similar to muscle contraction, and the overall structural organization of stress fibers is supported by additional molecules, in particular by the actin crosslinker alpha-actinin (Lazarides and Burridge, 1975; Hu et al., 2017). The resulting contractile force is oriented in the direction of these stress fibers, which are typically anchored to the extracellular space via specialized structures, called focal adhesions. Contraction of less

structured actomyosin, such as for example in the actin cortex, is also powered by Myosin II motors, but in contrast to stress fibers, the generated force is oriented more isotropic (Svitkina, 2020). This isotropic organization of contractile force is thought to be stabilized by various actin crosslinkers and by linking actin to the plasma membrane, for example via Ezrin-Radixin-Moesin (ERM) proteins (Chugh and Paluch, 2018).

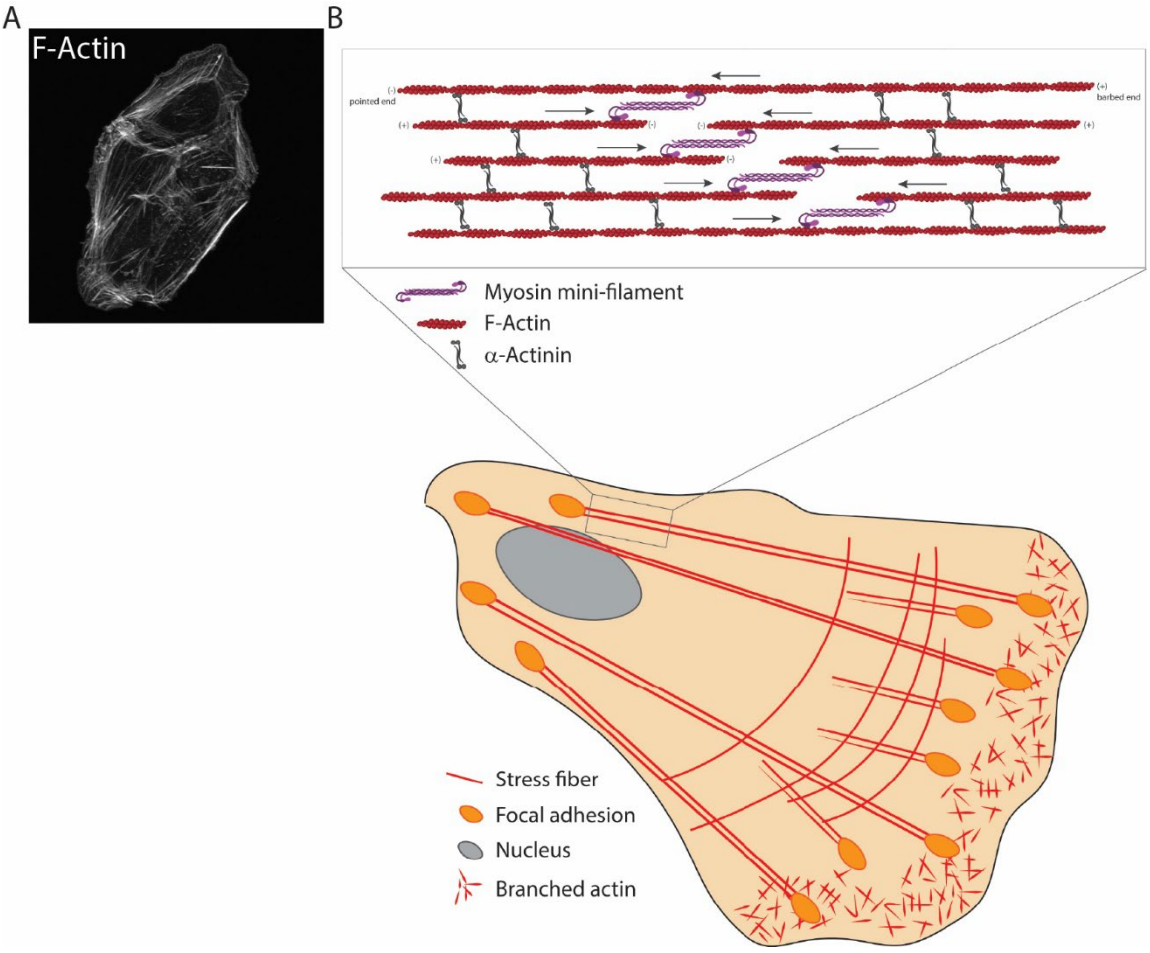


*Figure 2: Actin-base structures within cells. (A) Wildfield image of a fixed U2OS cell stained with phalloidin-Alexa488 (Milroy et al., 2012). (B) Schematic depiction of the most prominent actin-based structures in a typical migrating cell: contractile stress fibers, which are usually bound to focal adhesions, and the branched actin network within the lamellipodium which can generate a polymerization-based protrusive force. The magnified, detailed view of stress fibers illustrates their structural organization, with Actin filaments, non-muscle Myosin II mini-filaments (only two hexamers are shown for illustrative purposes), and α-Actinin crosslinkers.*

# Part I: Transduction and regulation of negative feedback in the cell contraction signaling network

## 1.3 Regulation of cell contraction by the small GTPase Rho

As previously mentioned, the cytoskeleton is highly dynamic in cells and these dynamics are the basis for cell shape changes, in particular cell protrusion and cell retraction. To perform higher order functions, such as directional cell migration, cells must regulate, organize and coordinate these shape changes in space and time. Cells achieve this via signal networks that locally control cytoskeletal dynamics in cells. The primary regulators of these dynamics are small GTPases, specifically the Rho family of small GTPases (Hodge and Ridley, 2016). The molecular weight of Rho small GTPases is approximately 21 kDa and they belong to the Ras superfamily of small GTPases. This superfamily consists of more than 150 different GTP-binding proteins in humans (Wennerberg et al., 2005), which act as key signal molecules in various important cellular processes. The G-domain of these proteins, which is also known as the GTP-binding domain, is located at the N-terminus, followed by the so-called switch I and switch II regions. Finally, each small GTPase has a hypervariable region at its C-terminus that is typically posttranslationally modified with a lipid anchor. In the Rho subfamily, the most common motif for lipidation is the C-terminal CAAX motif (C: Cysteine, A: aliphatic amino acids, X: random amino acid) (Schaefer et al., 2014). The subcellular localization of Rho GTPases is dependent on such lipid modifications, which are catalyzed by farnesyl and geranyl-geranyl transferases (Ridley, 2015). In combination with the predominantly positively charged hypervariable region, these lipidations are critical for anchoring Rho GTPases to cellular membranes, in particular the plasma membrane, where they can interact with their effectors (Michaelson et al., 2001).

Most members of the Rho family switch between an “on”, GTP-bound, and “off”, GDP-bound, state (Figure 3A). Two structural regions, the so-called switch I and switch II regions of the GTPase undergo a dramatic conformational change dependent on these states, which regulates their interaction with upstream and downstream signaling molecules. In the “on” state, Rho GTPases interact with so-called effectors, which by themselves can activate multiple downstream pathways.

Three classes of proteins are central for the control of the activity state of Rho GTPases (Figure 3A): Guanine-nucleotide exchange factors (GEFs) facilitate the exchange of GDP for GTP, thereby switching the small GTPase into the “on” state. In contrast, GTPase-activating proteins (GAPs) enhance the intrinsic GTPase activity of small GTPases, resulting in the hydrolysis of GTP to GDP, switching the small GTPase into the “off” state. Guanine-nucleotide dissociation inhibitors (GDIs) are a class of proteins that have an extensive hydrophobic pocket that can bind to the membrane anchor of small GTPases and thereby sequester these protein away from the plasma membrane into the cytosol (Buchsbaum, 2007; Ridley, 2011; Cherfils and Zeghouf, 2013).

The Rho GTPases RhoA, Rac1, and Cdc42 are the best characterized ones and play a crucial role in the regulation of the actin cytoskeleton (Hall, 1998). In the classical view, RhoA is associated with cell contraction signaling, namely stress fiber formation and focal adhesion assembly. It is well established that Rac1 is associated with the formation of lamellipodia, while Cdc42 regulates the formation of filopodia (Ridley, 2015).

However, it should be noted that not all small GTPases of the Rho family are subject to the same regulatory mechanisms. One exception is for example Rnd3 (also known as RhoE), an “atypical” Rho GTPase that is constitutively active (Ridley, 2011). Such a constitutively active form can also be enforced in the typical, canonical small GTPases by mutating a specific residue within the GTP binding pocket that results in loss of GTPase activity, e.g. Q63L for RhoA (Mayer et al., 1999). This method is frequently employed to investigate various aspects of small GTPases within cells.

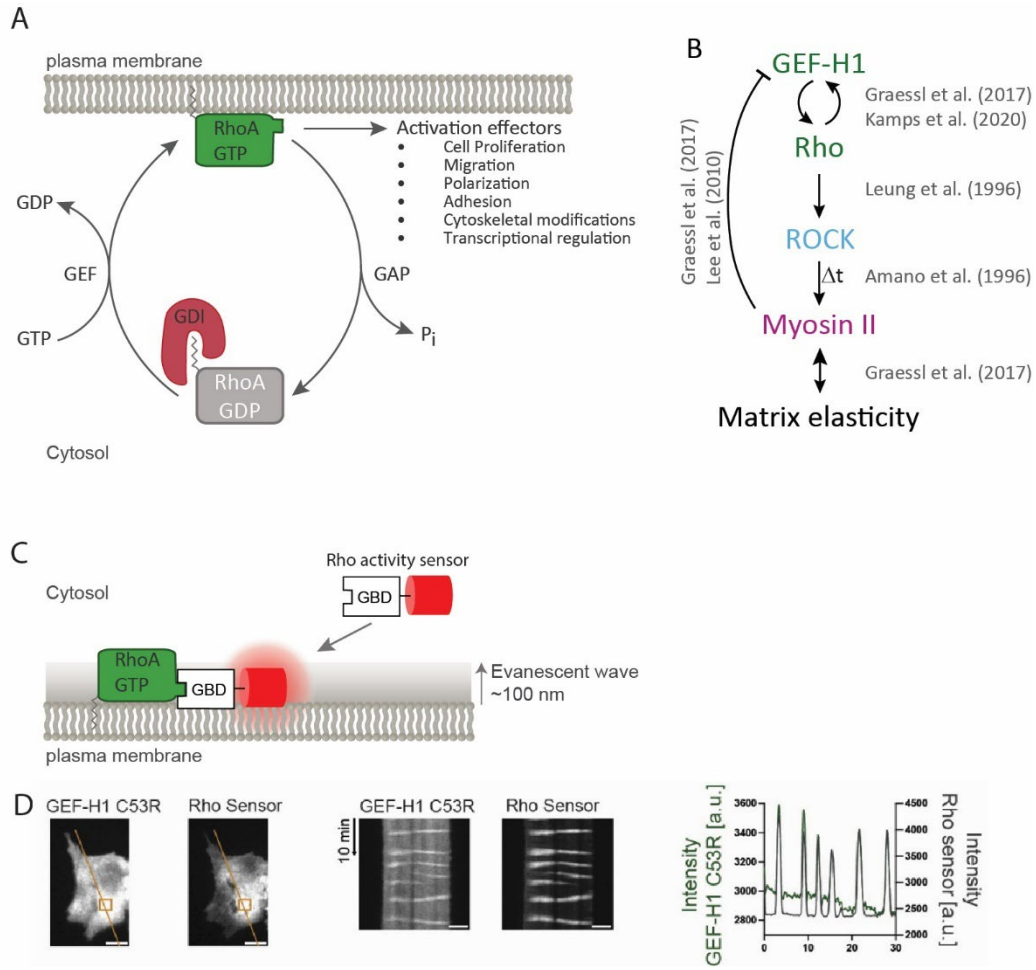


*Figure 3: Regulation of the small GTPase Rho and measurements of its activity. (A) In their active, GTP-bound form, canonical Rho GTPases such as RhoA are anchored at the plasma membrane via their C-terminal tails, which contain multiple positively charged residues that interact with the negatively changed plasma membrane headgroups, and a covalent, post-translational lipid anchor modification. At the plasma membrane, Rho GTPases can bind and activate effector proteins, which in turn activate several downstream signaling pathways. GTPase-activating proteins interact with the active, GTP bound form of Rho family proteins and increase their intrinsic GTPase activity. The resulting hydrolysis of GTP to GDP switches Rho proteins into their inactive, GDP bound form. Guanin-nucleotide dissociation inhibitors (GDIs) can bind to this inactive form and solubilize small Rho GTPases in the cytosol by binding to their lipid anchor with a hydrophobic pocket. Guanine-nucleotide exchange factors (GEFs) interact with the inactive, GDP bound form of Rho family proteins and activate them by catalyzing the exchange of GDP to GTP. This closes the regulatory cycle in the regulation of Rho family small GTPases. (B) Proposed cell contraction signal network topology based on Graessl et al. (2017) and Kamps et al. (2020). (C) Principle of Rho activity measurement via a translocation-based activity sensor. The sensor consists of a GTPase binding domain (GBD) that is linked to a fluorescence protein. The GBD only binds to the active, GTP bound form of the Rho GTPases, which is typically localized to the plasma membrane. The translocation of the sensor from the cytosol to the plasma membrane can be measured sensitively using total internal reflection fluorescence microscopy (TIRF-M). (D) GEF-H1 C53R plasma membrane translocation and Rho activity signals (mCitrine-Rhotekin GBD) are closely correlated in space and time at the plasma membrane. Left: Individual images obtained via TIRF microscopy of cells expressing the Rhotekin-based Rho activity sensor (mCitrine) and mApple-GEF-H1 C53R. Middle: Kymographs that represent the change in signal over time along the orange line in the TIRF images. Right: Intensity measurements from boxes in the TIRF images.*

### 1.3.1 Stimulation of Rho-dependent cell contraction by the guanine-nucleotide exchange factor GEF-H1

Given the slow release of guanine nucleotides from the switch regions of small GTPases, GEFs are essential to accelerate the process of nucleotide exchange. Mechanistically, this is achieved by stimulating the release of GDP, which is subsequently exchanged to GTP that is present at much higher concentrations in cells (Vetter and Wittinghofer, 2001). Many Rho-specific GEFs are members of the large Dbl family, which is characterized by the presence a Pleckstrin homology domain (PH) and the Dbl homology (DH) domain (Zheng, 2001). One specific Dbl-type RhoGEF, called GEF-H1, plays a particularly important role in the processes that are investigated in this thesis. GEF-H1 is well-known for its ability to activate RhoA, and its GEF activity is inhibited by association with microtubules (Krendel et al., 2002). The release of GEF-H1 from microtubules can easily be initiated by treatment of cells with the microtubule depolymerizing compound nocodazole (Chang et al., 2008), or by the ectopic expression of a microtubule-binding deficient C53R mutant (Krendel et al., 2002). Interestingly, the associated increased effective concentration of GEF-H1 in the cytosol does not simply increase baseline Rho activity but instead leads to a dramatic increase in Rho activity dynamics (Graessl et al., 2017). Other RhoGEFs in the related Lbc subfamily, such as LARG or PDZRhoGEF have a similar effect (Graessl et al., 2017; Kamps et al., 2020). As discussed in more detail in the following sections, GEF-H1 and its ability to stimulate Rho activity dynamics plays a central role in a mechanosensitive signal network that controls cell contraction.

### 1.3.2 The topology of the cell contraction signal network

It is well established that cells process not only chemical but also mechanical signals to modulate their function. The transduction of mechanical signals, such as stiffness of the extracellular matrix (ECM), is particularly important during the differentiation of stem cells (Wozniak and Chen, 2009). To sense substrate stiffness, cells must convert such mechanical signals into biochemical signals. This process is known as mechanotransduction (Aguilar-Cuenca et al., 2014). Cells achieve this task via a complex, multilevel signaling system. Important components of this system are adapter proteins, transmembrane receptors and contractile actomyosin structures (see section 1.2.2).

In the context of mechanotransduction, actomyosin-driven, highly dynamic cell contraction pulses were observed in several model organisms (Martin et al., 2009; Bement et al., 2015; Graessl et al., 2017; Saha et al., 2018; Michaux et al., 2018; Nalbant and Dehmelt, 2018; Kim et al., 2018). The frequency of these pulses was found to be modulated by substrate elasticity (Graessl et al., 2017), and they were proposed to be able to transduce mechanical signals more efficiently than constant tension (Cui et al., 2015; Graessl et al., 2017; Nalbant and Dehmelt, 2018). One downstream target of these pulses is cell differentiation, which was not only found to be correlated with Rho GTPase signal network oscillation frequency, but also was artificially steered by external, optogenetic oscillatory stimulation of this signal network (Sampayo et al., 2023).

Previous work already revealed several aspects of the signal network that generates dynamic, actomyosin-driven cell contraction pulses (Graessl et al., 2017). As delineated in section 1.1.1, pulsatile dynamics can be generated by an activator/inhibitor network (Figure 1D). Indeed, detailed experimental investigations strongly support the idea that the observed pulses were the result of such a network topology (Figure 3B). The Rho GEF GEF-H1 (section 1.3.1) activates Rho by catalyzing the exchange from GDP to GTP via the catalytical activity of its DH domain. At the same time, active Rho can recruit more GEF-H1 molecules to the plasma membrane, because the PH domain of GEF-H1 selectively binds to the active form of small GTPase RhoA. This mutual stimulation results in a positive feedback loop between Rho and GEF-H1 via the concurrent recruitment of both proteins to the plasma membrane resulting in the amplification of both activities. Downstream of RhoA, actin and Myosin II are recruited with a delay (Figure 3B) of 11s and 40s, respectively (Graessl et al., 2017). This delayed recruitment of actin and Myosin inhibits the amplification of Rho activity by GEF-H1 (Lee et al., 2010; Graessl et al., 2017), thereby closing a slow negative feedback loop, which can generate oscillatory and excitable system dynamics in combination with the fast positive feedback loop (Novák and Tyson, 2008).

### 1.3.3 Measuring spatio-temporal patterns of Rho activity

As these feedback mechanisms and the resulting Rho activity oscillations occurred in small subcellular regions of the plasma membrane, the implementation of tools to measure the Rho activity state locally with high spatial and temporal resolution was critical. Several strategies were developed to generate sensor constructs that can accomplish this task. One of these

strategies is based on fluorescence resonance energy transfer (FRET) (Pertz et al., 2006). One of the first widely used Rho sensor of this kind utilizes a Rho binding domain (GTPase binding domain, GBD) of the Rho effector rhotekin, which specifically binds to the active form of Rho (Ren et al., 1999). The GBD was flanked by a cyan fluorescent protein (CFP), full-length RhoA and YFP (yellow fluorescent protein) via an unstructured linker. Upon activation of RhoA, the relative orientation of the two fluorophores was altered, resulting in a change in FRET from CFP to YFP. This change of FRET was clearly measurable *in vitro* and indicated changes in the activity state of RhoA in specific locations of individual cells.

A key concern with this FRET biosensor design is that it does not measure endogenous Rho activity, but rather the activity of the transfected Rho-FRET biosensor. As the fusion of several additional protein modules (GBD, 2 fluorescent proteins) significantly altered the properties of RhoA, it was unclear if the sensor signals reliably report biologically relevant information. One interpretation was that these sensors report the ratio of stimulatory GEF and inhibitory GAP activities and therefore would also provide valuable information, where endogenous Rho might get activated. However, a recent review suggested that the subcellular localization of such sensor constructs does not reflect the subcellular localization of the Rho GTPase itself, and that activities are reported in cell regions that are devoid of endogenous RhoA (Seze et al., 2023). Consequently, a simpler biosensor design that is easier to interpret has recently gained increased recognition. Basically, these sensors simply consist of the GBD of rhotekin, linked to a fluorescent protein. This sensor is then simply translocated to cell regions with increased activity of endogenous Rho (Figure 3C) (Benink and Bement, 2005). The sensitivity of these biosensors can be enhanced by tandem repeats of the rhotekin GBD, thus increasing their translocation to sites of active Rho. Given the potential of the artificially expressed GBDs to compete with endogenous Rho effectors, the sensors have to be expressed at very low levels, for example using the weak delCMV promoter (Watanabe and Mitchison, 2002), and because of these low levels, the translocation of the sensor has to be measured with a very sensitive method. Total internal reflection fluorescence microscopy (TIRF-M) is particularly well suited for this task, as this method enables the sensitive detection of fluorescently labeled proteins near the plasma membrane, the subcellular localization in which active Rho plays its major role in regulating cell contraction (Figure 3C). Therefore, optimized constructs and analysis procedures to analyze Rho activity dynamics in adherent mammalian cells typically

contain one of multiple GBDs, expressed at low levels that are recorded via TIRF microscopy (Graessl et al., 2017; Kamps et al., 2020; Nanda et al., 2023; Seze et al., 2025).

Figure 3D shows an example, in which subcellular Rho activity pulses were measured using this TIRF microscopy-based approach. In this example, Rho activity dynamics were stimulated by strengthening the positive feedback loop between active Rho and GEF-H1, simply by ectopic expression of the constitutively active GEF-H1 C53R mutant (see section 1.3.1). As expected from their mutual activation, and as evident from the signal measurements (Figure 3D), the Rho activity sensor and GEF-H1 signals have nearly identical dynamics (see also Graessl et al. (2017)). Therefore, fluorescently labeled GEF-H1 C53R can be utilized both as a stimulator of Rho activity pulses and as sensor to measure spatio-temporal Rho activity dynamics, which is a very valuable feature of this construct that will be extensively used throughout this work.

### 1.3.4 Rapid spatio-temporal perturbation of Rho activity in cells

Figure 3D provides an example how simple measurements of the close spatio-temporal correlation of GEF-H1 plasma membrane translocation dynamics and Rho activity dynamics can provide critical information about how components might be connected to each other in a signal network. However, correlation by itself does not prove the existence of causal links between these molecules (Pearl, 2013). To obtain information about causalities it is instead necessary to introduce perturbations and to measure the associated signal network response. A simple way to actively perturb signal networks is by stimulating or inhibiting network components, for example by constitutive over-expression of proteins or protein mutants, or by gene knockout or mRNA knockdown. However, all these methods introduce perturbations in the entire cell, and they act over long time periods of hours or days and allow cells to adapt. Small pharmacological compounds can act relatively fast, but they still lack spatial selectivity and typically affect the whole cell. To overcome these limitations, the so-called molecular activity painting (MAP) method was developed (Chen et al., 2017; Kamps et al., 2020). This method enables the rapid induction of highly local perturbations at the plasma membrane of living cells. This perturbation can be combined with monitoring of the signal network response to investigate potential causal links between its components.

To perform MAP, cells must express several protein fusion constructs: 1) An artificial receptor that is modified by a photocaged chemical dimerizer, and 2) A protein of interest (POI) that is fused to a dimerization domain that can bind the dimerizer on the receptor after uncaging. The artificial receptor, which is referred to as a “dimerizer-PARC” (dimerizer Presenting Artificial Receptor Construct) includes extracellular viral epitopes that bind to surface-immobilized antibodies (Figure 4). This prevents lateral diffusion of dimerizer-PARCs in the plasma membrane. Intracellularly, the receptor contains a HaloTag domain which binds covalently to the cell-permeable 6-nitroveratroyloxycarbonyl (Nvoc)-caged photo-dimerizer (Nvoc-TMP-Cl). Uncaging the photochemical dimerizer with a single pulse of 405 nm light releases the Nvoc group from Nvoc-TMP-Cl. The remaining trimethoprim (TMP) group can then bind to the *E. coli* dihydrofolate reductase (eDHFR) domain fused to a POI (Figure 4). Consequently, local photo-uncaging leads to a local increase of the bound POI, resulting in the localized and sustained "painting" of the POI and its associated signal activities at the plasma membrane of living cells (Figure 4). Although the uncaging uses relatively short wavelength 405 nm light, phototoxicity is usually not problematic, as only a single, short laser pulse is sufficient for the perturbation. The irreversible character of the perturbation also makes this method easier to implement compared to reversible light-controlled perturbations that require sustained patterns illumination. Furthermore, as the uncaging wavelength does not overlap significantly with excitation wavelengths of further red-shifted fluorescent proteins, such as CFP, GFP, YFP, and mCherry derivatives, MAP-based perturbations can easily be combined with multiple fluorescent readouts (Chen et al., 2017; Kamps et al., 2020; Kowalczyk et al., 2022).

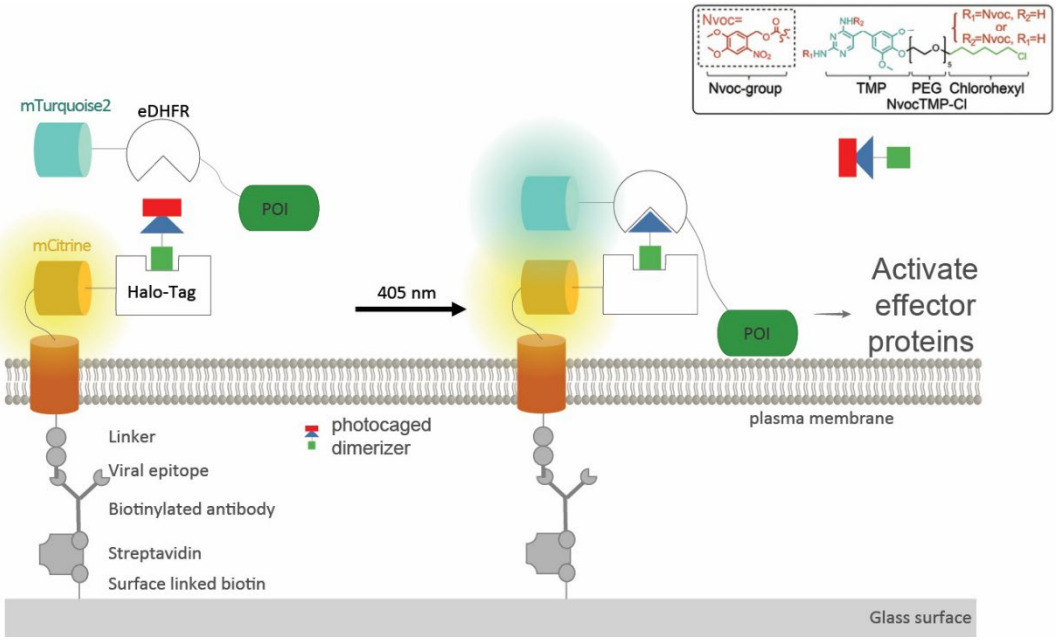


*Figure 4: Schematic of Molecular Activity Painting (MAP) to introduce rapid perturbations at the plasma membrane of living cells. A protein-of-interest (POI) is fused to* E. coli *dihydrofolate reductase (eDHFR) and recruited to dimerizer Presenting Artificial Receptor Constructs (dimerizer-PARCs) after photouncaging of a 6-nitroveratroyloxycarbonyl (Nvoc)-caged photo-dimerizer (Nvoc-TMP-Cl). dimerizer-PARCs bind covalently to the photo-dimerizer via a Halo-Tag and their diffusion is prevented by binding to antibodies that are immobilized at the glass surface. Recruitment of the POI increases its local concentration and can thereby activate potential effector proteins.*

### 1.3.5 Quantitative modeling of cell contraction signal network dynamics

As discussed in the introduction, the dynamics of signaling networks can be described quantitatively by systems of ordinary differential equations (ODEs). In previous work, a system of ODEs was developed to quantitatively investigate the pulsatile dynamics of the cell contraction signaling network (Kamps et al., 2020). In brief, the system is based on three components, GEF-H1, Rho, and Myosin, which are represented by the variables G, R, and M, respectively. The reactions that change the activity of these components as a function of time are shown schematically in Figure 5A, and the corresponding system of differential equations is given in the methods (section 7.8) and in Figure 5B.

The values for the system parameters (total concentrations $G_T$, $R_T$, $M_T$ of GEF-H1, Rho, and Myosin, respectively, as well as rate constants $k_1$-$k_6$ and Michaelis constants $K_{m1}$, $K_{m2}$, $K_{m5}$, and $K_{m6}$) were either estimated based on the literature or estimated via a Bayesian fitting approach using experimental data (Kamps et al., 2020). Simulations based on this system of ODEs generated dynamics in the Rho and Myosin components that very closely resembled the

corresponding experimental observations (Figure 5C). Therefore, this system can be used as a basis to predict, how the signal network is expected to change if a specific feature of this signal network is manipulated.

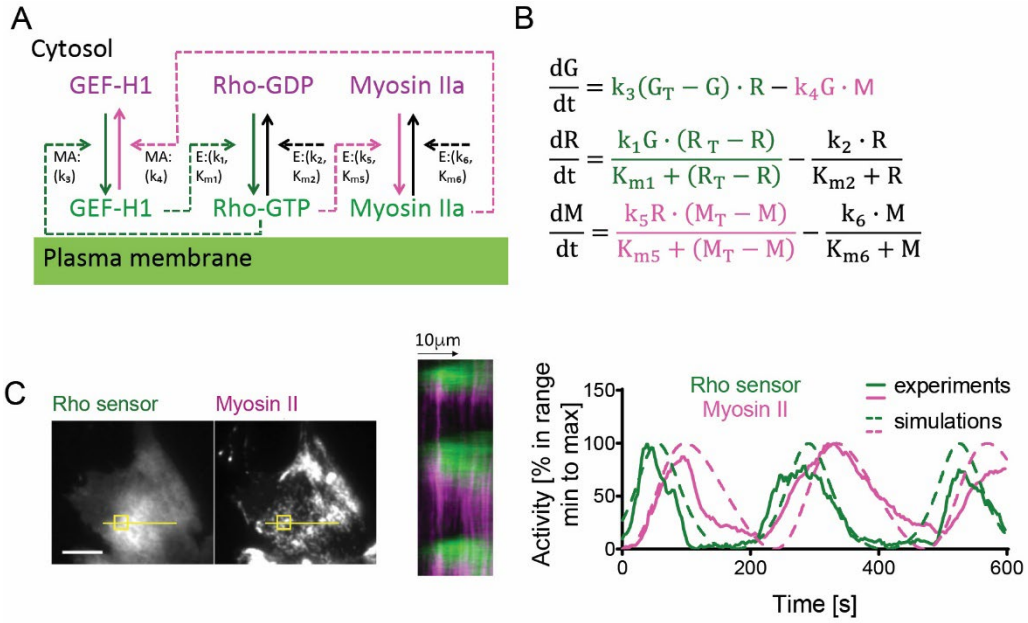


*Figure 5: Theoretical basis of the cell contraction signal network dynamics. (A) A Biochemical reaction scheme of positive as well as negative feedback regulation of Rho activity in the cell contraction signaling network. Solid arrows represent translocations between the cytosol and plasma membrane, which are associated with changes in the activity state of the GEF-H1, Rho and Myosin IIa components. Dotted arrows represent causal links between these components. The green dotted arrows close a positive feedback loop and the magenta dotted lines close a negative feedback loop. MA: mass action, E: enzymatic reaction. (B) System of ordinary differential equations which correspond to the reaction scheme in A, and which are the basis for numerical simulations used in Kamps et al. (2020). (C) A U2OS cell transfected with Rho activity sensor (green) and non-muscle Myosin IIa heavy chain (magenta) that exhibits pulsatile cell contraction dynamics (left). The kymograph (middle) corresponds to the yellow line in the cell images. Solid lines in the plot (right) show the quantification of the fluorescence intensity changes in the yellow box region in the cell images and dotted lines were obtained by numerical simulations of the ODE system shown in C. The cell was treated with nocodazole to increase non-microtubule bound GEF-H1 levels. Adapted from Kamps et al. (2020).*

### 1.3.6 Potential mechanisms of negative feedback in cell contraction signaling

As previously outlined (section 1.3.2), the delayed negative feedback in the activator/inhibitor network topology underlying the cell contraction signaling network was proposed to be an actomyosin-dependent process, and there are several lines of evidence that support Myosin as negative feedback mediator: The recruitment of Myosin is nearly anti-phasic to Rho activity

at the plasma membrane, thus suggesting that the rise of Myosin is associated with a corresponding decrease in Rho activity (Graessl et al., 2017; Kamps et al., 2020; Kowalczyk et al., 2022). Additionally, the system shows a significant decrease in pulsing activity after the direct or indirect inhibition of Myosin activity. For example, as demonstrated by Graessl et al. (2017), the inhibition of the Rho kinase ROCK via the small molecule inhibitor Y27632 acutely reduces the frequency of Rho activity pulses. As this kinase is a well-known activator of Myosin downstream of active Rho, this observation offers indirect support for the hypothesis of a role for Myosin in the regulation of cell contraction dynamics. Furthermore, more direct inhibition of Myosin II activity via the small molecule inhibitor blebbistatin had a comparable effect (Graessl et al., 2017). One potential mechanism of the Myosin mediated feedback might be the proposed binding of active Myosin to the DH domain of GEF-H1 (Lee et al., 2010; Kamps et al., 2020). This interaction could potentially inhibit GEF-H1 mediated Rho activation by competing with the nucleotide exchange activity of the GEF-H1 DH domain, thus disrupting the positive feedback (Lee et al., 2010; Kamps et al., 2020).

Interestingly, while these studies on adherent mammalian cells indicated a role for contractile actomyosin structures and specific non-muscle Myosin II in negative feedback, several lines of research in other systems, that include Starfish and *Xenopus* oocytes and *C. elegans* embryos, revealed a specific involvement of F-actin. Furthermore, these studies also found that non-muscle Myosin II was not essential for generating pulsatile signal network dynamics (Nishikawa et al., 2017; Michaux et al., 2018). It was revealed that, in Starfish and *Xenopus* oocytes, the RhoGAP RGA3/4 is recruited to the cell cortex by F-actin. There, it inhibits Rho activity, closing a negative feedback loop what controls cell contraction pulses (Michaud et al., 2022). The negative feedback regulation in *C. elegans* embryo cell contraction pulses is driven by a similar mechanism (Michaux et al., 2018).

Such an actin-based Rho inhibition mechanism can also be effectively enforced in U2OS cells by ectopic expression of the Rho inhibiting GTPase-activating protein (GAP) Myo9b (Müller et al., 1997; Graessl et al., 2017). This protein is recruited to sites of increased Rho activity (Graessl et al., 2017; Michaud et al., 2022) by binding to F-actin, which in turn can be stimulated by Rho, for example via the actin nucleator FHOD1 (Kühn and Geyer, 2014). However, the generated pulses had a much higher frequency than the observed frequency with endogenous Myo9b levels, and the amplitude was much lower (Graessl et al., 2017).

Both, FHOD1 and Myosin II are not direct effectors of Rho, but instead activated downstream of the Rho effector ROCK (Gasteier et al., 2003; Graessl et al., 2017; Garrido-Casado et al., 2021).

Taken together, these studies are controversial and thus suggest that the mechanism that mediates negative feedback regulation of cell contraction dynamics might be species or context specific and potentially more complex than currently appreciated.

## 1.4 The role of the Rho effector kinase ROCK in cell contraction regulation

As described above, Rho-associated coiled-coil containing protein kinases (ROCKs) were shown to play a central role in the regulation of cell contraction. ROCKs are serine-/threonine kinases and important effectors of Rho (Watanabe et al., 1996). They are well-known for their ability to activate Myosin II via activating phosphorylation of the Myosin regulatory light chain, as well as via inactivating phosphorylation of the Myosin regulatory light chain phosphatase MYPT1 (see section 1.2.2) (Amano et al., 1996; Kimura et al., 1996; Matsui et al., 1996).

Two human ROCK isoforms were identified, ROCK1 with 1354 amino acids and ROCK2 with 1388 amino acids. Both isoforms comprise three major protein domains. First, the N-terminal kinase domain followed by a long coiled-coil domain that contains three Rho binding domains (HRI, RID, and RBD) (Blumenstein and Ahmadian, 2004). The coiled-coil is also responsible for the dimerization of ROCKs (Nakagawa et al., 1996). At their C-terminus, these proteins exhibit a split PH domain (Pleckstrin homology) (Nakagawa et al., 1996) that has an inserted C1 domain (cysteine-rich zinc finger-like motif) (Figure 6A). The entire domain is called the PHC1 tandem domain (Wen et al., 2008).

In analogy to the typical roles of PH and C1 domains, the PHC1 tandem domain of ROCK was originally thought to play a role in plasma membrane binding. Many PH and C1 domains can specifically recognize signal lipids such as PIP2 or PIP3, or DAG, respectively. However, the PH and C1 domain parts of the ROCK PHC1 domain lack the critical amino acids that are responsible for these specific interactions. In contrast, the PHC1 domain contains a relatively large number of positive charges that can interact with the negatively charged headgroups of

biological lipids, and indeed, these positive charges were found to play a crucial role in ROCK membrane binding (Figure 6B) (Wen et al., 2008).

Despite this knowledge about the function of these domains, the mechanisms by which ROCKs are regulated are still unclear.

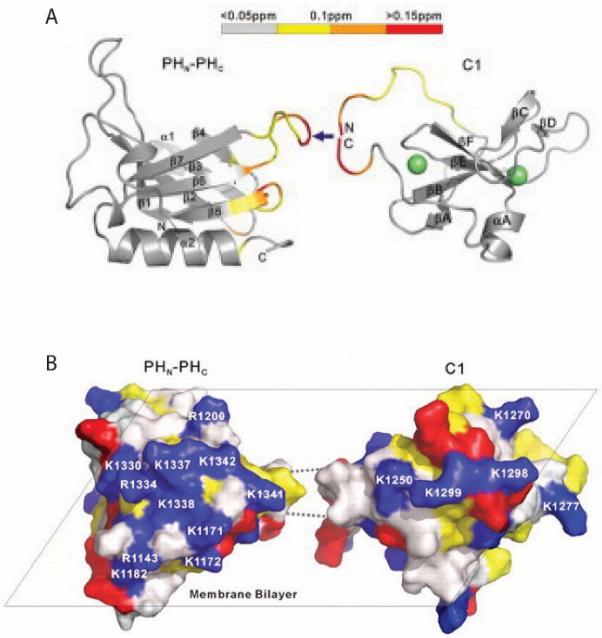


*Figure 6: Structure of the PHC1 tandem domain of ROCK. (A) Mapping of the PH and C1 domain in a 3D structure. The black arrow indicated the insertion site of C1 into the split PH domain. (B) Model to demonstrate the possible synergic action of positively charged amino acids (blue) on both domains in the tandem supramodule to bind the plasma membrane. Adapted from Wen et al. (2008).*

### 1.4.1 Classical mechanism for ROCK regulation via autoinhibition

In earlier studies, a relatively simple mechanism for ROCK activation was suggested, in which the N-terminal kinase domain is bound and inhibited by the C-terminal region of ROCK (Chen et al., 2002), and in which the interaction between active Rho and the ROCK C-terminus releases this autoinhibition (Figure 7A) (Raouf A. Khalil, 2010; Khalil, 2010). This idea is supported by the observation that C-terminal truncation mutants of ROCK are constitutively active (CA), while N-terminally truncated mutants exhibit dominant negative effects (Amano et al., 1997; Ishizaki et al., 1997; Amano et al., 2000; Asp et al., 2002).

### 1.4.2 "Molecular Ruler Hypothesis" for ROCK function

However, more recent studies raised questions about this idea, suggesting that ROCK is always in a fully extended conformation. In this conformation, its long coiled-coil region acts as a

spacer, positioning the kinase domain approximately 120 nm away from the plasma membrane (Figure 7B) (Truebestein et al., 2015). Based on this hypothesis, the N-terminal kinase domain of ROCK can only reach and then activate Myosin in the dense cell cortex near the plasma membrane in the extended conformation. Indeed, removing even a small section of the coiled-coil was found to interfere with ROCKs ability to activate Myosin. However, this mechanism also raised questions about the mechanism, how Rho could activate ROCK, as all known Rho GBDs (GTPase binding domain) are located within the coiled-coil domain, which is well-separated from the plasma membrane in the extended ROCK conformation (Figure 7B). Furthermore, these studies did not confirm the previously characterized interaction between ROCK and active Rho and even questioned that a specific interaction between active Rho and ROCK might exist. Consequently, there is a gap in our knowledge regarding the activation of ROCK and its downstream activities.

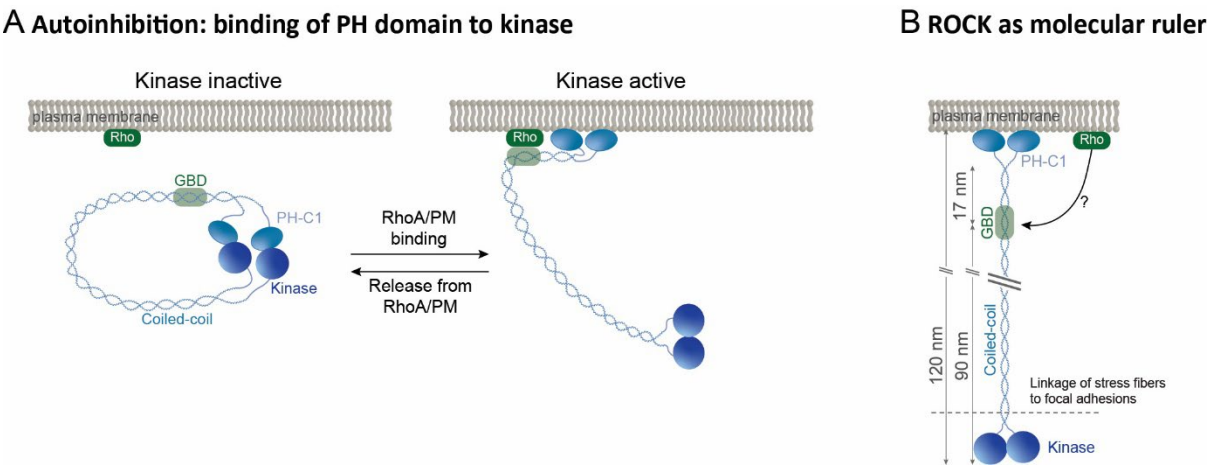


*Figure 7: Models of ROCK regulation. (A) The classical model of ROCK regulation via autoinhibition posits that the PHC1 domain inhibits the kinase domain. (B) A more recent model suggests that the coiled-coil domain places the kinase domain at a specific distance from the plasma membrane. In the model, ROCK1 is believed to be constantly bound to the plasma membrane. However, it is unclear how RhoA can activate ROCK in this conformation. Figure adapted from Gierse et al. (2025b).*

## 1.5 Objective

The aim of this thesis was to gain a deeper understanding of negative feedback regulation in the cell contraction signal network of mammalian, adherent cells. Previous investigations by Graessl et al. (2017) and Kamps et al. (2020) already clearly established that pulse or wave-like cell contraction signal network dynamics are generated by a combination of positive and negative feedback regulation, and that positive feedback is mediated by mutual activation

between active Rho and GEF-H1. The studies by Graessl et al. also already provided evidence for delayed negative feedback regulation which is dependent on intact and dynamic actomyosin structures. During the same time, studies in other model systems, including *Xenopus* oozytes or *C. elegans* embryos, suggested that Myosin itself is not required for cell contraction signal network dynamics, but that instead actin is the critical negative feedback component. To resolve this question, the initial objective of this study was to introduce long-term or rapid light-controlled perturbations in mammalian, adherent cells, to directly investigate the role of Myosin in negative feedback regulation (Results section 2.1). In particular, perturbation constructs that are based on the Myosin-activating kinase ROCK1 were chosen to introduce perturbations into the signal network. However, the initial attempts to control ROCK activity with light were not successful and revealed a more complex mechanism for its regulation than initially anticipated. This lead to new objectives to investigate ROCK1 regulation by Rho activity (Results section 2.2) and to investigate the crosstalk between RhoA and the unconventional Rho GTPase Rnd3 (Results section 2.3).

# 2 Results

## 2.1 Negative Feedback regulation of the cell contraction network

As discussed in section 1.1.1, it is often difficult to predict how the dynamics of signal networks with feedback regulation are affected by experimental manipulations. Based on previous results, the cell contraction signal network, which combined both positive and negative feedback, is a prime example for such a system. In particular, it is challenging to predict how its pulsatory dynamics, as shown in Figure 5C, are modulated by specific manipulations of system components. To gain a more quantitative understanding of this system, simulations were performed based on stochastic differential equations (SDEs) that were established previously by Kamps et al. (2020).

Figure 5B in the introduction already introduced a system of ordinary differential equations (ODEs) that can closely reproduce the oscillatory system dynamics of the cell contraction signal network (Figure 5C). To enable more realistic simulations, stochastic effects were introduced by Kamps et al. into the slowest, rate-limiting Myosin component (Kamps et al., 2020). The resulting system of stochastic differential equations (SDEs) is as follows:

$$dG = (\mathrm{k_3}(\mathrm{G_T} - \mathrm{G}) \cdot \mathrm{R} - \mathrm{k_4}\mathrm{G} \cdot \mathrm{M})\mathrm{dt} \qquad \text{equation (1)}$$

$$dR = \left(\frac{\mathrm{k_1}\mathrm{G}\cdot(\mathrm{R_T}-\mathrm{R})}{\mathrm{K_{m1}}+(\mathrm{R_T}-\mathrm{R})} - \frac{\mathrm{k_2}\cdot\mathrm{R}}{\mathrm{K_{m2}}+\mathrm{R}}\right) dt \qquad \text{equation (2)}$$

$$dM = \left(\frac{\mathrm{k_5}\mathrm{R}\cdot(\mathrm{M_T}-\mathrm{M})}{\mathrm{K_{m5}}+(\mathrm{M_T}-\mathrm{M})} - \frac{\mathrm{k_6}\cdot\mathrm{M}}{\mathrm{K_{m6}}+\mathrm{M}}\right) dt + \sigma \cdot dW \qquad \text{equation (3)}$$

The ODE system shown in Figure 5B was modified with small, stochastic processes that influence the system (equation (3)). This was modeled by a low level of Gaussian noise $\sigma \cdot dW$, with $dW = r \cdot \sqrt{dt}$, with σ being a factor that represents the level of Gaussian noise, and r corresponding to normally distributed random numbers with a standard deviation of 1 (Kamps et al., 2020). Incorporating such stochastic changes are justified, as it is well-known that the 3 simulated network components are influenced by many additional factors, many of which are highly stochastic in their nature.

Theoretical investigations based on this SDE system were combined with experimental manipulations of the cell contraction signal network in the U2OS osteosarcoma cell line. Similar to previous studies (Figure 5) (Graessl et al., 2017; Kamps et al., 2020) total internal reflection fluorescence (TIRF) microscopy was employed to measure subcellular, spatio-temporal dynamics of the plasma membrane translocation of signal network components to evaluate their activity state. In particular, cell contraction signal network dynamics were stimulated by releasing the positive feedback mediator GEF-H1 from microtubules by treating cells with the microtubule-destabilizing drug nocodazole and by measuring Rho activity via a GTPase-binding domain (See sections 1.3.1 and 1.3.3 and Figure 3B-C). Alternatively, we expressed the microtubule-binding deficient GEF-H1 C53R mutant, which can also stimulate cell contraction signal network dynamics and in parallel can be used to measure local Rho activity dynamics (see sections 1.3.1 and 1.3.3 and Figure 3D). To evaluate, how experimental manipulations affect signal network dynamics, a custom-build automated analysis ImageJ macro (Graessl et al., 2017) was used to measure the local standard deviation of the signal, as well as the frequency and amplitude of signal network activity pulses (see also Methods section 7.10.2).

### 2.1.1 Both inhibition and constitutive activation of Myosin inhibit cell contraction signal network dynamics

In the initial theoretical investigations, the SDE system by Kamps et al. (Figure 5) was employed to gain more detailed insights into the mechanism of negative feedback regulation (Figure 8A). This system is based on the hypothesis that Myosin functions as the sole negative feedback regulator and simulations that include specific manipulations were compared with corresponding experiments to challenge this hypothesis.

First, manipulations were implemented in the theoretical network model for which the corresponding experimental response was already known. Specifically, the effect of two distinct inhibitors on signal network dynamics were investigated: The direct inhibition of the Myosin component by blebbistatin, which is expected to reduce the total amount of activation competent Myosin (variable $M_T$; see Methods for details) (Figure 8B-C), and the inhibition of ROCK using the specific inhibitor Y27632. This is represented by the reduction of the rate constant $k_5$, which links the Rho and Myosin activities (Figure 8D-E).

Simulations of the system dynamics showed that the direct inhibition of Myosin has little to no effect on pulsatory signal network dynamics until an inhibition level of 90%. From 90% to 92%, both the peak height and peak frequency decrease sharply, and no pulsatile dynamics at inhibition levels that exceeded 93% could be measured (Figure 8C-D). These results agree with experimental findings reported by Graessl et al. (2017), which showed that a high concentration of the Myosin inhibitor blebbistatin (30 µM) was necessary to significantly inhibit or reduce pulsatory signal network dynamics in cells. At lower concentrations both Rho and Myosin were still highly dynamic, suggesting that a small fraction of Myosin was sufficient to support pulse generation.

Simulations of the effect of ROCK inhibition indicate a more gradual concentration dependency compared to direct Myosin inhibition (compare Figure 8C to E). In particular, a gradual reduction in dynamics as evidenced by a decrease in peak frequency and peak height with increasing levels of ROCK inhibition was observed (Figure 8E). This is in agreement with experimental observations reported in Graessl et al. (2017) on peak frequency, and with results on peak amplitude reported in the PhD thesis related to this publication (PhD Thesis Melanie Graessl, 2015). In these experiments, a reduction in peak height and frequency is

observed over a broader concentration range of the Y27632 inhibitor, and not a switch-like concentration dependence as with blebbistatin. These SDE simulations therefore align with the previously published experimental results of cell contraction network perturbations, and thereby validate the applicability of the SDE system, and further support the idea that negative feedback is mediated via Myosin II.

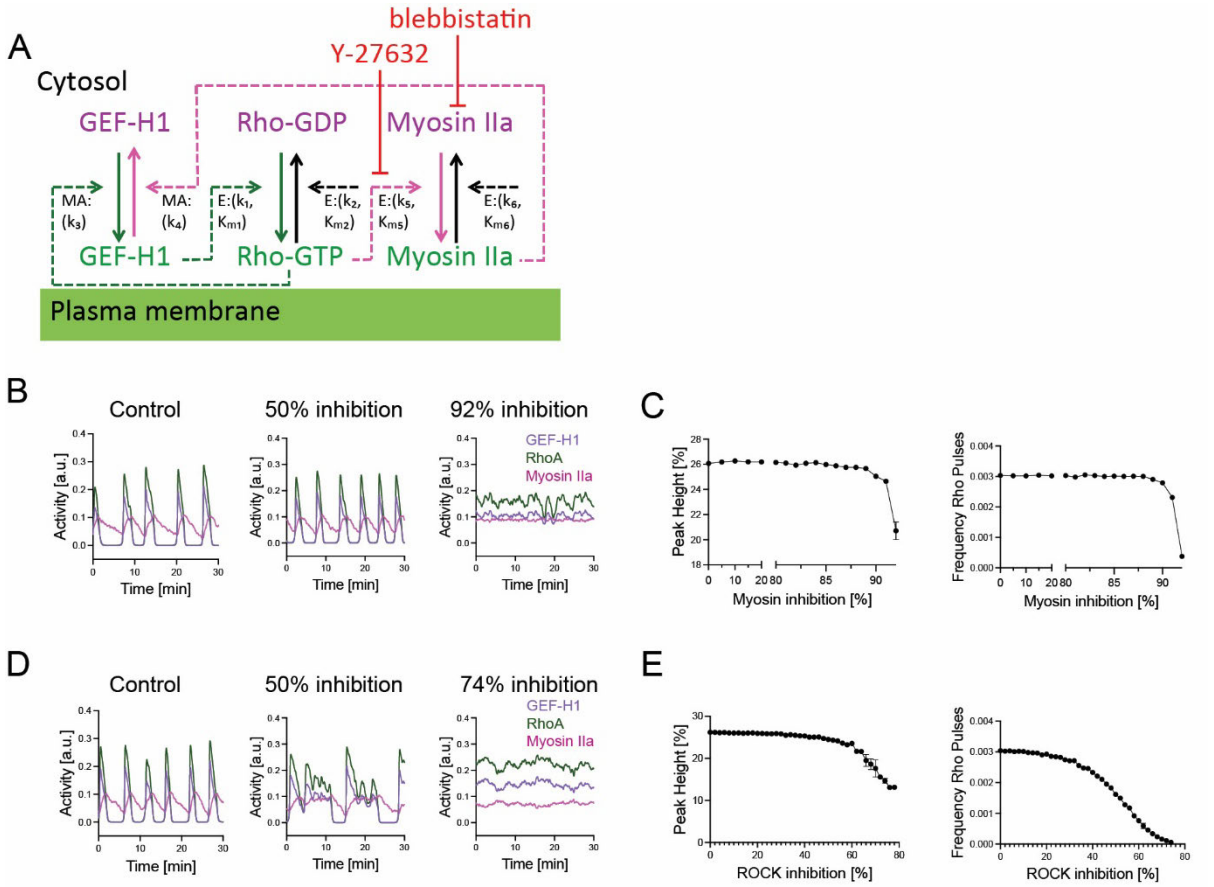


*Figure 8: Theoretical investigation of the role of Myosin and ROCK inhibition in cell contraction signal network dynamics. (A) Simplified biochemical reaction scheme that is proposed to generate excitable and oscillatory dynamics of cell contraction (see Methods for details). Red inhibitory arrows indicate perturbations via inhibitors. (B) Representative simulations of signal kinetics at indicated levels of Myosin inhibition obtained via SDE simulations. No pulsatile dynamics were observed at high levels of Myosin inhibition, even if prolonged simulations were performed that corresponded to more than 24h of simulated time. (C) Rho activity peak height (left) and Rho pulse frequency (right) dependence on decreasing Myosin levels (n=3 independent simulations for each value). On the x-axis, Myosin inhibition corresponds to the percentage reduction of the $M_T$ parameter (total Myosin concentration, i.e., the sum of active and inactive Myosin). (D) Representative simulations of signal kinetics at indicated levels of ROCK inhibition obtained via SDE simulations. (E) Rho activity peak height (left) and Rho pulse frequency (right) dependence on increasing levels of ROCK inhibition (n=3 independent simulations for each value). On the x-axis, ROCK inhibition corresponds to the percentage reduction of the $k_5$ parameter shown in A, which represents the Myosin activation rate downstream of active Rho. Figure adapted from Gierse et al. (2025a).*

Even though the negative effect on system dynamics after Myosin inhibition supports the SDE-based model, the inhibition of such a central cellular component could also have an indirect effect that could explain these results. Therefore, complementary investigations were performed that are based on constitutive activation of Myosin II, both within the simulations and experimentally. This can for example be achieved by expression of a constitutively active ROCK1 mutant (CA-ROCK1). Conceptually, this mutant would be an additional component that needs to be added to the cell contraction signal network simulation (Figure 9A). Due to its constitutive activity, there are no inputs into this component, but only an output into the Myosin component. To keep this component as simple as possible, it is implemented by a single enzymatic reaction with effective rate constant $k_7$ and Michaelis constant $K_{m7}$. Our simulations predicted that even a very small amount of constitutive Myosin activation can strongly inhibit network dynamics (Figure 9B, right). While concentration dependency is clear (Figure 9C), the simulations indicate that this dependence is only observed within a very narrow range of very low CA-ROCK1 activity levels (Figure 9C).

This inhibition of system dynamics was confirmed via experiments in U2OS cells. As shown in Figure 9D (right), expression of a previously established constitutively active ROCK1 mutant (CA-ROCK1) effectively suppressed the signal network dynamics observed via a Rhotekin-based Rho activity sensor. Our observations revealed a decrease in both peak height and frequency (Figure 9D, right), and these measurements thus confirm the predictions that were obtained via simulations (Figure 9D, left). [1]

The CA-ROCK1 construct is a C-terminal truncation of full-length ROCK1 that contains only the kinase domain and a part of the coiled-coil for dimerization, which is essential for kinase activity (data not shown). This construct has been utilized in numerous studies, which have demonstrated an increase in cell contraction activity, as evidenced for example by increased stress fiber formation (Ishizaki et al., 1996; Leung et al., 1996; Amano et al., 1997). To confirm that our CA-ROCK1 construct is indeed constitutively active, we stained U2OS cells for filamentous actin (F-actin) with phalloidin (Figure 9E). As illustrated in Figure 9E, the actin structures undergo significant alterations in the presence of CA-ROCK1. In particular, we observed actin accumulations within the cell, which were similar to previous studies that

[1] These investigations were performed under my supervision by Bachelor student Jennifer Hanemann (Thesis year 2023)

documented comparable results (Ishizaki et al., 1996). Here, Cell Profiler was employed to quantitatively assess the levels of F-actin in cells that had been transfected with either the parental control construct or CA-ROCK1. The analysis confirmed the activity of CA-ROCK1: The maximal phalloidin intensity (Figure 9F), which is a measure for local accumulation of F-actin, was significantly increased in cells transfected with CA-ROCK1 compared to the control.

Taken together, these results show that either the inhibition or the constitutive activation of Myosin II inhibits the dynamics of the cell contraction signal network, and that the combination of experimental investigations and simulations supports a direct role for Myosin II in mediating negative feedback regulation in this system.

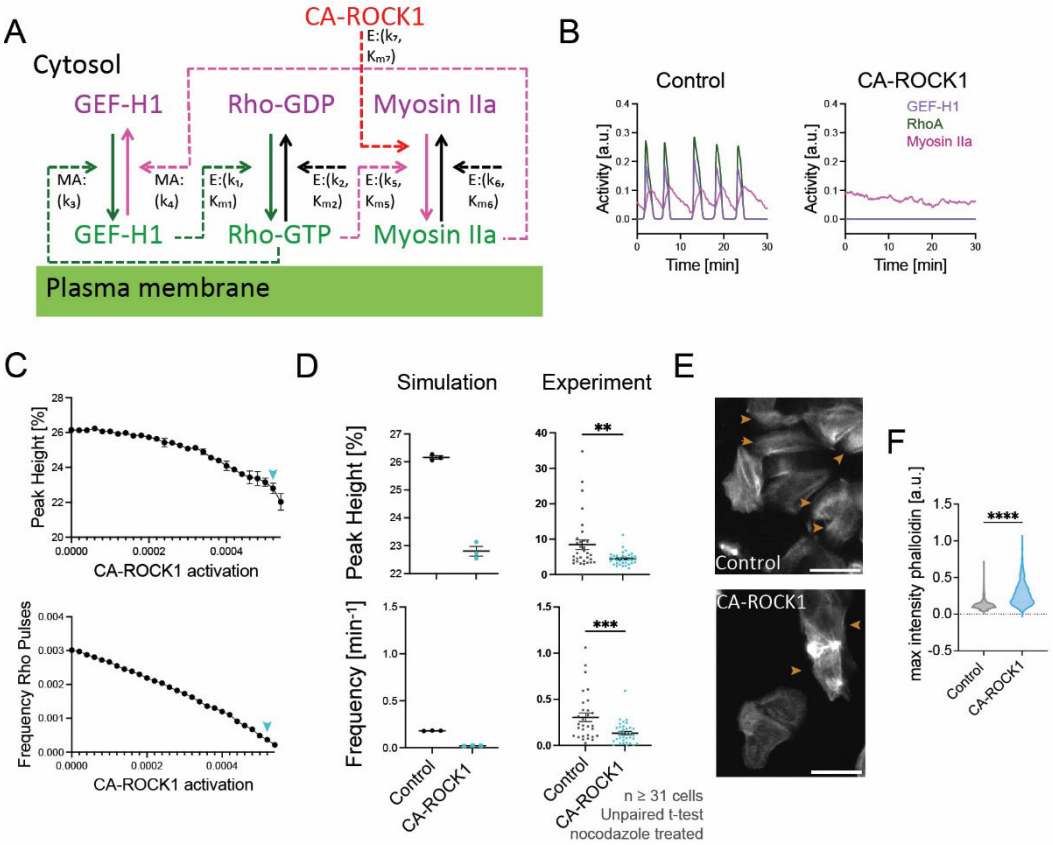


*Figure 9: Continuous activation of Myosin II by constitutively active ROCK1 (CA-ROCK1) inhibits cell contraction signal network dynamics in mammalian adherent cells. (A) Simplified biochemical reaction scheme that is proposed to generate excitable and oscillatory dynamics of cell contraction (see Methods for details). The red arrow from CA-ROCK1 indicates the non-feedback regulated, continuous activation of Myosin II. (B) Representative simulations of signal kinetics in the presence or absence of constitutively active ROCK1 (the CA-ROCK1 activation level corresponds to k7 = 0.0006; see panels C and D). (C) Dependence of Rho activity peak height (top) and Rho pulse frequency (bottom) on increasing Myosin over-activation by increasing CA-ROCK1 levels (n=3 independent simulations for each value). On the x-axis, CA-ROCK1 activation corresponds to the rate constant $k_7$ in the scheme shown in panel A, which represents the Myosin activation. (D) Comparison of Rho activity peak height (top) or pulse frequency (bottom) in the absence or presence of CA-ROCK1, using either SDE simulations (left) or*

*experimental analysis (right). The experimental analysis was obtained from measurements in U2OS cells using a Rhotekin-based translocation Rho activity sensor. The cells co-expressed either an the mCherry fluorophore alone for the control group or mCherry-CA-ROCK1 protein. The signal network dynamics were stimulated by adding 30 µM of nocodazole. SDE simulations were carried out at a CA-ROCK1 concentration corresponding to the blue arrowheads in C. (E) Representative wide-field images of cells expressing either mCherry control (top) or mCherry-CA-ROCK1 (bottom), which were stained for F-actin (Atto488-phalloidin). Cells expressing the respective construct are indicated by the orange arrowheads. (F) Quantification of the maximum phalloidin signal corresponding to the conditions shown in panel E (n = 3 independent repeats with ≥694 cells, unpaired t-test). **: $p < 0.01$, ***: $p < 0.001$, ****: $p < 0.0001$. Scale bar: 50 µm, 0.8 µm/pixel. Figure adapted from Gierse et al. (2025a).*

### 2.1.2 Centripetal flow of active Myosin rescues peripheral cell contraction network dynamics

Careful examination of the effect of CA-ROCK on cell contraction dynamics shown in Figure 9D revealed additional, unexpected changes. While signal network dynamics were strongly suppressed in the majority of cells, some residual activity was still detectable in a subset of cells. Interestingly, network dynamics were only visible in the periphery of these cells, and dynamics were largely absent in central cell attachment areas.

To further investigate this unexpected observation, the effects of long-term CA-ROCK1 expression on Myosin and signal network dynamics were examined by an observer, who was blind to the experimental manipulations. First, the CA-ROCK1 (Figure 10A-C, bottom) or the empty parental plasmid (Figure 10A-C, top) were expressed together with fluorescently labeled Myosin IIa heavy chain. In the control condition, approximately 90% of cells exhibited normal Myosin II structures (stress fibers, small patches), as depicted in the TIRF image of a representative cell (Figure 10A, top). In contrast, in CA-ROCK1 expressing cells, only ∼20% of cells showed a normal organization of Myosin (Figure 10C). Instead, ∼70% of cells expressing CA-ROCK1 had aggregated Myosin II (Figure 10A-C, bottom). In some cells, it was possible to observe a continuous flow of Myosin II towards the aggregation site. The kymograph of the TIRF image of the example cell illustrates this flow (Figure 10B, bottom).

Next, the response of the network dynamics to CA-ROCK1 expression was examined. For these experiments, signal network dynamics were stimulated with GEF-H1 C53R. The cells co-expressed either the empty parental construct as control (Figure 10D-F, top) or CA-ROCK1 (Figure 10D-F, middle and bottom). Control cells exhibited much higher dynamics in central cell attachment areas compared to CA-ROCK1 transfected cells (Figure 10F). Furthermore, in

about 30% of the cells the analysis clearly showed that CA-ROCK1 can induce a shift of signal network dynamics towards peripheral cell attachment regions (Figure 10D-E, middle, and Figure 10F).

What could be the reason for this effect? It is well-established that CA-ROCK1 continuously activates Myosin without feedback control, thus leading to an uncontrolled over-activation of Myosin. Hypothetically, based on the contractile forces generated by Myosin, this uncontrolled activation could result in a continuous centripetal contractile actomyosin flow from the periphery of the cell attachment area towards more central areas. Increased Myosin in the cell center (Figure 10A, bottom) could then locally inhibit Rho amplification, while peripheral areas are less affected due to the depletion of actomyosin via its centripetal flow (Figure 10G). This hypothesis was subsequently confirmed through additional experiments. As shown in the example in Figure 10H-I, Myosin II accumulates near the nucleus due to constitutive Myosin activation. This prevents Rho/GEF-H1 activity dynamics in central cell attachment areas and only allows pulsatory signal network dynamics in the cell periphery, where Myosin is depleted due to contractile flow.

Both observations, the complete inhibition and the spatial shift of pulsatory dynamics, support an inhibitory role of Myosin II on cell contraction signal network dynamics. Therefore, the results obtained from these experiments provide substantial support for the hypothesis that non-muscle Myosin II functions as a negative feedback mediator. In particular, the spatial shift induced by central Myosin accumulation furthermore also suggests that this effect is local in cells, and either mediated directly by Myosin molecules, or by an additional component that is specifically associated with Myosin and only acts very closely within a short distance of actomyosin structures.

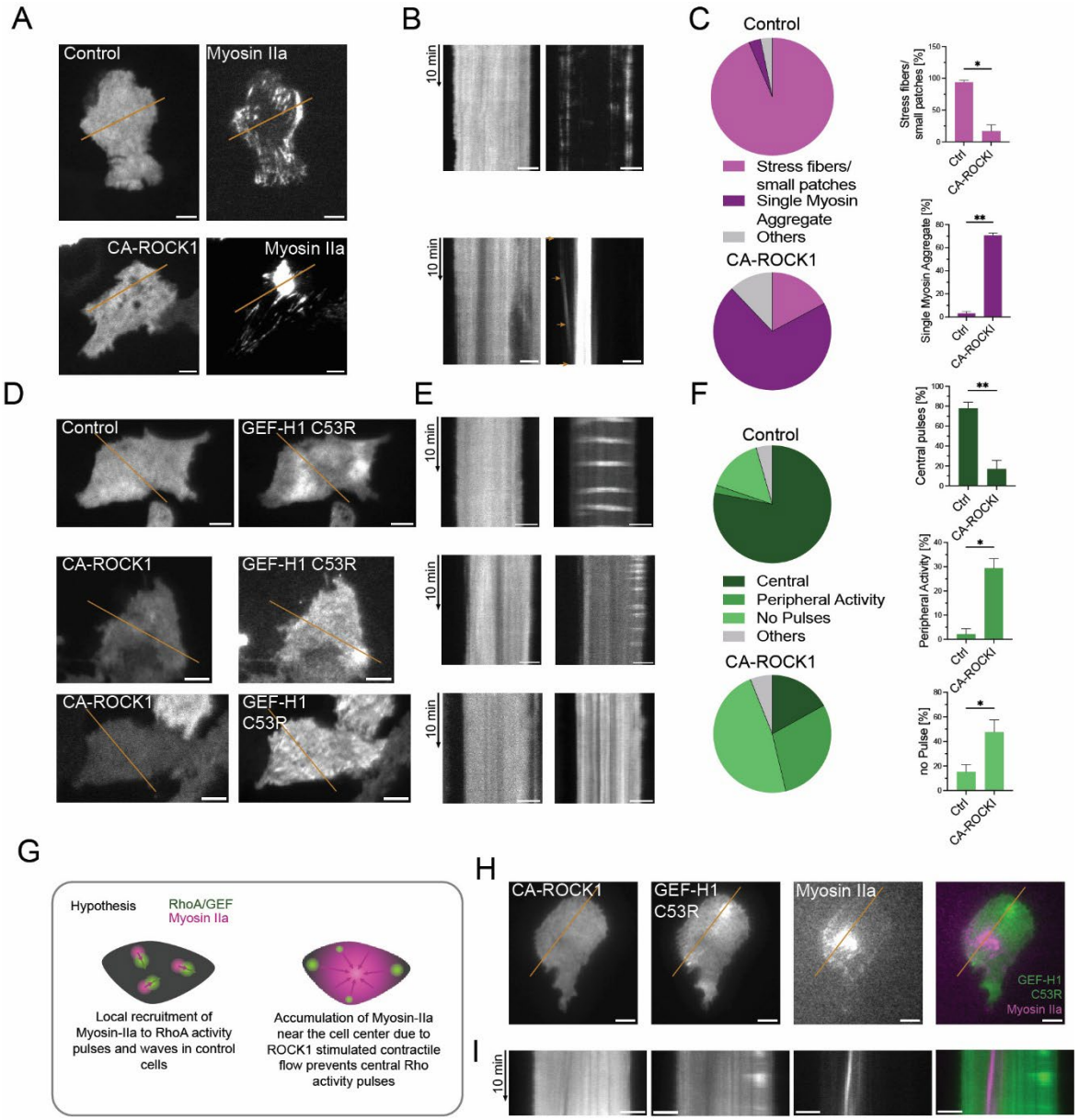


*Figure 10: Continuously activated Myosin IIa by constitutively active ROCK1 (CA-ROCK1) restricts the activity of the cell contraction signal network the periphery of the cell attachment areas. (A-C) Analysis of the Myosin IIa response to CA-ROCK1 expression (long-term). (A) Representative TIRF images of cells expressing mCherry as a control (top) or mCherry-CA-ROCK1 (bottom), together with mCitrine-non-muscle Myosin heavy chain IIa. (B) Kymographs corresponding to regions in A (orange lines). The orange arrows in the bottom right indicate the retrograde flow of Myosin IIa toward the single Myosin IIa aggregate within the example cell. (C) Quantitative analysis of the change of Myosin IIa structures in cells in response to CA-ROCK1 over-expression. (D–F) Analysis of the cell contraction signal network dynamics in response to long-term CA-ROCK1 expression. (D) Representative TIRF images of cells co-expressing mCherry as a control (top), mCherry-CA-ROCK1 (middle and bottom) together with mCitrine-GEF-H1 C53R. (E) Kymographs corresponding to regions in D (orange lines). (F) Quantitative analysis of the effect of CA-ROCK1 on GEF-H1 C53R dynamics. (G) Proposed mechanism of the spatiotemporal shift in GEF-H1 C53R dynamics in cells expressing CA-ROCK1. Continuous Myosin activation leads to the assembly of a single Myosin aggregate within the cell and a contractile flow that reduces active Myosin levels at the cell's periphery. Based on our hypothesis, this would minimize the inhibitory effect of Myosin on Rho activity and restrict the dynamics of the pulsatile signaling network in*

*the peripheral regions of the cell. (H–I) Direct investigation of the effect of Myosin II on signal network dynamics. (H) Representative TIRF images of cells co-expressing mCherry-CA-ROCK1, mCitrine-GEF-H1 C53R, and mTurquoise-non-muscle Myosin heavy chain IIa. (I) Kymographs for the regions indicated in H (orange lines). n = 3 independent experiments with >42 cells for A–C and >32 cells for D–F. Error bars represent standard error of the mean, *: p < 0.05, **: p < 0.01, unpaired t-test. Scale bars: 10 µm; 0.26 µm/pixel. Figure adapted from Gierse et al. (2025a).*

### 2.1.3 Rapid light-based perturbations support a specific inhibitory role for Myosin in the cell contraction signal network

While ROCK1 is best known for its ability to activate non-muscle Myosin II, it can also phosphorylate and activate the actin nucleator FHOD1, leading to the accumulation of actin filaments. Thus, although the previous results strongly support a specific role for actomyosin as negative feedback regulator in the cell contraction signal network, it was still unclear, if this effect was due to Myosin or due to actin within these structures. To distinguish between these possibilities, perturbations were introduced more rapidly and combined with specific readouts of the Myosin vs actin response kinetics.

Initially, the LOVTRAP system (Wang et al., 2016) was employed, which enabled a rapid manipulation of the effective cytosolic concentration of CA-ROCK1 in individual living cells (FigureS 2A). In this system, CA-ROCK1 is sequestered away from the cytosol to mitochondria in the dark by a fusion with the dark-state binding Zdk1 domain. This domain interacts with the light-oxygen-voltage-sensing (LOV2) domain that is anchored at mitochondria. Illumination with blue light triggers the reversible release of CA-ROCK1 into the cytosol, where it then can act on the cell contraction signal network. In general, these perturbations reduced signal network dynamics, however, the strength of the effect was variable from cell to cell (FigureS 2), presumably due to the relative slow coupling between illumination, release and effect on the signal network. One possible explanation for the slow coupling is that the CA-ROCK1 does not contain a plasma membrane interacting domain. Therefore, the concentration of CA-ROCK1 was high in the cytosol but not as high as needed at the plasma membrane where the cell contraction signaling network in U2OS cells is present. Thus, an optimized perturbation strategy that can introduce a stronger perturbation more rapidly and localized at the plasma membrane would be preferable for a more detailed investigation into the impact of CA-ROCK1 release on Myosin and actin at the plasma membrane.

As ROCK is a signal molecule that acts at the plasma membrane, direct targeting of this molecule to this compartment is expected to be more effective to quickly raise its local concentration compared to releasing a signal molecule from mitochondria into the much larger cytosolic volume. To achieve such a more direct activity control of ROCK, the Molecular Activity Painting (MAP) method was employed (Chen et al., 2017; Kamps et al., 2020). In this method, a protein of interest is recruited to an immobilized artificial plasma membrane receptor upon uncaging of a photo-chemical dimerizer with a focused beam of UV light (Figure 11A and Figure 4). In parallel to this perturbation, a response of an arbitrary fluorescently labeled component can be monitored over time (Figure 4).

Initially, CA-ROCK1 was recruited to the plasma membrane, however, this did not result in a measurable Myosin response (Figure 11B-D). In contrast, if full-length ROCK1 was recruited to the plasma membrane, Myosin II was strongly co-recruited and activated at the perturbation spot (Figure 11F-H). Over the course of this thesis, several additional constructs were developed to enable plasma membrane recruitment of ROCK1 variants [2]. These investigations lead to the insight that the PHC1 domain and/or the coiled-coil domain are essential for plasma membrane targeted ROCK1 to activate non-muscle Myosin II (see Figure 23 in Section 2.2).

[2] See, Figure 23 in chapter 2.2.5 for a more detailed description of the development of ROCK1-based Myosin activation constructs.

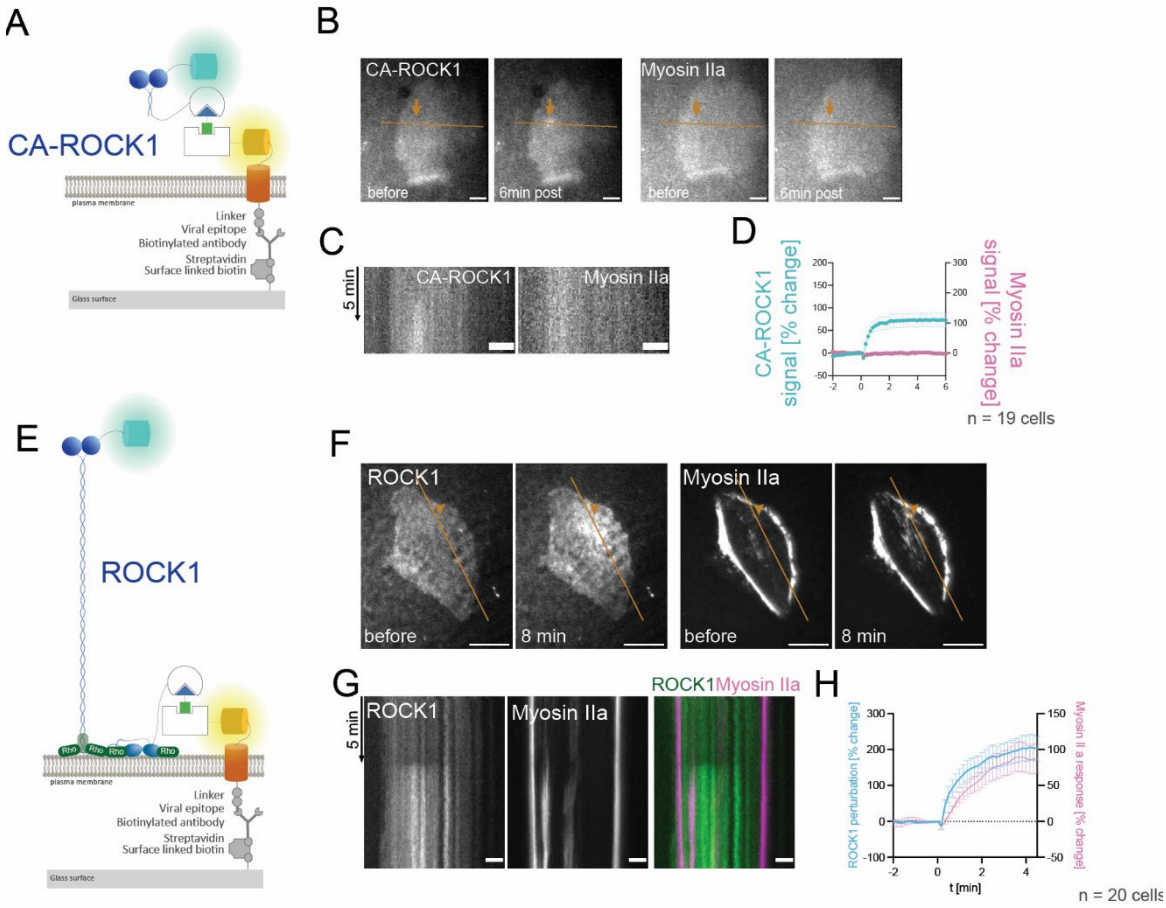


*Figure 11: Light- triggered, rapid plasma membrane targeting of full-length ROCK1 activates Myosin IIa in the cell cortex. (A) Schematic representation of CA-ROCK1 bound to an immobilized artificial receptor using the original Molecular Activity Painting (MAP) method. (B) Representative TIRF images of a cell expressing mTurquoise2-CA-ROCK1-eDHFR (left) and mCherry-non-muscle Myosin heavy chain IIa (right) before and after local photouncaging. Orange arrowheads point to the uncaging position. (C) Kymographs corresponding to the orange lines in B. (D) Quantification of the perturbation of mTurquoise2-CA-ROCK1-eDHFR and the response of mCherry-non-muscle Myosin heavy chain IIa. (E) Schematic representation of full-length ROCK1 bound to an immobilized artificial receptor using the original Molecular Activity Painting (MAP) method. (F) Representative TIRF images of a cell expressing mTurquoise2-ROCK1-eDHFR (left) and mCherry-non-muscle Myosin heavy chain IIa (right) before and after local photouncaging. Orange arrowheads point to the uncaging position. (G) Kymographs corresponding to the orange lines in F. (H) Quantification of the perturbation of mTurquoise2-ROCK1-eDHFR and the response of mCherry-non-muscle Myosin heavy chain IIa. Mean values with standard error of the mean (SEM). Panels B-D are identical to panels B-D middle1 in Figure 23. Figure adapted from Gierse et al. (2025a) and Gierse et al. (2025b).*

While these results clearly demonstrate the performance of the approach, analyzing the effect of a local perturbation at the plasma membrane on signal network dynamics was challenging. This would require accurate measurements of network activity before and after perturbation exclusively at the site of perturbation, as the activity dynamics in the remaining cell area are expected to be unaltered. This is problematic because network activity can occur anywhere in

the cell and the position cannot be predicted. Furthermore, it was unclear which spatial perturbation dimensions would be required to influence signal network dynamics. To address these points, a variant of the MAP-based method was developed, that was named Cell Attachment area - MAP (CA-MAP, Figure 12). In this variant, the uncaging of the photochemical dimerizer occurs in the entire cell attachment area. To achieve this, a UV laser was utilized in TIRF mode to ensure uniform illumination in the entire field of view. Furthermore, to simplify the method, the artificial receptor is not immobilized. This was not expected to be necessary, as lateral diffusion in this configuration would only have a very slow effect on the perturbation concentration in the cell attachment area. Compared to illumination in a single, diffraction limited spot, initial optimization experiments showed that about 3x more laser intensity is required for effective uncaging und ROCK1 plasma membrane recruitment.

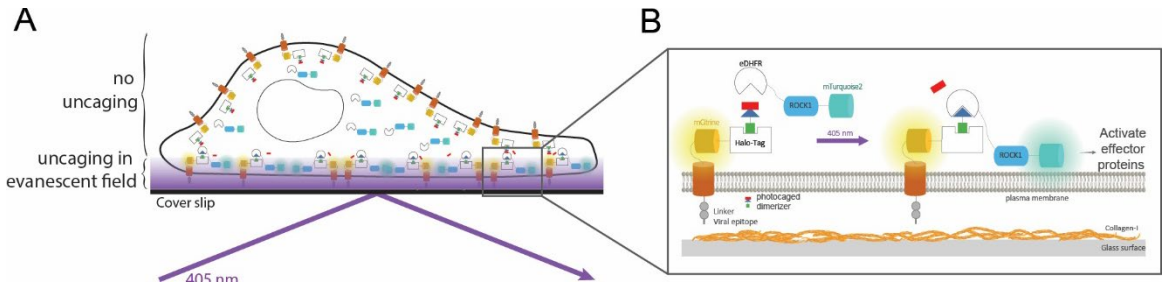


*Figure 12: Schematic representation of Cell Attachment area – Molecular Activity Painting (CA-MAP). (A) Overview representation of CA-MAP activation via TIRF illumination. Illumination occurs only in the evanescent field of the TIRF microscope (magenta gradient), leading to the plasma membrane recruitment of ROCK (cyan boxes). (B) Detailed representation of the components of the CA-MAP approach in this study: Artificial receptors that contain a Halo-Tag are bound to a photocage dimerizer. Uncaging with a 405-nm laser for 400 ms in the entire cell attachment area via TIRF illumination enables the interaction between of the eDHFR domain fused to ROCK1 and the artificial receptor, thereby increasing the local concentration of ROCK1 at the plasma membrane, where it can affect its downstream targets. Figure adapted from Gierse et al. (2025a).*

As shown in Figure 13B-D, the ROCK1 recruitment to the plasma membrane via the CA-MAP method is very robust and immediate. In fact, the increase in ROCK1 signal upon illumination in the example cell shown reached up to 366% and exhibited very fast, switch-like kinetics. The Myosin IIa response to this perturbation was also very robust and started immediately and then exhibited a slow but continuous increase over several minutes (reaching up to 108% in the example cell). The slow increase was expected due to the relatively slow kinetics of Myosin activation and plasma membrane recruitment, which is a multi-step process, that for example includes Myosin polymerization into functional mini-filaments (Beach et al., 2017).

Given this robust Myosin response, the subsequent experiments focused on the question, whether the dynamics of the cell contraction signaling network are influenced by the recruitment of ROCK1 to the plasma membrane. As the perturbation affects the whole cell attachment area, its effect on signal network dynamics can be quantified by similar analysis approaches that were previously published (Graessl et al., 2017) and already used in section 2.1.2. In these experiments, cells were prepared and treated analogously to Figure 13B-C however, rather than measuring the Myosin response, a Rhotekin-based Rho activity sensor was employed as the readout. To ensure accurate quantification of pulsatile signal network dynamics, cells were observed for extended periods of time (20 minutes) both before and after introducing the perturbation. The signal network dynamics were stimulated throughout the entire experiment by the addition of 30 µM nocodazole (Figure 13E-G and K-l). This treatment releases GEF-H1 from microtubules, thereby enabling a larger dynamic range for a potential inhibitory effect.

Similar to the previous experiments shown in Figure 11F-H and Figure 13B-D, the ROCK1 perturbation was again very robust, rapid and strong (Figure 13F-G), and this perturbation had a significant effect on the dynamics of the cell contraction signal network. In particular, rapid ROCK1 perturbation leads to a substantial decrease in the pulse frequency, pulse height, and local standard deviation of the Rho sensor signal (Figure 13L). To ensure that this effect was not caused by the light used for uncaging, an additional control was performed in identical conditions, but in the absence of the photochemical dimerizer (Figure 13H-J and M-N). Analyses of these experiments clearly demonstrate that the observed effect is specific to the recruitment of ROCK1 and subsequent activation of Myosin and not simply caused by the short illumination pulse (Figure 13N). Furthermore, an analysis of the total fluorescence intensity in the cell attachment area revealed a 5% decrease in the baseline of the Rho sensor signal (Figure 13O). This decline is highly significant and again was only observed after the ROCK1 perturbation, and not in the control groups (Figure 13J). This shows that the ROCK1 perturbation does not only inhibit Rho activity dynamics, but also Rho baseline activity, further supporting the idea, that a process that acts downstream of ROCK1 can either directly or indirectly inhibit Rho activity.

As outlined in the introduction (section 1.3.6), actin serves as the feedback mediator in several systems that generate pulsatory dynamics of the cell contraction signal network, e.g. during

early stages of embryonic development in the nematode *C. elegans* and during cytokinesis of *Xenopus leavis* oozytes. To investigate the role of this alternative feedback mediator in adherent, mammalian cells, we used a fluorescently labeled actin construct as readout (Figure 13P-S). Strikingly, although the ROCK1 perturbation leads to a massive increase in Myosin, the overall levels of actin were not elevated, but instead were even significantly diminished by about 5% (Figure 13R-S). This reduction could be explained by the known effect that contractile Myosin forces can break actin filaments (Murrell and Gardel, 2012; Vogel et al., 2013; Vemula et al., 2021), which can expose unstable ends leading to actin depolymerization. The known activation of the formin FHOD1 by ROCK might not be able to compensate for this effect, as this molecule is a very inefficient stimulator of actin filament nucleation and polymerization and has been proposed to predominantly act as an actin crosslinking and capping protein (Schönichen et al., 2013). In addition to this, isoform specific effects of ROCK1 and ROCK2 have been investigated. While ROCK2 seems to stabilize the actin cytoskeleton via phosphorylation of cofilin, ROCK1 does not phosphorylate that protein (Newell-Litwa et al., 2015). Taking together with the other observations presented in this chapter, this result provides very strong, definitive evidence that Myosin, and not actin, is responsible for the observed reduction in cell contraction signal network dynamics. Thus, in contrast to other systems, in which an actin-based process mediates negative feedback regulation in the generation of pulsatory Rho activity and cell contraction dynamics, adherent mammalian cells utilize a different negative feedback mechanism that is dependent on Myosin II.

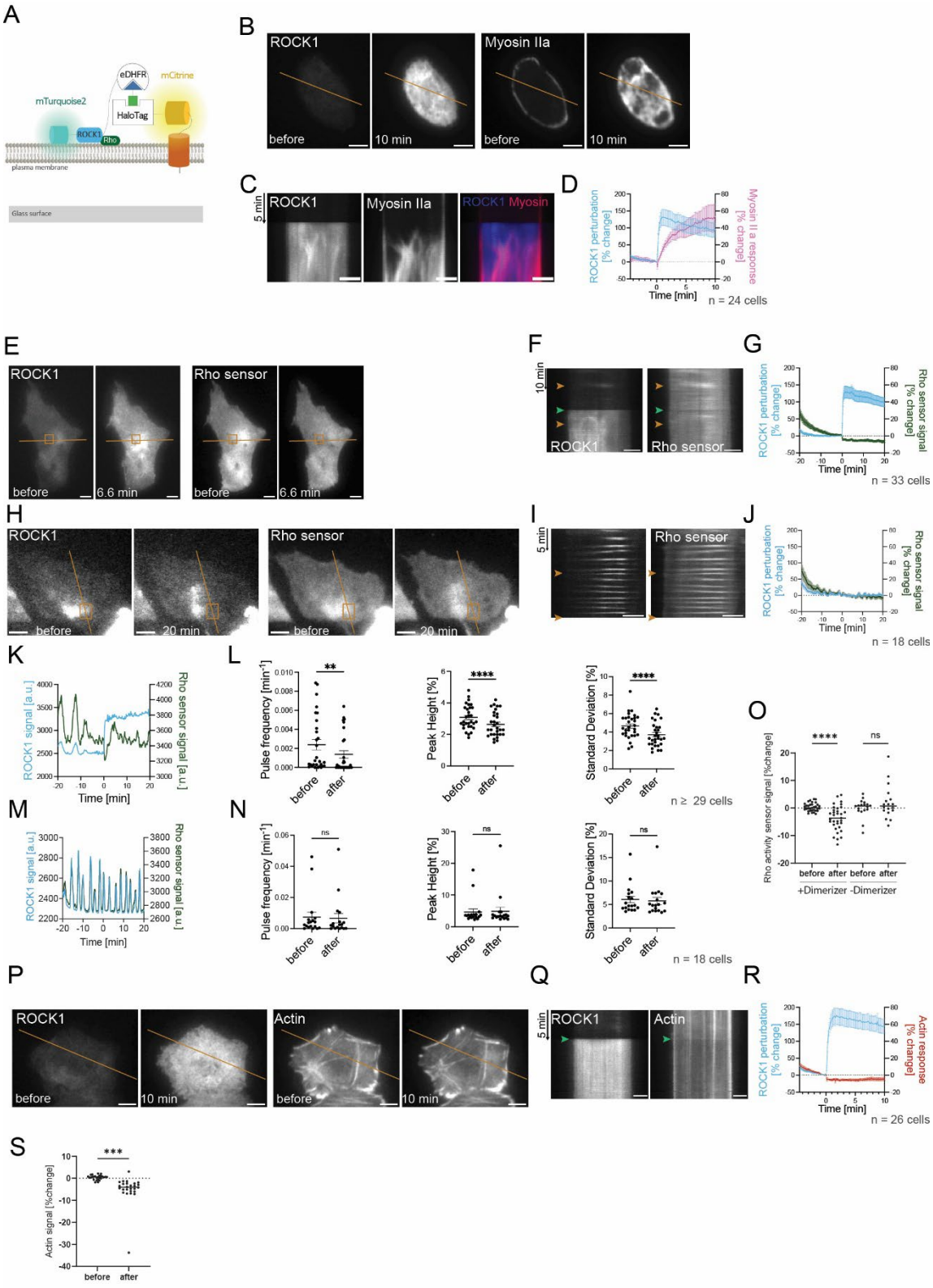


*Figure 13: Light-controlled activation of Myosin IIa rapidly inhibits cell contraction signal network dynamics. (A) Schematic for the recruitment of ROCK1 to artificial receptors at the plasma membrane via Cell Attachment area-MAP (CA-MAP). (B–D) Myosin IIa response to ROCK1 plasma membrane recruitment. (B) Representative total internal reflection fluorescence (TIRF) images of chemo-optogenetic mTurquoise2-ROCK1-eDHFR plasma membrane recruitment and the mCherry-non-muscle Myosin heavy chain IIa response. (C) Kymographs that correspond to the orange lines in B. (D) Quantitative analysis of the co-*

*recruitment of the Myosin IIa construct (mean values with standard error of the mean (SEM); n = 24 cells). (E–J) Analysis of the response of the Rhotekin-based mCherry-Rho activity sensor to ROCK1 plasma membrane recruitment. Experiments were performed in the in the presence (E–G) or absence (H–J) of the photo-dimerizer. (E and H) TIRF images representing the chemo-optogenetic recruitment of mTurquoise2-ROCK1-eDHFR and the response of the mCherry-Rho sensor. (F and I) Kymographs that correspond to the orange lines in E and H, respectively. Orange arrowheads mark the time of the example frames in E and H, and green arrowheads mark the time of ROCK1 plasma membrane targeting, which coincides precisely with an immediate drop in baseline Rho activity levels. (G and J) Quantification of the mCherry-Rho sensor response (mean values with SEM; n = 33 cells for G and n = 18 cells for J). (K–N) Quantitative analysis of cell contraction network dynamics before vs. after light perturbation in cells incubated with dimerizer (K–L) or in control cells without dimerizer (M–N). (K and M) Representative intensity profile plots corresponding to the orange rectangles in E and H, respectively. (L and N) Quantitative analysis of the automated peak analysis of the mCherry-Rho sensor signals. The pulse frequency (left), pulse height (middle), and standard deviation (right) of the Rho activity sensor dynamics were determined before and after light-based perturbation. The standard error of the mean (SEM) was calculated from n ≥ 29 cells in three independent experiments for L and n = 18 cells in three independent experiments for N, and a paired t-test was performed. (O) Quantitative comparison of the fluorescence intensity of the mCherry-Rho sensor at three time points before and three time points after the perturbation. (P–S) Analysis of the actin response to ROCK1 perturbation at the plasma membrane. (P) Representative TIRF images showing the recruitment of mTurquoise2-ROCK1-eDHFR to the plasma membrane and the response of mCherry-Actin. (Q) Kymographs corresponding to orange lines in P. The green arrowheads point to the timepoint at which actin levels drop right after ROCK1 plasma membrane recruitment. (R) Quantification of mCherry-actin response (mean values with standard error of the mean (SEM); n = 26 cells). (S) Quantitative comparison of the fluorescence intensity of mCherry-Actin at three time points before and three time points after the perturbation (paired t-test). In all experiments shown in this figure, cells were treated with 30 µM nocodazole to stimulate cell contraction dynamics. ns: non-significant, **: p < 0.01, ***: p < 0.001, ****: p < 0.0001. Scale bars: 10 µm; 0.26 µm/pixel. Figure adapted from Gierse et al. (2025a).*

## 2.2 The PH domain of ROCK1 interacts with Rho to transduce cell contraction signals

As shown in the previous chapter, Myosin II is a central component of the cell contraction signal network, and it mediates negative feedback to control pulsatile cell contraction dynamics. Furthermore, the Rho kinase ROCK1, that links the activity of Rho and Myosin, also plays a central role in this signaling network, as both its constitutive activation and its inhibition block network activity dynamics. However, during this thesis, it became clear that the mechanism, how ROCK1 is activated by Rho, and how it then transduces this signal to Myosin was still poorly understood. To investigate this mechanism, the spontaneous, pulsatory dynamics of the cell contraction signal network were used as a sensitive readout to investigate how functional manipulations of ROCK1 affect interactions and signal transduction in the control of cell contraction.

### 2.2.1 ROCK1 is dynamically recruited to cell contraction network activity patterns

As discussed in the introduction, previous studies of pulsatile cell contraction dynamics already revealed several insights into the kinetics that link the central components of this system. Due to the rapid positive feedback between GEF-H1 and Rho, the active, plasma membrane bound states of these two components correlate very closely both in space and time at the cell cortex near the plasma membrane with minimal temporal delay (Graessl et al., 2017; Kamps et al., 2020). In contrast, Myosin II plasma membrane recruitment is significantly delayed by about 40s (Graessl et al., 2017), presumably due to the complex multi-step process that acts between active Rho and fully functional, active Myosin II mini-filaments within newly formed actomyosin structures (Beach et al., 2017). These insights were obtained simply by pairwise, parallel measurements of the GEF-H1, Rho activity sensor and Myosin plasma membrane translocation dynamics. In the present study, we employed a similar approach to directly examine the dynamics of the Rho effector ROCK1 during individual cell contraction pulses (Figure 14). Analogous to experiments presented in chapter 2.1, the microtubule-binding deficient GEF-H1 C53R was utilized to stimulate pulsatory cell contraction network activity, thereby enhancing the sensitivity of the analyses (Krendel et al., 2002; Graessl et al., 2017; Kamps et al., 2020). As shown in the middle panels of Figure 14B-D, spatio-temporal plasma membrane recruitment dynamics of the Rho activity sensor and GEF-H1 C53R are identical, what confirmed previous observations (Graessl et al., 2017). For the following studies, GEF-H1 C53R was again employed both as a sensor to measure spatio-temporal Rho activity dynamics and as a stimulator of cell contraction pulses.

The spatio-temporal relationship between Rho and its effector ROCK1 full-length were investigated using this approach (Figure 14B-D, middle2). These experiments clearly demonstrate that, throughout the whole cell attachment area, ROCK1 plasma membrane recruitment closely follows GEF-H1 C53R/active Rho in time and space with minimal temporal delay. Detailed cross-correlation analyses indicate that ROCK1 is maximally recruited at an average of 3.12 $\pm$ 0.56s (mean $\pm$ SEM) after GEF-H1 C53R (Figure 14B-D, middle2). ROCK2 recruitment dynamics showed similar results in an analogous experiment (Figure 14B-D, bottom). This shows that the recruitment of ROCK1 from the cytosol to the plasma membrane

is a very fast process, and that it is not a rate limiting step in the activation of Myosin downstream of Rho activity.

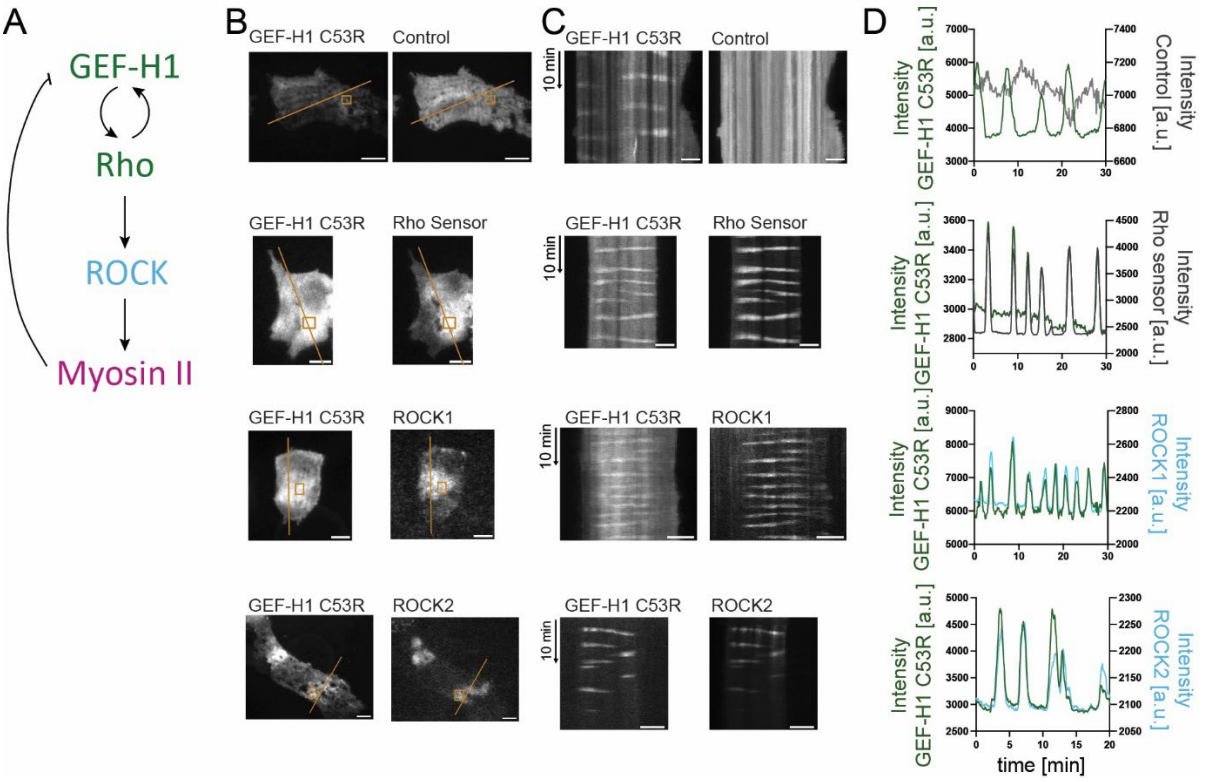


*Figure 14: ROCK1 is dynamically recruited to cell contraction signaling network activity at the plasma membrane. (A) The topology of the cell contraction signal network: The small GTPase Rho gets activated by GEF-H1 and subsequently recruits GEF-H1 to the plasma membrane, thereby closing a positive feedback loop. Rho activates Myosin II via the Rho effector ROCK. Myosin II is thought to mediate negative feedback by competing with binding to the PH domain of GEF-H1. (B) Representative TIRF images of cells expressing the constitutively active GEF-H1 mutant C53R, co-transfected with mCherry as control (top), a Rhotekin GTPase-binding domain (GBD)-based Rho activity sensor (mCitrine, middle1), fluorescently labelled full-length ROCK1 (mCherry-ROCK1 full-length; middle2), or fluorescently labelled full-length ROCK2 (mCherry-ROCK2 full-length; bottom). GEF-H1 was either labelled with mApple (Rho Sensor) or mCitrine (all other conditions). (C) Kymographs corresponding to orange lines in B. (D) Representative intensity profile plots corresponding to rectangular regions of interest in B. B-C middle 1 already shown in Figure 3. Figure adapted from Gierse et al. (2025b).*

Based on the topology of the cell contraction signal network shown in Figure 14A, the local, dynamic recruitment of ROCK1 to active Rho was not surprising. However, a recent study that proposed a new "Molecular Ruler" model for ROCK1 regulation casted doubt on a previously proposed direct interaction between active Rho and ROCK1 (Truebestein et al., 2015). This study was questioning that the previously well-established Rho binding domain (RBD) within its coiled-coil would bind active Rho. Specifically, an *in vitro* binding assay in that study failed to replicate a previously proposed direct interaction between ROCK1 full-length or the RBD

with active Rho, thus casting doubt that ROCK1 and active Rho can interact with each other at all. Furthermore, that study proposed that ROCK would always be constitutively bound to the plasma membrane in a fully extended conformation. In this conformation, the position of the best characterized, most C-terminal RBD within the ROCK coiled-coil would not be able to bind to plasma membrane bound, active Rho (Figure 7B) (Truebestein et al., 2015). These claims in the literature therefore prompted further consideration concerning the tight spatio-temporal cross-correlation between GEF-H1/active Rho and ROCK1 (Figure 14B-D, middle2).

Interestingly, there are other potential Rho-binding sites on ROCK beyond the well-established RBD. This includes two additional binding sites in the coiled-coil. However, in the fully extended ROCK conformation, these sites would be even further away from plasma membrane bound Rho. The PHC1 tandem domain in the extreme C-terminus of ROCK was so far only seen to interact in a non-specific way with negative lipid headgroups at the plasma membrane via clustered positive surface charges (Wen et al., 2008). This domain is composed of a Pleckstrin homology (PH) domain, into which a cysteine-rich (C1) domain is inserted. Interestingly, previous studies in other proteins have shown that both C1 and PH domains are capable of specifically binding the active form of small GTPases. Examples are the interaction between active Ras and the C1 domain of Raf kinase and the interaction between the PH domain of Lbc-type GEFs and RhoA, respectively (Mott et al., 1996; Medina et al., 2013; Graessl et al., 2017; Kamps et al., 2020). Interestingly, in contrast to the other, previously described Rho binding sites in ROCK, an interaction between active RhoA and the PHC1 domain would be compatible with the proposed, extended ROCK1 conformation by Truebestein et al. (2015), and would therefore be able to resolve the conflict that was raised by the “Molecular Ruler hypothesis”.

### 2.2.2 Identification of a novel Rho binding domain in the extreme C-terminus of ROCK

Based on the idea, that the PHC1 tandem domain might interact with active Rho, N-terminally truncated ROCK1 constructs were generated, that lack the previously known GTPase binding domains (GBDs): The homology region 1 (HR1) (Blumenstein and Ahmadian, 2004), the Rho-interacting domain (RID) (Blumenstein and Ahmadian, 2004), and the Rho-binding domain (RBD) (Dvorsky et al., 2004; Tu et al., 2011). First, constructs that contain both the PHC1

tandem domain and the originally identified RBD (RBD-PHC1-ROCK1) or the PHC1 tandem domain alone with a minimal coiled-coil region to ensure its dimerization (dPHC1-ROCK1) were generated (Figure 15A). Thus, the dPHC1-ROCK1 does not contain any of the previously reported Rho binding sites.

Next, the dynamic recruitment of these constructs to cell contraction signal network pulses was measured in U2OS cells. Similar to previous experiments, the dynamics of the cell contraction signal network were stimulated by GEF-H1 C53R expression to increase the Rho activity pulse amplitude and the associated downstream effects. As shown in Figure 15B-D, plasma membrane recruitment of RBD-PHC1-ROCK1 closely correlated with the maximal cell contraction signal network activity indicated by the GEF-H1 C53R signal. This was expected, as RBD-PHC1-ROCK1 contained the best characterized Rho binding site. Interestingly, the further truncated dPHC1-ROCK1 also co-localized with GEF-H1 dynamics, despite lacking any of the previously reported GBDs (Blumenstein and Ahmadian, 2004). This shows that none of the previously characterized GBDs is required for ROCK1 to get recruited by Rho (Figure 15B-D), implying that the remaining parts of ROCK1 are sufficient for this ROCK1 function. The detailed quantitative analysis confirms that both truncations, RBD-PHC1-ROCK1 and dPHC1-ROCK1, exhibit similar pulsatile recruitment dynamics (Figure 15E-F).

In addition to measuring co-recruitment signals of a protein of interest to GEF-H1 localization at the plasma membrane, the presence of a co-expressed protein of interest can also affect the dynamics of the GEF-H1/Rho activity pulses, for example, by interfering with interactions that occur between the components of the cell contraction signal network. Here, the latter can be quantified by measuring the dynamics of the GEF-H1 signals in the presence of the ROCK1 constructs. These measurements showed that ROCK1 wild type has a substantial inhibitory effect on signal network dynamics, while RBD-PHC1-ROCK and dPHC1-ROCK1 did not have such an effect (Figure 15G-H). Based on previous studies, these observations were initially unexpected: Classical experiments observed an inhibitory, dominant negative effect of the PHC1 domain of ROCK on cell contraction (Leung et al., 1996; Ishizaki et al., 1997; Amano et al., 1997). This observation was interpreted in the context of the autoinhibitory model (Figure 7A) what indicates that the C-terminal domain can inhibit the N-terminal kinase domain of ROCK1. However, our own observation that these constructs do not influence oscillatory cell contraction dynamics do not support the autoinhibitory model, and in fact are

contradictory to this idea. Instead, and surprisingly, increasing the expression level of the wild-type molecule, which contains both the N-terminal kinase domain and the C-terminal domain, which should inhibit each other based on the autoinhibitory model, does have a significant inhibitory effect on cell contraction signal network dynamics. As elucidated in section 2.3, this effect is at least partially dependent on crosstalk of ROCK with another Rho family GTPase, which is called Rnd3.

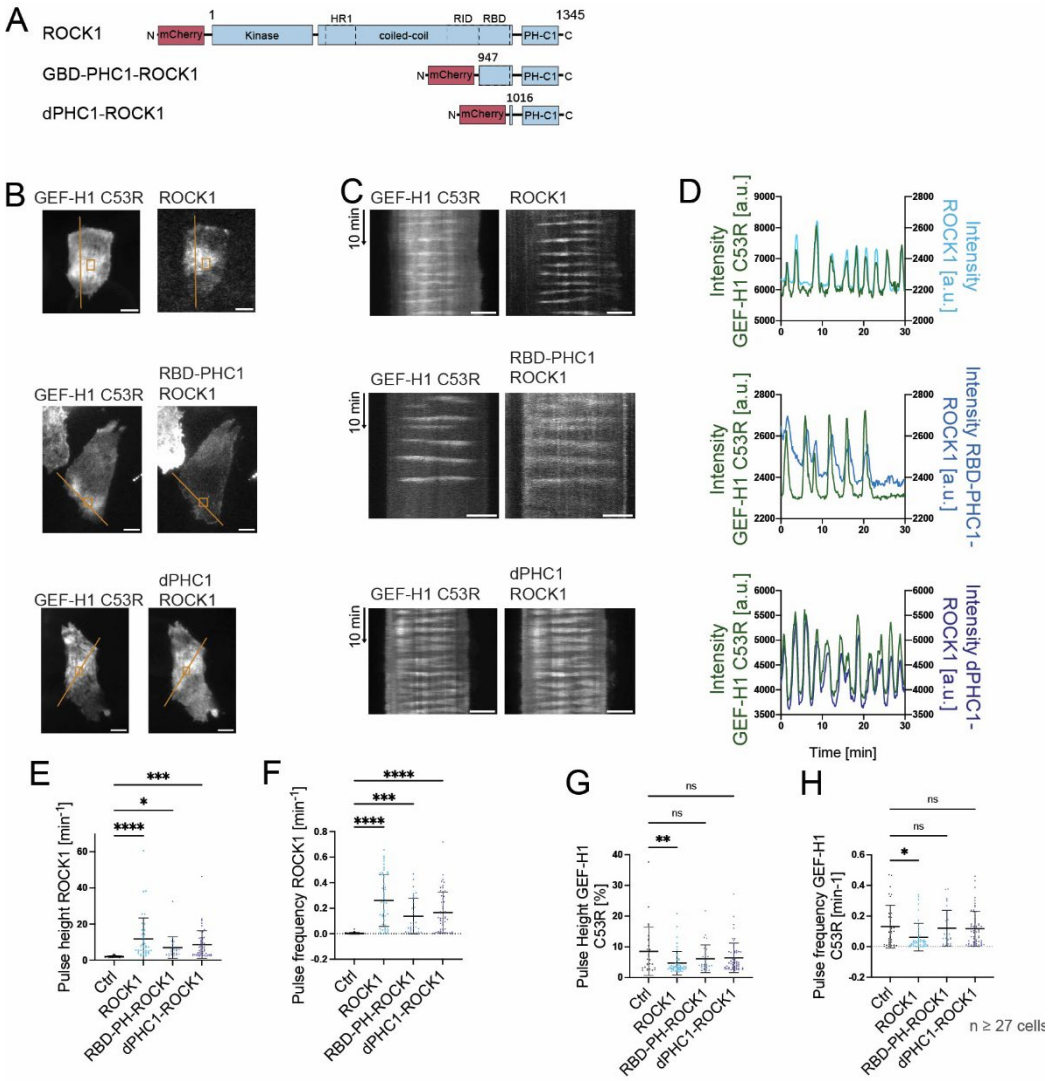


*Figure 15: The previously identified RhoA GTPase binding domains (GBDs) within the coiled-coil domain are not necessary for ROCK1 plasma membrane recruitment. (A) Schematic representation of the ROCK1 constructs used in this study. (C1: phorbol ester/diacylglycerol binding domain, PH: Pleckstrin homology domain, RBD: Rho-binding domain, RID: Rho-interacting domain, HR1: homology region 1). The d prefix indicates a presumed dimeric construct based on the presence of a small residual coiled-coil region. (B) Representative TIRF images of cells expressing mCitrine-GEF-H1 C53R together with mCherry-ROCK1 full-length (top), mCherry-RBD-PHC1-ROCK1 (middle), or mCherry-dPHC1-ROCK1 (bottom). (C) Kymographs corresponding to orange lines in B. (D) Representative intensity profile plots corresponding to the orange rectangles in B. (E-F) Quantitative analyses of the plasma membrane recruitment dynamics of the mCherry-ROCK1 constructs shown in B-D,*

*compared to the mCherry control construct. (G-H): Quantitative analysis of GEF-H1-based signal network dynamics corresponding to mCitrine-GEF-H1 signal changes using the same conditions as shown in E-F. Error bars represent standard error of the mean (SEM) from 3 independent experiments each. ns: non-significant, *: p < 0.05, **: p < 0.01, ***: p < 0.001, ****: p < 0.0001, Dunnett's multiple comparison test, scale bar = 10 µm, 0.26 µm/pixel. Figure adapted from Gierse et al. (2025b).*

In order to identify the minimal Rho binding site in the ROCK1 C-terminus, the small, remaining coiled-coil that was present in the dimeric dPHC1-ROCK1 construct was removed, resulting in the monomeric PHC1 domain (mPHC1, Figure 16A). As demonstrated in Figure 16B-D (top), the mPHC1 domain plasma membrane recruitment exhibits a clear and significant correlation with GEF-H1 signals in both space and time, showing that dimerization via the coiled-coil is not a prerequisite for the recruitment of the PHC1 domain. Furthermore, a more detailed cross-correlation analysis substantiates a robust spatio-temporal correlation between the mPHC1 domain and the GEF-H1/active Rho plasma membrane recruitment signals (Figure 16D).

Given the established propensity of the PH and C1 domains of other proteins to bind small GTPases (Mott et al., 1996; Medina et al., 2013; Kamps et al., 2020; Powis et al., 2023), the tandem domain was dissected to isolate the individual monomeric PH (mPH-ROCK1) and C1 (mC1-ROCK1) domains (Figure 16A). These experiments showed that the mC1-ROCK1 domain did not exhibit any measurable signal changes in correlation with GEF-H1/Rho (Figure 16B-D, bottom). Furthermore, the mPH-ROCK1 was only marginally enriched at local GEF-H1/Rho signals (Figure 16B-D, middle). The automated quantitative analysis corroborated these observations: mC1-ROCK1 pulse height measurements were comparable to the negative control, and mPH-ROCK1 exhibited a very small positive trend which was not significantly different from the negative control (Figure 16E-F). This indicates that both domains are indispensable and act together for the efficient plasma membrane recruitment of ROCK1's C-terminal region.

Furthermore, no observable decrease in network activity was detected in response to the expression of mPHC1-, mPH-, or mC1-ROCK1. The pulse height and pulse frequency of GEF-H1 C53R remained unchanged in comparison to the control group. Taken together with the previous results (Figure 15 G-H), neither the intact PHC1 domain, nor the constituent PH or C1 domains (Figure 16G-H) exert any detectable dominant negative effect on pulsatile cell contraction dynamics.

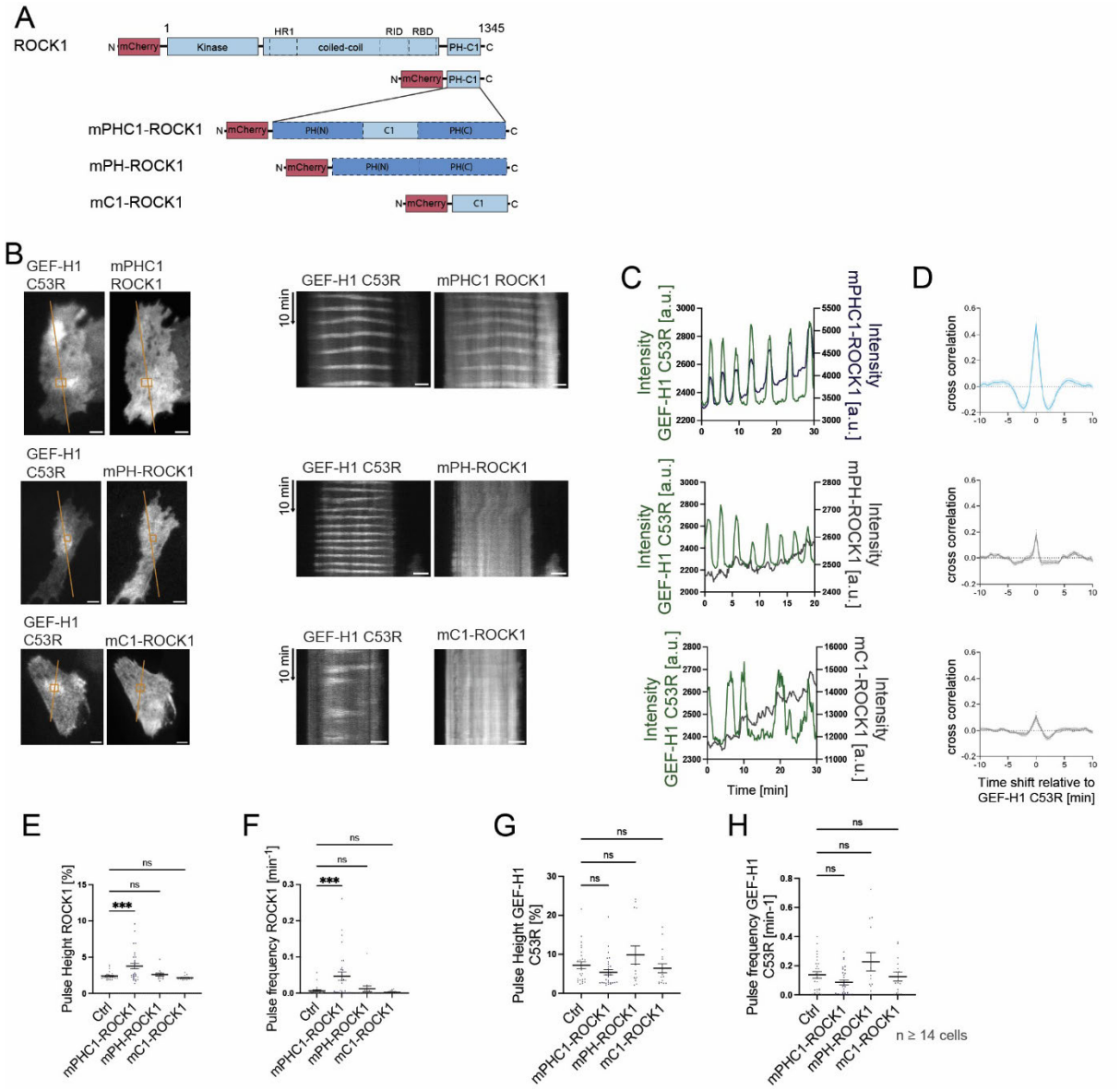


*Figure 16: The PH and C1 domains are both required for efficient ROCK1-PHC1 recruitment to active Rho. (A) Schematic representation of the ROCK1 constructs used in this study (C1: phorbol ester/diacylglycerol binding domain, PH: Pleckstrin homology domain, RBD: Rho-binding domain, RID: Rho-interacting domain, HR1: homology region 1). The m prefix indicates a presumed monomeric construct based on the absence of a coiled-coil region. (B) Representative TIRF images of cells expressing mCitrine-GEF-H1 C53R together mCherry-mPHC1-ROCK1 (top), mCherry-mPH-ROCK1 (middle), or mCherry-mC1-ROCK1 (bottom). Kymographs correspond to orange lines in B. (C) Representative intensity profile plots corresponding to the orange rectangles in B. (D) Mean cross correlation of the different ROCK1 variants with respect to GEF-H1 C53R localization. (E-F) Quantitative analysis of the plasma membrane recruitment dynamics of the mCherry-ROCK1 constructs shown in panels B and C, compared to the empty parental mCherry control construct. (G-H) Quantitative analysis of GEF-H1-based signal network dynamics corresponding to mCitrine-GEF-H1 C53R signal changes using the same conditions as shown in E-F. Error bars represent standard error of the mean (SEM) from 3 independent experiments each. ns: non-significant, *: $p < 0.05$, **: $p < 0.01$, ***: $p < 0.001$, ****: $p < 0.0001$, Dunnett's multiple comparison test, scale bar = 10 µm, 0.26 µm/pixel. Figure adapted from Gierse et al. (2025b).*

### 2.2.3 Alphafold predicted point mutations in the ROCK1 PH domain disrupt its interaction with active Rho

To further investigate the recruitment of mPHC1 ROCK1 to cell contraction network activity, AlphaFold2 was employed to predict potential interactions with a set of distinct small GTPases. Indeed, an interaction between GTP-bound Rho family GTPases and the mPHC1 domain was predicted with high confidence (Figure 17E). Specifically, the interface predicted template modeling score (ipTM) for the most studied members of the RhoA subgroup RhoA, RhoB, and RhoC, exhibited a consistently higher value than the 0.8 threshold frequently employed to differentiate between true and false positives (Figure 17E). In contrast, predictions of interactions with GTPases belonging to more distant Rho family members or with the Ras, Rap, and Rab families failed to consistently reach this confidence level.

To experimentally validate this prediction, a Protein Interfaces, Surfaces and Assemblies (PISA) analysis was conducted by Ingrid Vetter (MPI Dortmund). This analysis was designed to identify amino acid pairs that are most critical for the interaction between the two proteins. The four amino acids predicted by PISA are highly conserved as shown by the sequence alignment of ROCK1 and ROCK2 PH domains from different species using a *Clustal 2.1 multiple sequence alignment* (Figure 17D). This suggests that the binding site for Rho at the ROCK1 PH domain has played a pivotal role in evolution, indicating that it might also contribute to the recruitment of ROCK1 or the related ROCK2 isoform in a variety of other species.

Subsequently, the corresponding amino acids in the PHC1 domain were substituted to disrupt the predicted interaction based on steric and electrostatic properties. Importantly, these substitutions were chosen to have a minimal impact on the structure of the PHC1 domain. The following substitutions were identified, listed in order according to the anticipated inhibitory effect on the interaction: The A1291R, F1174A, L1199A, and E1203K (Figure 17C). To optimally investigate their impact, two independent, non-overlapping sets of mutants were chosen (mutA$^{PH}$ and mutB$^{PH}$), as well as a combination of the two (mutC$^{PH}$). Proteins harboring these mutations were investigated for their recruitment to GEF-H1/Rho activity signal dynamics at the plasma membrane.

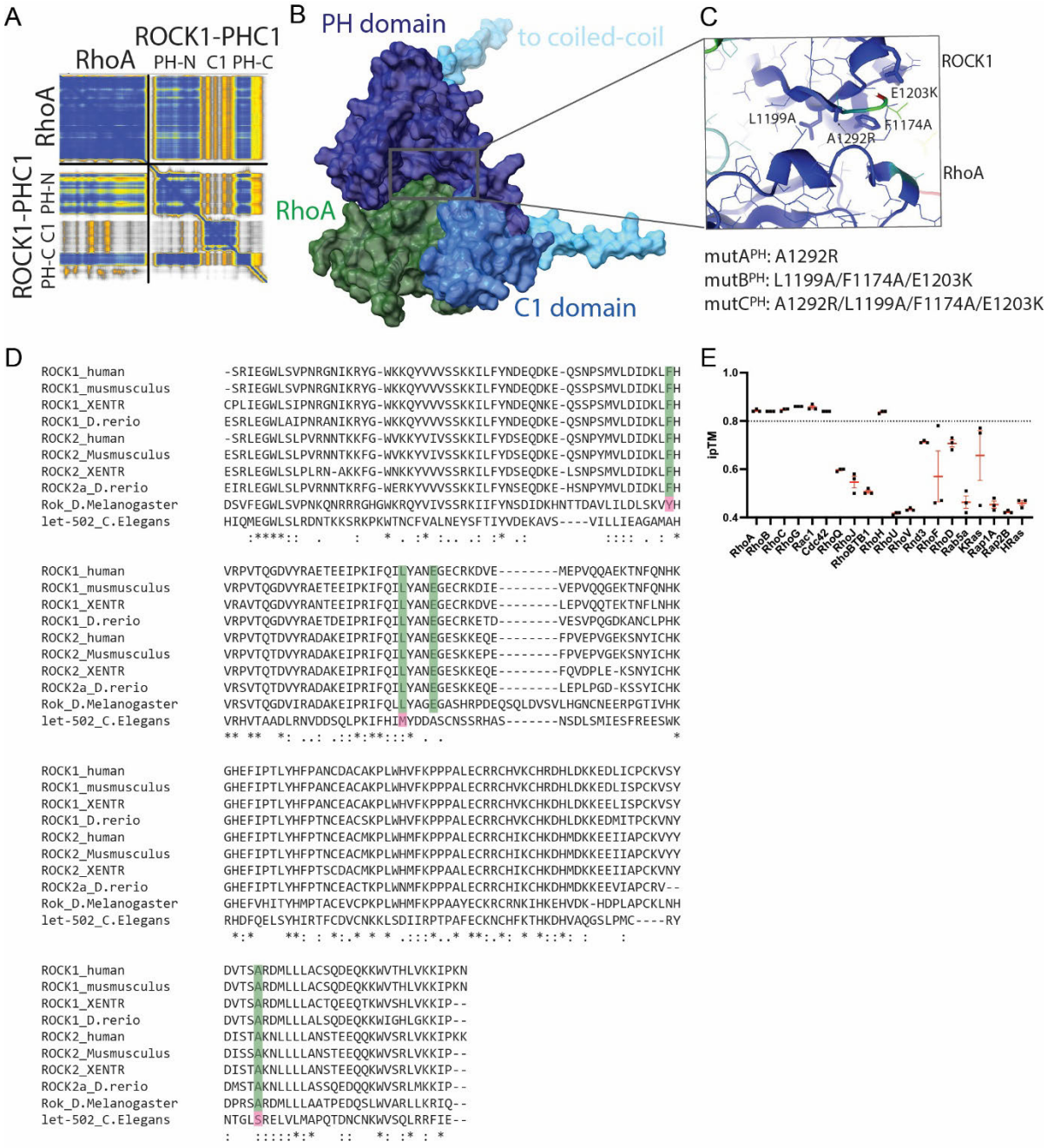


*Figure 17: Alphafold-based prediction of the complex between active Rho and the ROCK1 PHC1 domain. (A) The predicted aligned error (PAE) plot for the PHC1:RhoA complex. (B) AlphaFold2 predicted structure of the PH:RhoA complex (green: RhoA, blue: PHC1-tandem domain). (C) Magnified view of the predicted binding interface of the ROCK1 PH domain and RhoA. The amino acids predicted to be most critical for the interaction, as determined by Protein Interfaces, Surfaces and Assemblies (PISA) analysis, are highlighted. (D) Protein sequence alignment of the ROCK1 PHC1 domain and analogous domains from several other species obtained via the Clustal 2.1 multiple sequence alignment web tool. (E) The Interface Predicted Template Modeling (ipTM) score of various GTPases in their GTP-bound state in complex with the ROCK1 PHC1 tandem domain obtained via AlphaFold3 predictions. The dashed line represents the 0.8 threshold that typically distinguishes true from false positives. Figure adapted from Gierse et al. (2025b).*

These experiments demonstrated that the two independent sets of mPHC1 domain mutations (mutA$^{PH}$ and mutB$^{PH}$), both by themselves and in combination (mutC$^{PH}$) lead to a substantial decrease in recruitment to GEF-H1/Rho signal dynamics. Quantitative peak analysis demonstrated that all three mutants exhibited strongly diminished peak frequency and amplitude in comparison to the non-mutated mPHC1-ROCK1 domain, which served as the control (Figure 18E-F).

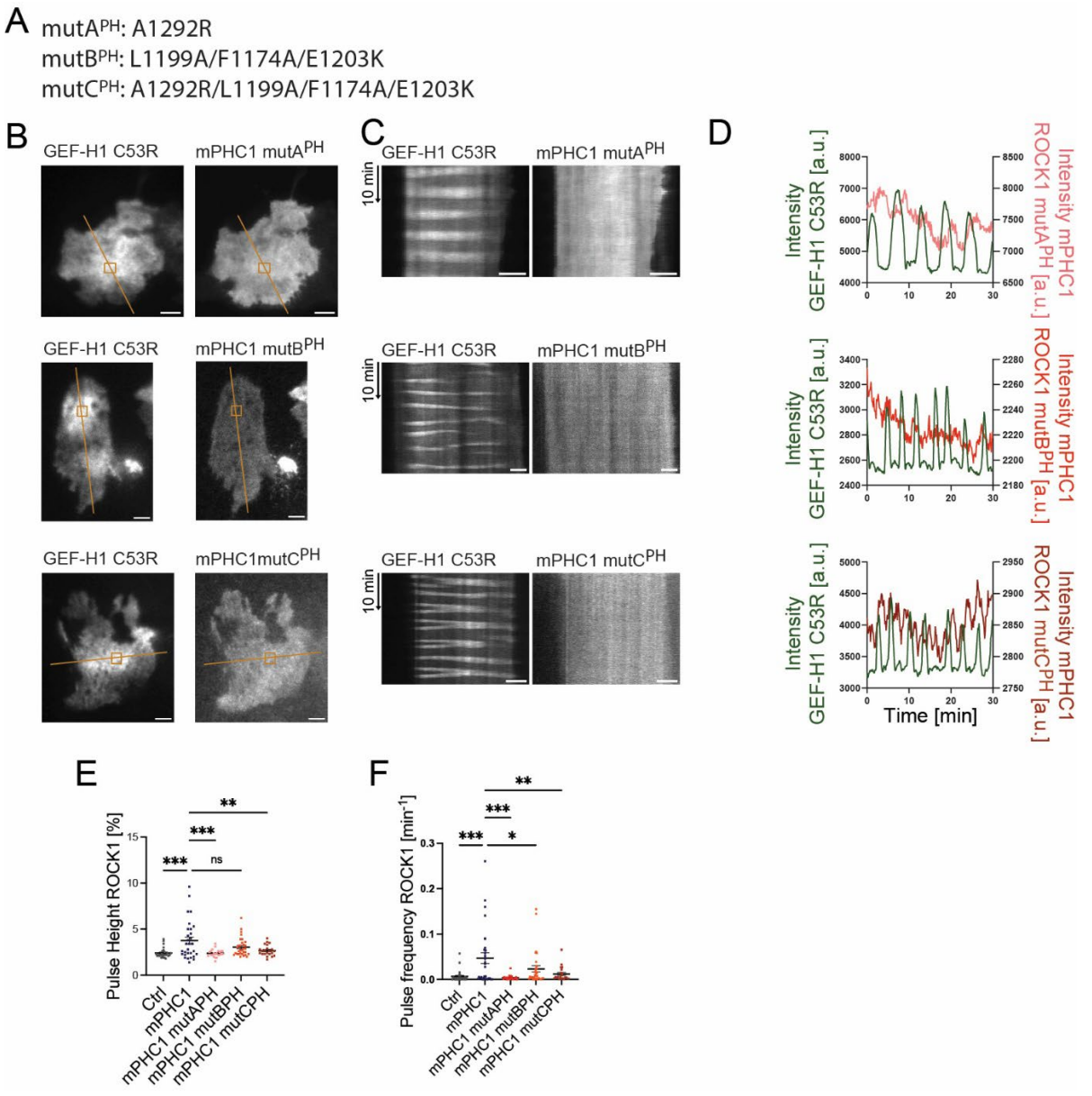


*Figure 18: Point-mutations based on the Alphafold-predicted PHC1:Rho complex structure disrupt ROCK1 PHC1 domain recruitment to GEF-H1/active Rho dynamics at plasma membrane. (A) Nomenclature for the PH domain mutants. (B) Representative TIRF images of cells expressing either mCherry-mutA$^{PH}$ (top), mCherry-mutB$^{PH}$ (middle), or mCherry-mutC$^{PH}$ (bottom) together with mCitrine-GEF-H1 C53R. (C) Kymographs corresponding to lines in B. (D) Representative intensity profile plots corresponding to the orange rectangles in B. (E-F) Quantitative analysis of mCherry-ROCK1 constructs plasma membrane*

*recruitment dynamics. Error bars represent standard error of the mean (SEM) from 3 independent experiments each. ns: non-significant, *: p < 0.05, **: p < 0.01, ***: p < 0.001, Dunnett's multiple comparison test, scale bar = 10 µm, 0.26 µm/pixel. Figure adapted from Gierse et al. (2025b).*

The experiments above clearly show that the PHC1 domain is recruited to GEF-H1/Rho activity pulses in the cell contraction network and that this recruitment is dependent on individual amino acids in the PH domain, that were predicted based on AlphaFold2 to contribute most to a PHC1/active Rho complex. However, these observations are based on correlation and therefore do not show a causal link between GEF-H1/Rho activity and the PHC1 domain. To investigate a potential causal link, the Molecular Activity Painting Method (MAP, see Figure 4 and methods section 7.5 for a more detailed description) (Chen et al., 2017; Kamps et al., 2020) was employed again. Initially, it was attempted to induce a direct binding of mPHC1 to various Rho molecules: RhoAΔCAAX Q63L, RhoAΔCAAX, RhoCΔCAAX, and RhoA. Unfortunately, none of these molecules recruited mPHC1 (data not shown). During the troubleshooting process, we identified a potential underlying cause of this issue: the various Rho variants were unable to activate the signaling network when they are forced to the plasma membrane when bound to eDHFR. In fact, as demonstrated in Figure 19A-C top, the recruitment of Rho does not result in the activation of Myosin, showing that the enforced plasma membrane enrichment of wild-type or mutant RhoA constructs via this method is not sufficient to induce the phenotype of active Rho. A potential reason for this is that enforced plasma membrane targeting of these Rho molecules might sterically interfere with their normal function, or that the proper interaction of Rho with plasma membrane bound effectors might be disrupted.

Previous research in the lab has demonstrated that the plasma membrane recruitment of the Rho activator GEF-H1 C53R leads to the strong and local activation of the cell contraction signaling network, by local recruitment and activation of endogenous Rho. Subsequently, this also leads to the efficient activation of the Rho downstream target Myosin II (Kamps et al., 2020; Kowalczyk et al., 2022). As shown in Figure 19A-C (bottom), this effect was confirmed again in this thesis, demonstrating that the enforced, local enrichment of GEF-H1 C53R via the molecular activity painting method strongly and locally activates Myosin. Furthermore, also in agreement with previous studies (Kamps et al., 2020; Kowalczyk et al., 2022), the Myosin response was transient, further supporting the idea, that it acts as a negative feedback mediator to control GEF-H1/Rho activity.

Upon the recruitment of GEF-H1 C53R to the plasma membrane, a similar, local and transient increase in the mPHC1-ROCK signal was observed, thereby clearly confirming a causal link between mPHC1 plasma membrane recruitment and the cell contraction signal network activity (Figure 19D-F, top). Furthermore, analogous experiments with the quadruple (mutC$^{PH}$) mPHC1 mutant did not lead to any detectable local enrichment to local GEF-H1 C53R perturbations (Figure 19D-F, middle). Statistical analysis confirms that the recruitment of mPHC1 to the induced network activity differs significantly both compared to an empty control readout construct as well as compared to the quadruple mutant mPHC1 mutC$^{PH}$ (Figure 19H).

It should also be noted here, that previous studies showed that the Rho activity response to sustained GEF-H1 perturbations is transient (Kowalczyk et al., 2022). The reason for these transient responses is the negative feedback regulation of the cell contraction signal network, which quickly inhibits Rho activity amplification, and is thus also expected to affect Rho downstream targets, such as the ROCK PHC1 domain.

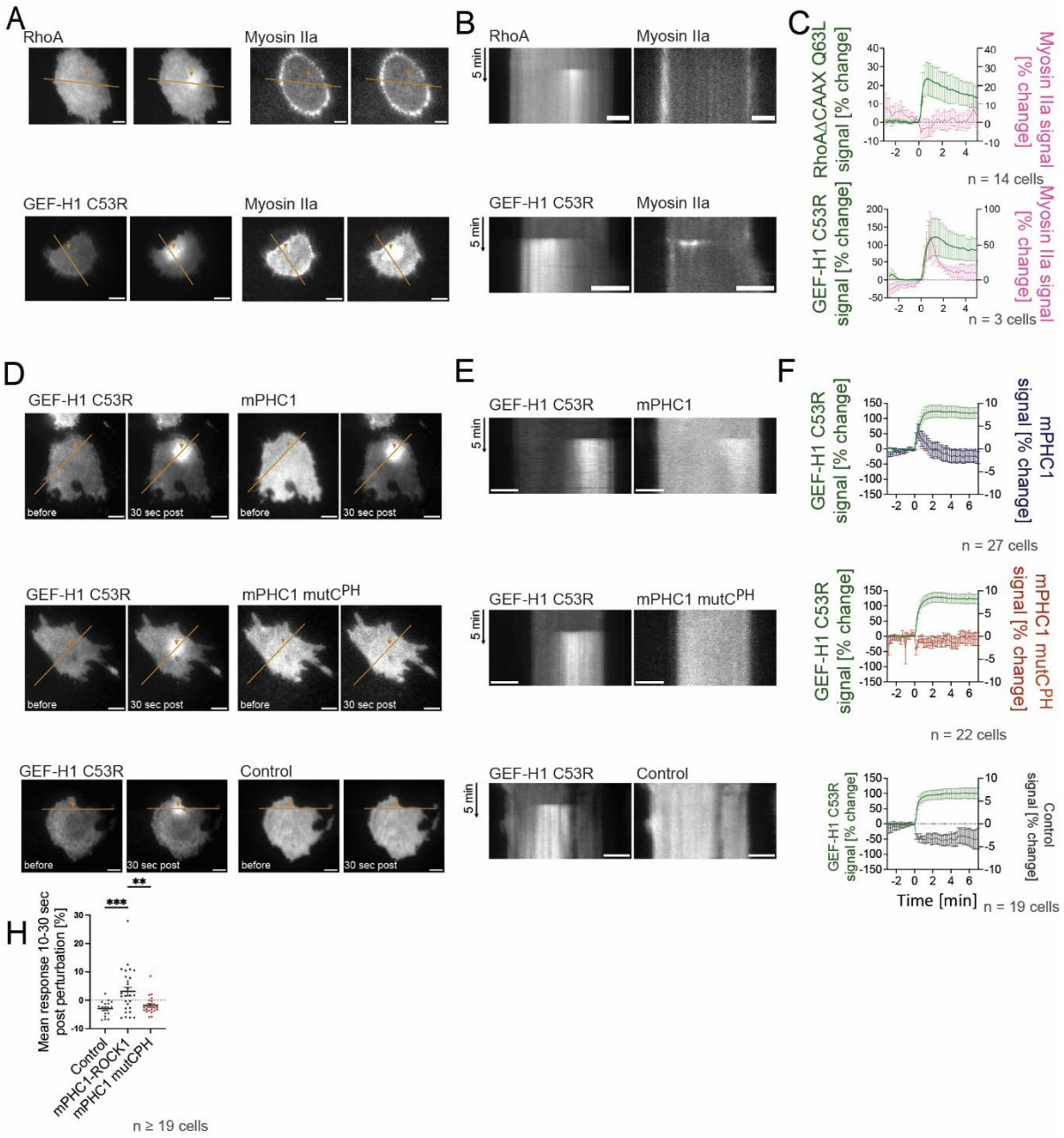


*Figure 19: Light induced rapid activation of the cell contraction signal network leads to plasma membrane recruitment of the mPHC1 ROCK1 domain. (A) Representative TIRF images of cells co-expressing either the RhoAQ63LΔCAAX perturbation construct (top left, mTurqoise2) or the GEF-H1 C53R perturbation construct (bottom left, mTurqoise2) and non-muscle Myosin II heavy chain to measure the response (right, mCherry). (B) Kymographs corresponding to lines in A. (C) Kinetics of mean fluorescence signals of all cells measured at the perturbation spot (indicated by orange arrows in A). (D) Representative TIRF images of cells that express the GEF-H1 C53R perturbation construct (left, mTurqoise2) and either mPHC1 (top right, mCherry), mPHC1 mutC$^{PH}$ (middle right, mCherry), or the empty parental mCherry control construct (bottom right, mCherry). (E) Kymographs corresponding to lines in D. (F) Kinetics of mean fluorescence signals of all cells measured at the perturbation spot (indicated by orange arrows in D). (H) Quantitative analysis of the mPHC1 and control construct responses 10-30s after the onset of light induced GEF-H1 perturbations. Error bars represent standard error of the mean from 3 independent experiments each. **: p < 0.01, ***: p < 0.001, Dunnett's multiple comparison test, scale bar = 10 µm, 0.26 µm/pixel. Figure partly adapted from Gierse et al. (2025b).*

### 2.2.4 The PH domain and the Rho binding domain in the coiled-coil both participate in the recruitment of full-length ROCK1 to cell contraction signal network dynamics

Next, we investigated the relevance of the PHC1 domain for the function of full-length ROCK1. First, we introduced the mutC$^{PH}$ point mutations into the PHC1 domain of ROCK1 full-length to specifically and selectively inhibit the ability of the PHC1 domain to interact with active Rho. We then investigated if these mutations influence dynamic ROCK1 full-length recruitment to cell contraction pulses. Figure 20A-C (bottom) demonstrates that ROCK1 full-length mutC$^{PH}$ still exhibits pulsatile behavior that correlates closely with GEF-H1 in both space and time. This is probably due to the presence of the different, previously characterized Rho binding sites (Blumenstein and Ahmadian, 2004; Dvorsky et al., 2004; Tu et al., 2011). Nonetheless, an examination of the peak height indicated a tendency in which the recruitment of this mutant to GEF-H1 at the plasma membrane was less efficient ($p = 0.3791$, Figure 20D). Furthermore, the more sensitive measurement for signal dynamics based on the local standard deviation of fluorescence intensity signals was able to detect significantly diminished temporal recruitment dynamics of the ROCK1 full-length mutC$^{PH}$ compared to the non-mutated ROCK1 full-length (Figure 20E). Taken together, these measurements show that the newly identified RhoA binding domain can significantly contribute to ROCK1 plasma membrane recruitment.

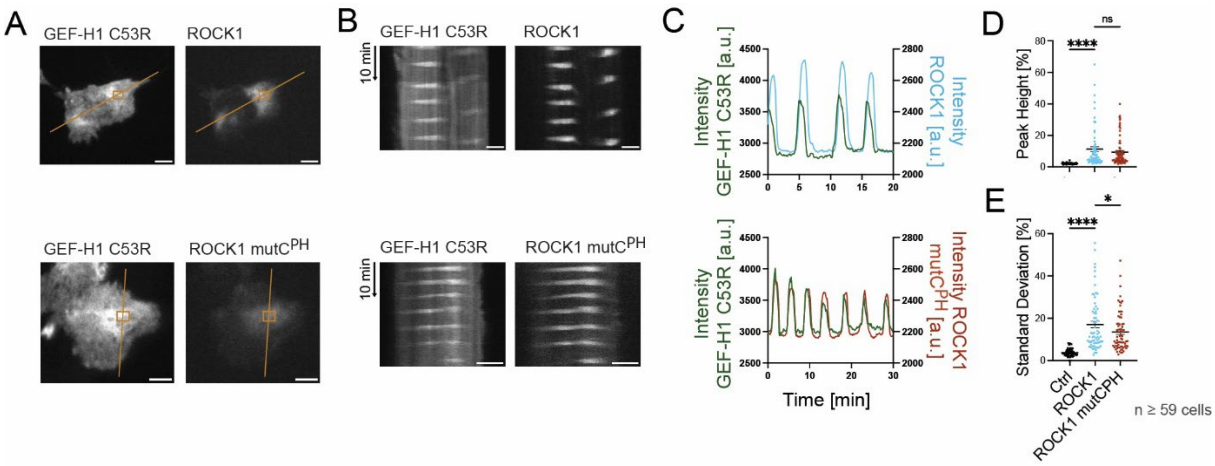


*Figure 20: The intact PHC1 domain is required for efficient recruitment of full-length ROCK1 to cell contraction signal network activity dynamics. (A) Representative TIRF images of cells expressing mCitrine-GEF-H1 C53R together with mCherry-ROCK1 (top) or mCherry-ROCK1 mutC$^{PH}$ (bottom). (B) Kymographs corresponding to lines in A. (C) Representative intensity profile plots corresponding to the orange rectangles in A. (D-E) Quantitative analysis of recruitment dynamics to the plasma*

*membrane (pulse height: p=0.379; local standard deviation over time: p=0.0465) of the mCherry-ROCK1 constructs shown in A-C. An empty parental mCherry construct was used as a control in panels D-E. ns: non-significant, *: p < 0.05, ****: p < 0.0001, Dunnett's multiple comparison test, scale bar = 10 µm, 0.26 µm/pixel. Figure adapted from Gierse et al. (2025b).*

To evaluate the impact of the PHC1 domain for ROCK1 recruitment, we also investigated the functional role of the previously identified RBD, which is the best characterized of the previously known Rho binding sites on ROCK. The Asn1004Thr and Lys1005Thr mutations reported in Leung et al. (1996) were demonstrated to prevent RhoA binding to this RBD domain, thereby providing a rationale for utilizing these mutations.

We first mutated the isolated RBD domain to verify these earlier reports, and indeed, the mutated RBD was not recruited to GEF-H1/Rho activity pulses at the plasma membrane. In contrast, the non-mutated RBD strongly correlated with GEF-H1/Rho activity pulses (Figure 21).

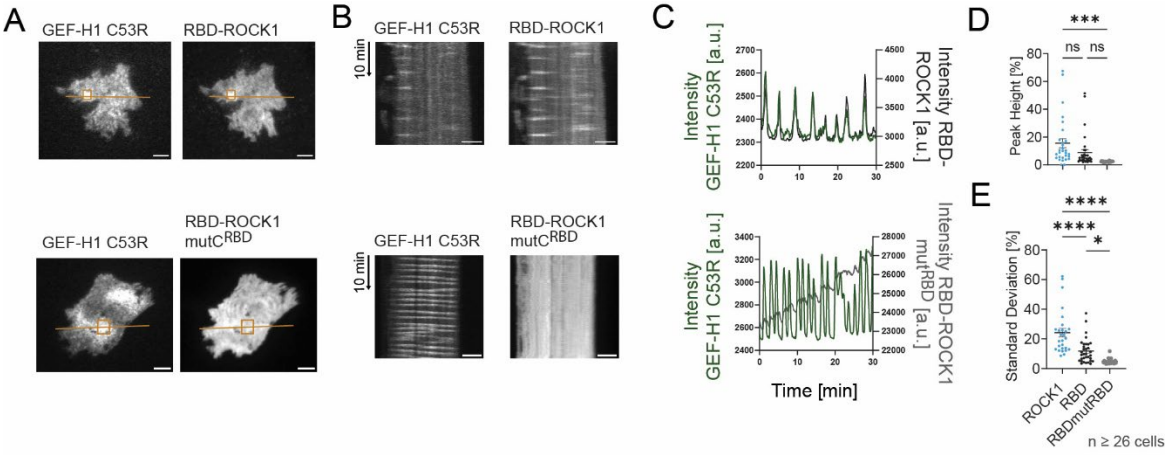


*Figure 21: Asn1004Thr and Lys1005Thr mutations (RBDmut$^{RBD}$) within the ROCK1-RBD disrupt its interaction with active Rho. (A) Representative TIRF images of cells expressing mCherry-ROCK1 RBD domain (top), mCherry-ROCK1 RBDmut$^{RBD}$ domain (bottom) together with mCitrine-GEF-H1 C53R. (B) Kymographs corresponding to lines in A. (C) Representative intensity profile plots corresponding to the orange rectangles in A. (D-E) Quantitative analysis of mCherry-ROCK1 constructs plasma membrane recruitment dynamics. ns: non-significant, *: p < 0.05, ***: p < 0.001, ****: p < 0.0001, Ordinary one-way ANOVA, scale bar = 10 µm, 0.26 µm/pixel. Adapted from Gierse et al. (2025b).*

Introducing these mutations in the ROCK1 full-length protein (Figure 22A-C, middle) led to a substantial decrease in its recruitment to GEF-H1 C53R/active Rho pulses. However, plasma membrane recruitment of this mutated construct (ROCK1mut$^{RBD}$) was still detectable, showing that the remaining parts of ROCK1 were still able to selectively bind to GEF-H1 C53R/active Rho pulses. To address this, a full-length ROCK1 mutant was engineered that contains both the mut$^{RBD}$ mutations and the mutC$^{PH}$ mutations. As demonstrated in Figure

22A-C (bottom), the recruitment of this construct to GEF-H1 C53R/active Rho was almost completely ablated, showing that the RBD and the PHC domain synergistically contribute to ROCK1 full-length recruitment to cell contraction signal network activity.

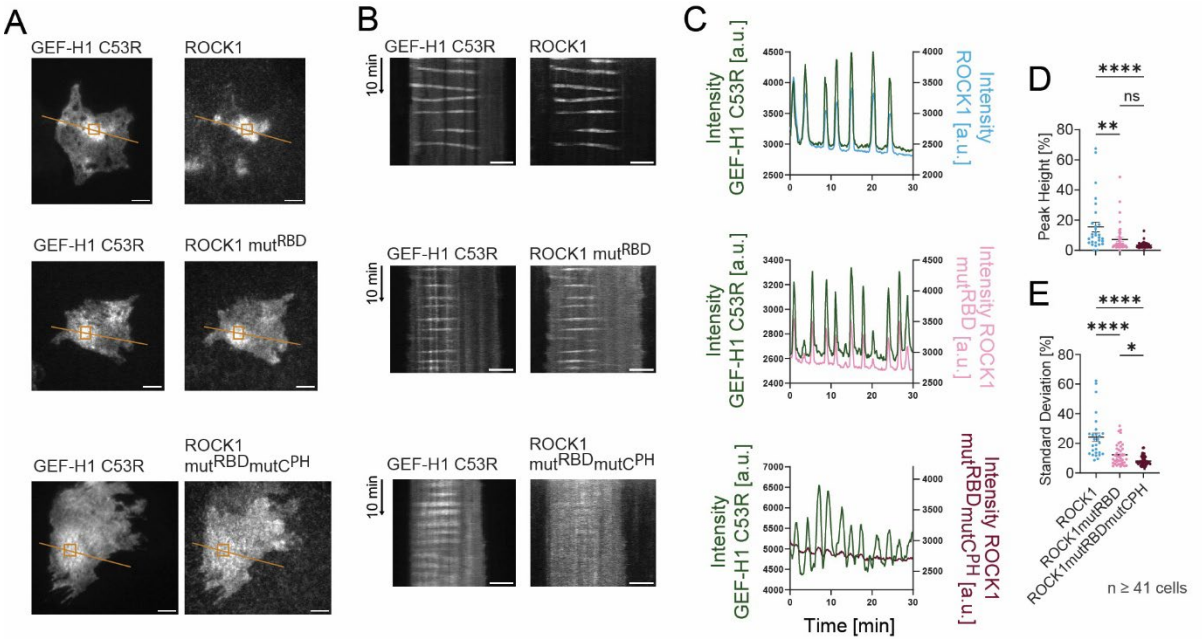


*Figure 22: The ROCK1 RBD and PHC domains synergistically contribute to the recruitment of full-length ROCK1 to cell contraction signal network activity. (A) Representative TIRF images of cells expressing mCherry-ROCK1 (top), mCherry-ROCK1 mut$^{RBD}$ (middle), or mCherry-ROCK1mut$^{RBD}$mutC$^{PH}$ (bottom) together with mCitrine-GEF-H1 C53R. (B) Kymographs corresponding to lines in A. (C) Representative intensity profile plots corresponding to the orange rectangles in A. (D-E) Quantitative analysis of plasma membrane recruitment dynamics of the mCherry-ROCK1 construct shown in A-C. Data in the column for full-length ROCK1 recruitment dynamics are identical to data shown in Figure 21. ns: non-significant, *: p < 0.05, **: p < 0.01, ****: p < 0.0001, Ordinary one-way ANOVA, scale bar = 10 µm, 0.26 µm/pixel. Figure adapted from Gierse et al. (2025b).*

### 2.2.5 The PHC1 tandem domain is essential for ROCK1 to activate Myosin at the cell cortex

The previous experiments showed that the PHC1 domain contributes significantly to the plasma membrane recruitment of ROCK1. This raised the question, which role this domain might have in the ability of ROCK1 to transduce Rho activity signals into the activation of Myosin. To independently examine the effect of this domain on plasma membrane recruitment and on Myosin activation, the Molecular Activity Painting assay was employed again (Chen et al., 2017; Kamps et al., 2020). Basically, by enforcing plasma membrane targeting of ROCK1 via this method in an autonomous manner, the effect of different ROCK1 constructs at the plasma membrane on the subsequent Myosin II activation can be measured

and compared. Enforcing the plasma membrane targeting of non-mutated, ROCK1 full-length via this method led to a substantial increase in Myosin IIa at the plasma membrane. This shows that simply increasing the local concentration of ROCK1 at the plasma membrane is sufficient to increase local ROCK1 activity towards Myosin II (Figure 23B-D, top).

Interestingly, enforcing the plasma membrane targeting of the constitutively active, C-terminally truncated CA-ROCK1 construct did not lead to any noticeable local Myosin II activation. This observation provides direct support for the molecular ruler model that was previously suggested by Truebestein et al. (2015), which suggested that the full-length coiled-coil domain, which is largely absent in CA-ROCK1, is essential to bridge the distance between Myosin II in the dense cell cortex and the plasma membrane.

Next, the significance of the PHC1 domain for localized ROCK1 function at the plasma membrane was investigated. As illustrated in Figure 23C-D (middle2), deleting the PHC1 tandem domain strongly interferes with the ability of ROCK1 to effectively activate Myosin. While the recruitment efficiency of ROCK1 and of ROCK1$\Delta^{PHC1}$ to the plasma membrane was comparable via molecular activity painting, in fact, Myosin activation was nearly abolished in response to the ROCK1$\Delta^{PHC1}$ mutant. This demonstrates that the PHC1 domain is an important and essential component of ROCK1 for its ability to activate Myosin.

Next, plasma membrane targeting of ROCK1 full-length that harbors the mutC$^{PH}$ mutations was enforced to more specifically investigate the role of the PHC1:Rho interaction in the activation of Myosin. As ROCK1 is a downstream effector of Rho, it was originally expected that these mutations would reduce the efficiency Myosin II activation by ROCK1. However, surprisingly, the Myosin response was markedly increased in the presence of these mutations (Figure 23B-D, bottom). In fact, despite the comparable recruitment of both the mutated and non-mutated forms of ROCK1 full-length, a more than threefold increase in the Myosin IIa response was observed in the presence of these mutations (compare Figure 23D top and bottom). Furthermore, simple over-expression of ROCK1 full-length mutC$^{PH}$ exhibited a more pronounced stimulatory effect on the formation of contractile F-actin structures compared to its non-mutated full-length counterpart (Figure 23E). Taking together, these results show that both a rapid, local increase in the concentration of ROCK1 mutC$^{PH}$ at the plasma membrane, as well as a long-term, global increase of this mutant in the cytosol by simple over-expression,

lead to increased Myosin activity, suggesting that the interaction of Rho with the PHC1 domain exerts an inhibitory impact on its kinase activity.

A more detailed analysis of the kinetics of Myosin recruitment after ROCK1 perturbations indicated that there is no discernible difference in Myosin activation between ROCK1 and ROCK1 mut$C^{PH}$ during the early phase of recruitment (Figure 23F). In contrast, the difference induced by the mutations is only seen at later, subsequent timepoints, several minutes after the initiation of the perturbation (Figure 23G). Thus, it appears that the inhibitory effect of Rho bound to the PHC1 domain on Myosin activation manifests itself only after a significant time delay.

Taken together, these results show that the PHC1 tandem domain is indispensable for the transduction of Rho signals for Myosin II activation in cells. Additionally, the interaction of the PHC1 tandem domain with active Rho modulates this transduction, exhibiting an inhibitory effect on Myosin activation by ROCK that is either considerably slower, or has a temporal delay.

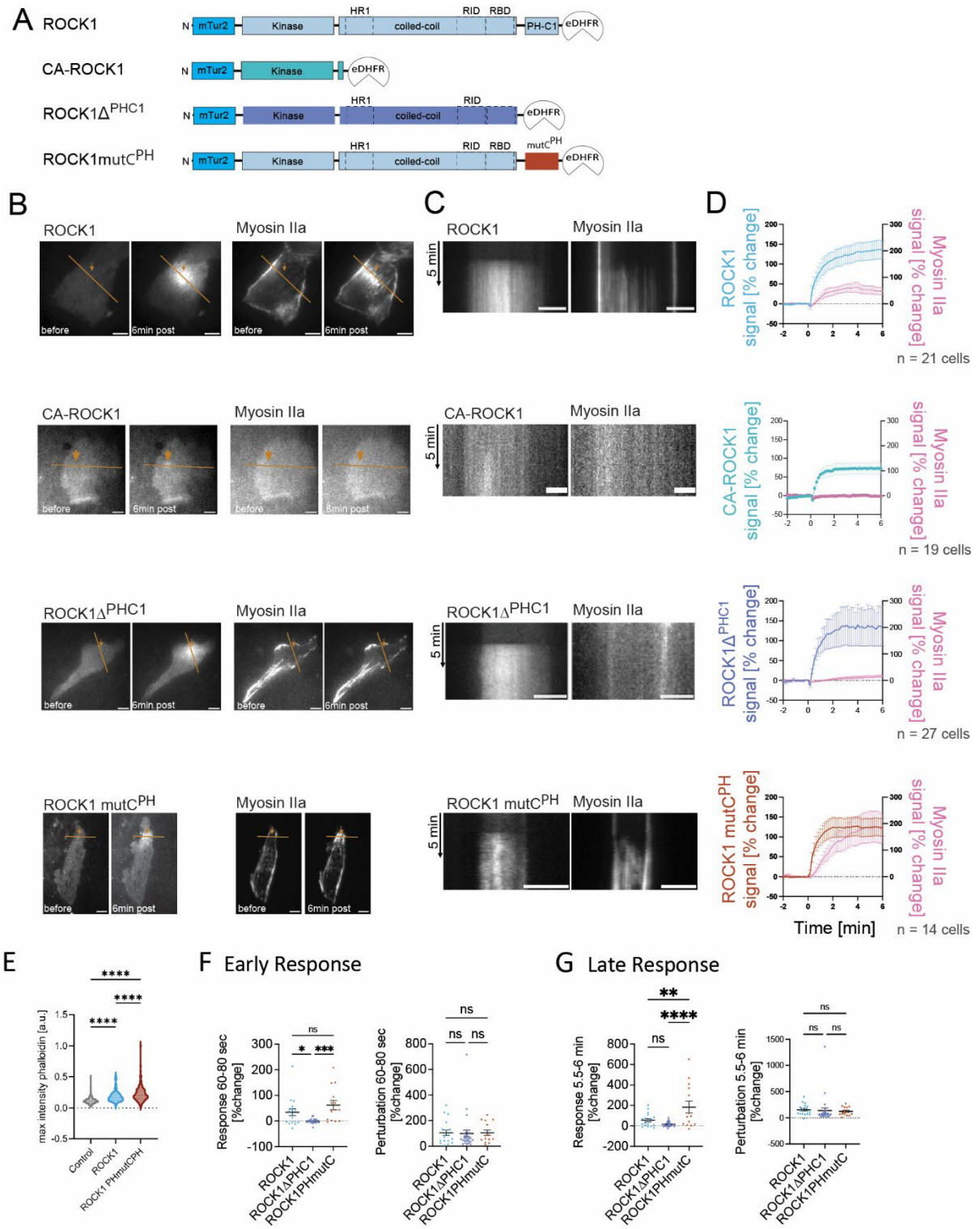


*Figure 23: The PHC1 tandem domain of ROCK1 is essential for its ability to activate Myosin II. (A) Schematic representation of ROCK1 constructs for enforced plasma membrane targeting (C1: phorbol ester/diacylglycerol binding domain, PH: Pleckstrin homology domain, RBD: Rho-binding domain, RID: Rho-interacting domain, HR1: homology region 1, eDHFR: E. coli dihydrofolate reductase, mTur2: mTurquoise2). B. Representative TIRF images of cells co-expressing mTurquoise2-ROCK1 (top left), -CA-ROCK1 (middle1 left), -ROCK1ΔPHC1 (middle2 left), or -ROCK1 mutC$^{PH}$ (bottom left) perturbation constructs, and the mCherry-non-muscle Myosin IIa heavy chain readout construct (right). Images either correspond to a timepoint before perturbation, or six minutes after the initiation of the light-induced perturbation. Orange arrowheads mark the photo-*

*dimerizer uncaging position. (C) Kymographs corresponding to lines in B. (D) Kinetics of the mean fluorescence signals of all cells measured at the perturbation spot (indicated by orange arrows in B). (E) Maximal phalloidin intensity measurement in fixed cells treated with either ROCK1 (blue), ROCK1 mut$C^{PH}$ (red), or the empty parental mCherry construct as control condition (gray). (F-G) Quantitative analysis of the mean response (left) and mean perturbation intensity (right) either 60–80 s (F) or 5.5–6 min (G) after the induction of the perturbation. Panels B-D middle1 are identical to panels B-D in Figure 11. 3 independent experiments were performed. * p < 0.05, ** p < 0.01, *** p < 0.001, **** p < 0.0001, Ordinary one-way ANOVA. Scale bar = 10 µm, 0.26 µm/pixel. Figure adapted from Gierse et al. (2025b).*

### 2.2.6 Alphafold predicts a kink in the ROCK1 coiled-coil that enables simultaneous binding of 3 Rho molecules at the plasma membrane

The results described above reveal several layers of control that can act on ROCK1, including a novel Rho binding site in the PHC1 domain. This newly identified Rho binding domain plays multiple roles, both in the recruitment of ROCK1 to active Rho at the plasma membrane, and in the transduction of Rho activity to activate Myosin. To rationalize, how these new findings might be related to the "Molecular Ruler" (Truebestein et al., 2015) model, in which ROCK1 is proposed to always exist in a fully extended conformation, additional investigations into the ROCK1 structure were performed in collaboration with Ingrid Vetter of the MPI Dortmund.

Strikingly, based on Alphafold2 predictions and well-known repetitive sequence motifs, the coiled-coil domain might form a kink directly C-terminal to the RBD (Figure 24A-B). This kink would allow for flexibility in the angle of the downstream and upstream coiled-coil structures, what enables a conformation in which the upstream coiled-coil can bind one plasma membrane-associated Rho molecule via the RBD in addition to one Rho molecule bound to each PHC1 tandem domain in the ROCK1 dimer (Figure 25A-C). The resulting model is illustrated as a ribbon representation or a representation of the electrostatic surface in Figure 25A-C.

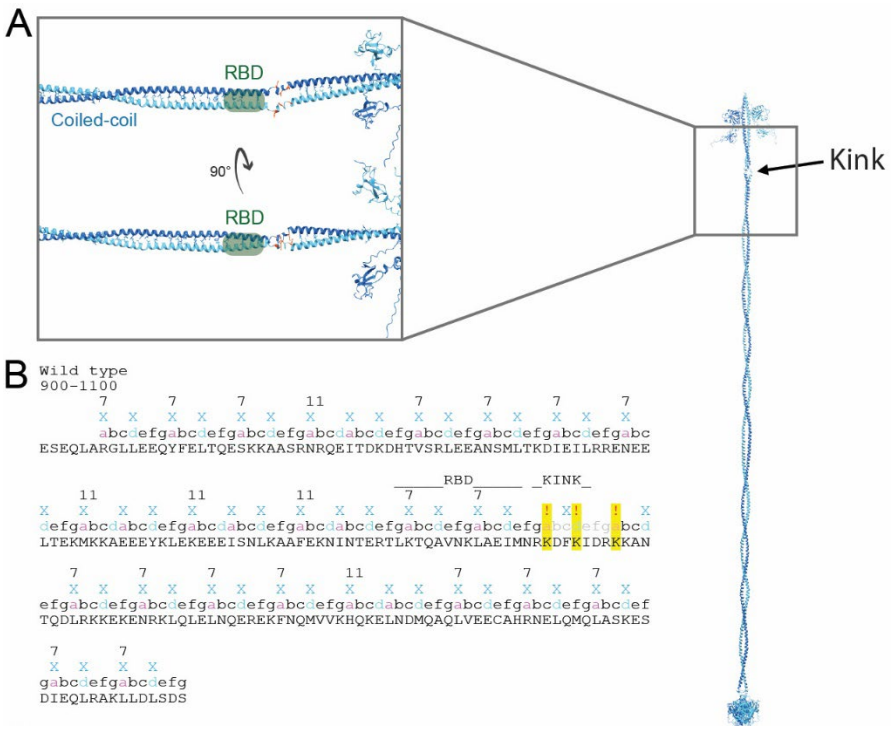


*Figure 24: A predicted kink in the coiled-coil domain of ROCK1 enables an extended conformation at the plasma membrane in complex with multiple active Rho molecules. (A) Structural model of full-length ROCK1 based on Alphafold2 predictions, with a magnified view of a region containing the RBD (Rho binding domain) and the predicted kink in the coiled-coil domain. The kink can be attributed to disrupting elements within the amino sequence motif of the repetitive coiled-coil. (B) The amino acid sequence of ROCK1 of the coiled coil and kink regions corresponding to amino acids 900-1100. The amino acids are indicated by "X" in positions where they point toward the core of the coiled-coil in the Alphafold2 prediction. It is noteworthy that the predominant nature of these amino acids is hydrophobic. The sequence 'abcdefg' corresponds to a single canonical coiled-coil heptad repeat, while 'abcdabcdefg' corresponds to a single non-canonical hendecad repeat. The numerical values of 7 and 11, respectively, indicate the start of each heptad or hendecad repeat. Positions inside the kink regions that are highlighted in yellow and accompanied by an exclamation mark ('!') highlight amino acids that, based on the configuration of coiled-coil heptad repeats, would be expected to be hydrophobic. However, the Alphafold2 prediction indicates that these amino acids are hydrophilic and oriented away from the coiled-coil core. Figure adapted from Gierse et al. (2025b).*

Strikingly, a cluster of positive charges at the kink region of the coiled-coil could stabilize the plasma membrane association of the RBD domain in complex with active Rho and thereby further stabilize a perpendicular orientation of the coiled-coil domain downstream of the RBD (Figure 25A-C). With 3 Rho molecules bound to ROCK1 as shown in Figure 25, the orientation of the coiled-coil perpendicular to the plasma membrane could be stabilized so that the molecule cannot pivot back and forth. This would stabilize the extended conformation of ROCK1 and thereby effectively bridge the distance between plasma membrane bound Rho and Myosin at a more distant position within the dense cell cortex.

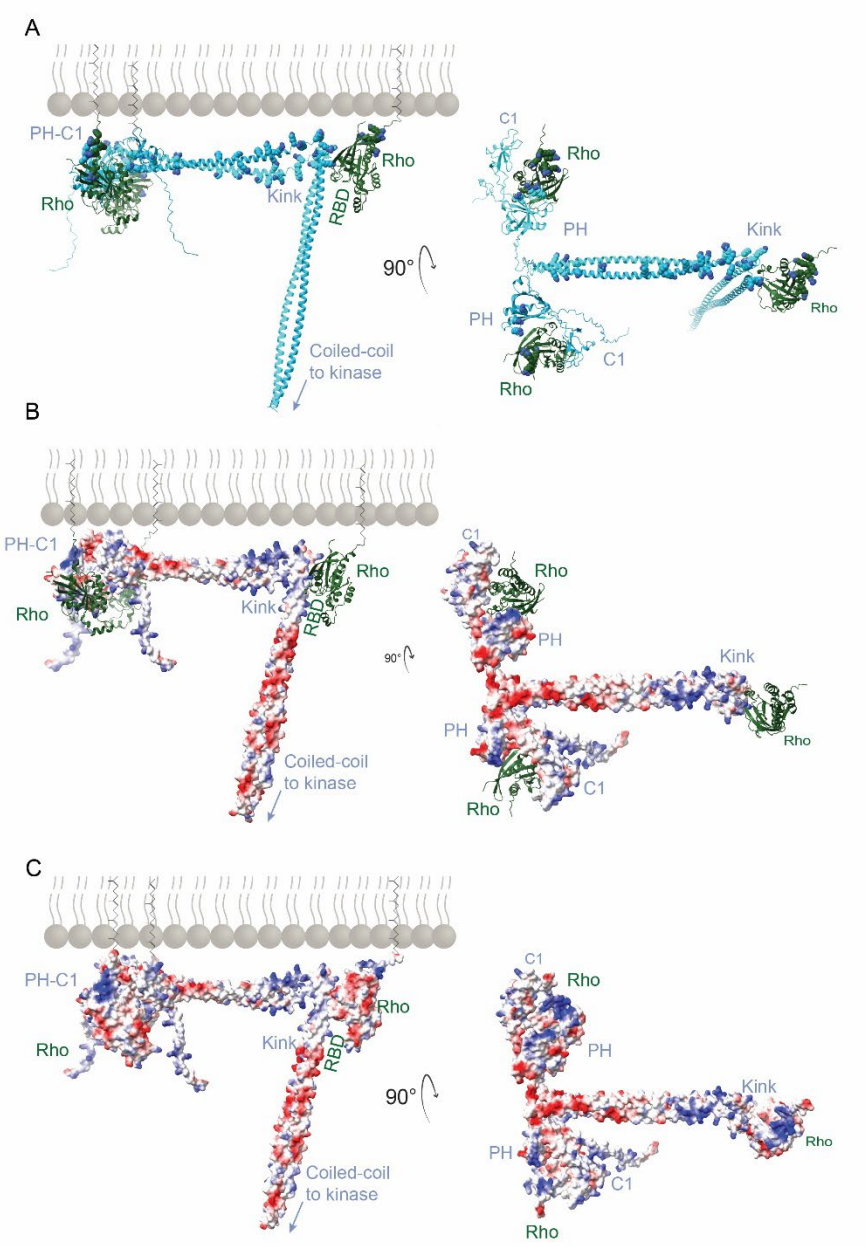


*Figure 25: Structural model of the ROCK1 dimer bound to 3 RhoA-GTP molecules. (A) Left: The ribbon representation of the ROCK1 dimer is shown together with the RhoA molecules. Right: A rotation by 90° showss the full plasma membrane interaction surface and points out the high number of positive charges (blue) in this region (B) Left: In the predicted plasma membrane interaction surface, a cluster of positively charged amino is revealed in the electrostatic surface of ROCK1. Rotating the protein by 90° reveals the full potential plasma membrane interaction surface and highlights the high number of positive charges in this region (left). RhoA molecules depicted in ribbon representation. (C) Left: The ROCK1 dimers electrostatic surface is shown together with the electrostatic surface of bound RhoA molecules. Right: Top view of the structure shown on the left. Both electrostatic surfaces together show that the membrane bound fraction of this model is highly positive. The plasma membrane is indicated in grey and the lipid anchors of all Rho molecules point into the plasma membrane. Figure adapted from Gierse et al. (2025b). Predictions and modelling carried out by Ingrid R. Vetter, MPI Dortmund.*

## 2.3 Crosstalk between Rho GTPases in the spatio-temporal control of the cell contraction signal network

In addition to the well-established causal link, in which ROCK is activated by RhoA activity, additional mechanisms were described that link these two signaling molecules. In the context of feedback regulation of the cell contraction signal network, the functional interaction of ROCK1 with another member of the Rho GTPase family, called Rnd3 (previously referred to as RhoE) was investigated.

### 2.3.1 Mutually exclusive activity patterns of RhoA and Rnd3 in the cell cortex

As described in the introduction, Rnd3 is an unconventional member of the Rho GTPase family, as it is constitutively bound to GTP and its G domain is thus always in the conformation that corresponds to the active, GTP-bound state. Consequently, Rnd3 is not regulated by the canonical mechanism that involves GEFs and GAPs. Functionally, Rnd3 is best known for its role as a RhoA inhibitor. In particular, over-expression of Rnd3 reduces ROCK1 induced stress fiber (SF) formation, decreases Myosin activation and consequently reduces actomyosin contractility (Riento et al., 2003; Riento and Ridley, 2006). This inhibitory effect is mediated by the recruitment of the Rho inhibiting p190RhoGAP by Rnd3 (Dovas and Couchman, 2005; Riou et al., 2010). Conversely, this function of Rnd3 can be inhibited by phosphorylation via ROCK (Riento et al., 2003), resulting in binding of the protein 14-3-3 and their translocation from the plasma membrane to the cytosol (Riento et al., 2003; Komander et al., 2008; Riou et al., 2010; Riou et al., 2013). Together, these two causal links constitute a positive feedback loop via mutual inhibition, which has the potential to act as a toggle switch (see also Figure 1C). Thus, this regulatory link has the potential to significantly influence the dynamics of the pulsatory cell contraction signal network.

To investigate, if the activity of Rnd3 is associated with cell contraction pulses, fluorescently labelled Rnd3 and a Rhotekin-based Rho activity sensor were co-expressed in U2OS cells (Figure 26C). Strikingly, cell contraction signal network activity pulses exhibited a clear anticorrelation between Rnd3 plasma membrane recruitment and Rho activity (Figure 26C, E), which supports the idea that Rnd3 and Rho mutually inhibit each other in the cell contraction

signaling network. Interestingly, we did not observe a substantial change in signal network dynamics even if Rnd3 was expressed at high levels downstream of the strong CMV promoter, indicating that the effect of Rnd3 on cell contraction signal network dynamics is already saturated at its endogenous expression level (Figure 26D).

To more specifically investigate the inhibitory effect of ROCK1 on Rnd3 in the cell contraction signal network, we introduced point mutations in the Rnd3 binding site of ROCK1 (S288R, N292D) (Figure 26A). According to previous work (Komander et al., 2008), these mutations disrupt the Rnd3:ROCK1 interaction and prevent the phosphorylation of Rnd3 by ROCK1. Notably, GEF-H1/Rho dynamics in cells that were transfected with the Rnd3 binding deficient ROCK1 (S288R, N292D) mutant were much higher compared to cells transfected with ROCK1 wild type (Figure 26E-H). Thus, in comparison to the wild-type ROCK1 full-length construct, which substantially inhibited cell contraction dynamics, a comparable level of ROCK1 (S288R, N292D) expression did not show this effect. This suggests that the inhibition of cell contraction dynamics by ROCK1 wildtype is – at least partly – dependent on its interaction with Rnd3.

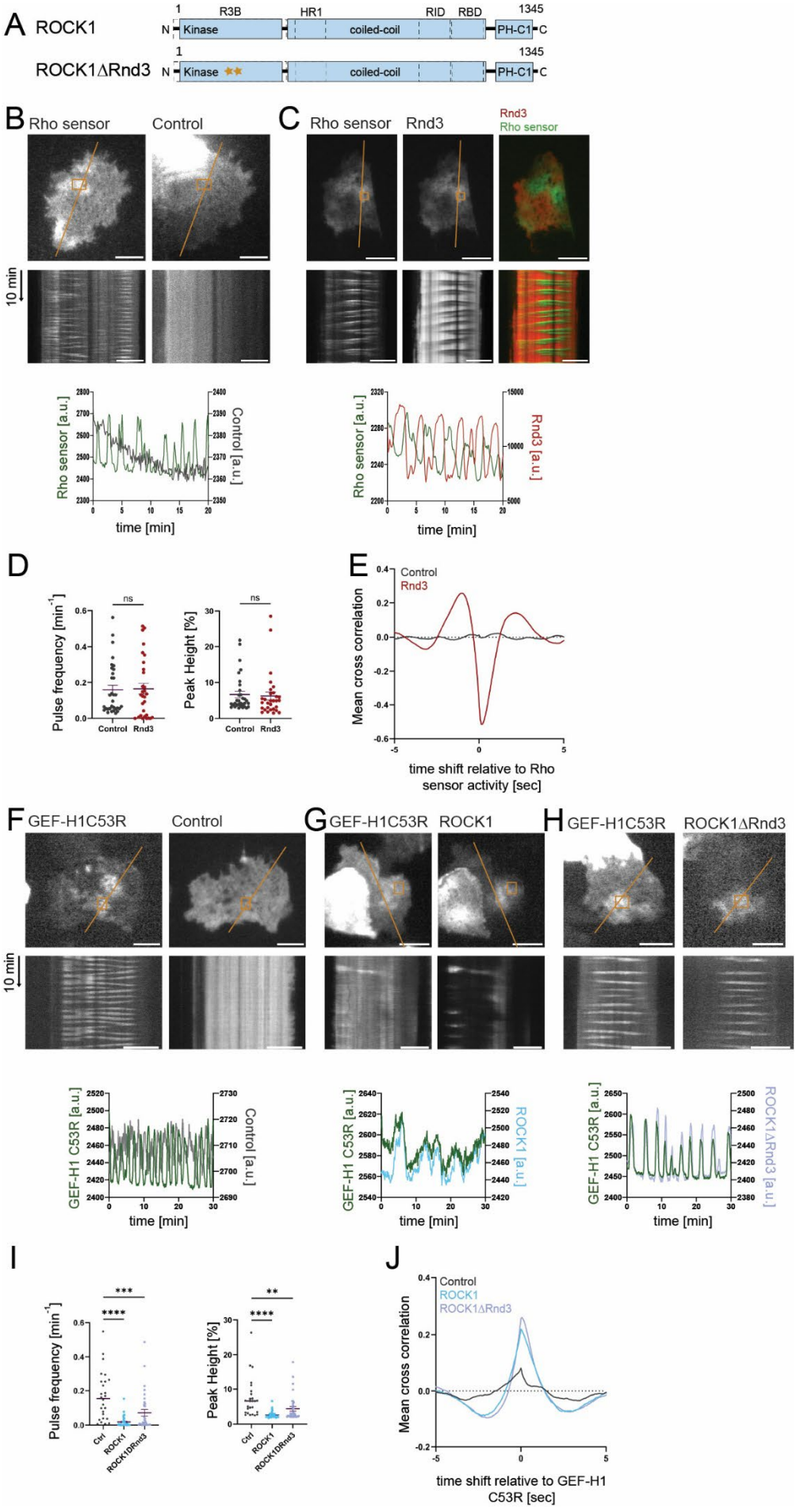
A
ROCK1
ROCK1ΔRnd3
N
C
1
1345
R3B
HR1
RID
RBD
Kinase
coiled-coil
PH-C1
B
Rho sensor
Control
C
Rho sensor
Rnd3
Rnd3
Rho sensor
10 min
Rho sensor [a.u.]
Control [a.u.]
Rnd3 [a.u.]
time [min]
D
Pulse frequency [min-1]
Peak Height [%]
ns
Control
Rnd3
E
Control
Rnd3
Mean cross correlation
time shift relative to Rho sensor activity [sec]
F
GEF-H1C53R
Control
G
GEF-H1C53R
ROCK1
H
GEF-H1C53R
ROCK1ΔRnd3
GEF-H1 C53R [a.u.]
Control [a.u.]
ROCK1 [a.u.]
ROCK1ΔRnd3 [a.u.]
I
Pulse frequency [min-1]
Peak Height [%]
Ctrl
ROCK1
ROCK1DRnd3
J
Control
ROCK1
ROCK1ΔRnd3
Mean cross correlation
time shift relative to GEF-H1 C53R [sec]

Figure 26: *Inhibiting the ROCK1:Rnd3 interaction partially rescues the effect of ROCK1 over-expression on cell contraction signal network dynamics. (A) Schematic representation of ROCK1 wild type and Rnd3 binding deficient mutant ROCK1ΔRnd3 (Ser288Arg & Asn292Asp* (Komander et al., 2008)*). (B-C) Representative TIRF images (top), corresponding kymographs (middle) and intensity profiles (bottom) of Rho activity sensor dynamics in control (B) and Rnd3 (C) expressing cells. (D) Quantitative analysis of plasma membrane recruitment dynamics with and without Rnd3 over-expression. (E) Temporal cross-correlation functions for Rnd3 plasma membrane localization and Rho activity signals. (F-H) Representative TIRF images (top), corresponding kymographs (middle) and intensity profiles (bottom) of Rho activity sensor dynamics in control (F), ROCK1 (G) and ROCK1ΔRnd3 (H) expressing cells. (I) Quantitative analysis of plasma membrane recruitment dynamics of GEF-H1 C53R in the presence of the indicated ROCK1 constructs. (J) Temporal cross-correlation functions for ROCK1 and GEF-H1 C53R plasma membrane localization signals. Error bars represent standard error of the mean from 3 independent experiments each. **: p < 0.01, ***: p < 0.001, ****: p < 0.0001, ns: non-significant, unpaired t-test (D) and Dunnett's multiple comparison test (I), scale bar = 10 µm, 0.26 µm/pixel. Cells in B-D were treated with 30 µM nocodazole.*

This observation raised the question whether the even stronger, inhibitory effect of CA-ROCK1 on cell contraction dynamics, shown in Figure 9D, was also dependent on Rnd3 or only an effect of constitutive Myosin II activation as suggested in Section 2.1. To test this, a Rnd3 binding deficient CA-ROCK1 construct was generated [3] and its effect on GEF-H1 stimulated cell contraction dynamics was measured. As shown in Figure 27, the interaction of ROCK1 with Rnd3 does not have a substantial impact on the effect of CA-ROCK1 on signal network dynamics. Thus, the ROCK1:Rnd3 interaction only appears to have an effect in the presence of the normal mechanisms that regulate ROCK1 activity via its C-terminal domain.

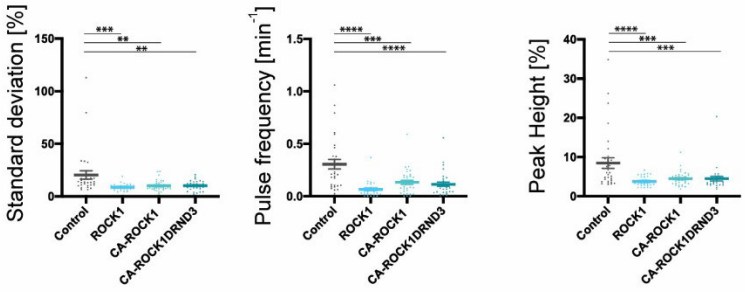


*Figure 27: The inhibitory effect of CA-ROCK1 on cell contraction signal network dynamics is not dependent on its interaction with Rnd3. The quantitative analysis of plasma membrane recruitment dynamics of GEF-H1 C53R in the presence of the indicated ROCK1 constructs is shown. An empty parental mCherry construct was used as a control. The signal network dynamics were stimulated by adding 30 µM of nocodazole (n=3 independent experiments). **: p < 0.01, ***: p < 0.001, ****: p < 0.0001, Ordinary one-way ANOVA.*

[3] These investigations were performed under my supervision by Bachelor student Jennifer Hanemann (Thesis year 2023)

# 3 Discussion

## 3.1 Myosin and not Actin acts as the negative feedback mediator in the cell contraction signaling network

In this work, several lines of evidence support the idea that Myosin and not Actin mediates negative feedback regulation in the cell contraction signaling network. First, this evidence is based on the combination of simulations and experiments that confirm that either an inhibition or a constitutive activation of the Rho effector kinase ROCK leads to an inhibition of dynamics in the cell contraction signal network. Specifically, in simulations, a gradual inhibition of ROCK1 by a stepwise reduction of the link between Rho activity and Myosin activation results in a corresponding gradual reduction of Rho activity dynamics (Figure 8D-E). Similarly, in experiments, a relatively broad concentration range of the pharmacological ROCK1 inhibitor Y27632 reduced analogous measures of Rho activity dynamics (Graessl et al., 2017). Furthermore, even a very small amount of constitutive, Rho-independent Myosin activation abolished Rho dynamics in simulations, and analogous experiments showed that the constitutively active CA-ROCK1 construct strongly suppressed these dynamics (Figure 9C-D). This shows that ROCK1 and/or its downstream effector Myosin are critical to generate Rho activity dynamics in adherent, mammalian cells. In other systems, such as *C. elegans* embryos, knockdown of Myosin-II only suppressed Myosin dynamics without affecting Rho activity dynamics (Nishikawa et al., 2017), showing that cell contraction pulses in adherent, mammalian cells and in C. elegans embryos operate via distinct molecular mechanisms.

Interestingly, in some cells that express CA-ROCK1, Rho activity dynamics were not eliminated everywhere. Instead, activity dynamics were specifically inhibited near the center of the cell attachment area and some residual signal dynamics were retained near the cell periphery (Figure 10E-G). This effect can be explained by the highly local accumulation of Myosin II next to the nucleus, which was accompanied by a depletion of Myosin II away from the cell periphery by a strong centripetal flow. Thus, based on the logic of Myosin-II acting as a Rho inhibitor, Rho activity dynamics would only be possible in the cell periphery. This feature of Rho independent Myosin activation might be relevant for some striking differences in the morphodynamics of distinct cell types.

Cell migration was shown previously to be affected by spatial organization of cell contraction. Peripheral contraction was shown to have a positive effect on migration speed and directionality, and central contraction a negative effect (Totsukawa et al., 2004). In that study, this spatially differential control of cell contraction, central vs peripheral, was linked to distinct upstream kinases, ROCK vs MLCK, respectively (Totsukawa et al., 2004). The current work in this thesis suggests that the ROCK kinase alone might be sufficient to differentially affect Myosin activation. As discussed in the previous paragraph, depending on how ROCK is activated, it can induce central or peripheral Myosin phosphorylation. Rho-dependent ROCK activation stimulates both central and peripheral Myosin activation while Rho-independent activation stimulates predominantly central Myosin activation. The balance of Rho-dependent and Rho-independent ROCK activating might thus play a role in tuning spatial cell contraction and thereby migration speed and directionality.

ROCK is best known to be activated by Rho, but some studies also suggested alternative activation mechanisms. Caspase-triggered activation is thought to lead to constitutive activation of ROCK (Coleman et al., 2001; Gabet et al., 2011; Özdemir et al., 2021). Indeed, in Coleman et al. (2001), accumulation of F-actin structures close to the nucleus, that were similar to those observed in this thesis, were observed before apoptosis. Notably, recent research demonstrates that caspases do not only act in apoptosis, but do also have unconventional roles in cell differentiation, proliferation and invasion (Abdelghany et al., 2024). For example, the cleavage of the C-terminal domain of ROCK1 is also involved in cell differentiation (Gabet et al., 2011) and interestingly, it has been shown that caspase-3 is involved in promoting migration and invasion in melanoma cells (Liu et al., 2013). Therefore, a less pronounced, small level of constitutively active ROCK could also play a role in other cellular processes since it is not only present in apoptotic cells. For instance, the caspase activated ROCK could affect the balance between peripheral and central contraction during cell migration.

The results obtained in this thesis clearly support the idea, that Myosin II acts either directly or indirectly as an inhibitor of Rho activity. However, on the one hand, cells could adapt to the long-term expression of constitutively active CA-ROCK1, and on the other hand, the pharmacological treatments could have toxic side effects and thus might lack specificity. To address these problems, rapid ROCK1 perturbations were performed in U2OS cells (Figure 13)

using light-induced recruitment of full-length ROCK1 to the plasma membrane. These perturbations were very fast and resulted in a strong Myosin II recruitment response within a few minutes. The recruited Myosin II was characterized by a strong flow indicating efficient stimulation of Myosin motor activity (movie Figure4G-H in Gierse et al. (2025a)). Furthermore, these perturbations were very specific and not expected to have toxic side-effects, as they were based on a positive perturbation, i.e. stimulation of activity, rather than a negative perturbation such as inhibition via pharmacological substances. The strong, rapid activation of Myosin that was stimulated by the plasma membrane recruitment of ROCK1 lead to a significant reduction both of Rho activity dynamics and of Rho baseline activity. Measurements of the actin response to rapid ROCK1 perturbations revealed that this actomyosin component is not increased but rather reduced upon plasma membrane recruitment of ROCK1. Taking together, this shows that the inhibition of Rho activity downstream of ROCK1 can only be explained by a Myosin-mediated and not by an actin-mediated mechanism.

As ROCK1 is a well-established activator of the actin nucleating formin FHOD1, it was initially unexpected that actin abundance at the plasma membrane was decreased upon ROCK1 activation (Gasteier et al., 2003). Formins are well-known for their ability to both nucleate actin filaments, and for staying attached to the newly nucleated barbed end, where they can subsequently regulate filament elongation. Depending on the formin family member, these molecules act either as slow, intermediate or fast elongators (Oosterheert et al., 2024). Specifically, FHOD1 is known to be a very slow elongator (Schönichen et al., 2013), in particular in comparison to other formins, such as mDia1 (Romero et al., 2004; Antoku et al., 2023). mDia1 and FHOD1 also differ in the way they are activated: mDia1 is directly activated by Rho and FHOD1 is activated by the Rho effector ROCK1. Thus, plasma membrane recruitment of ROCK1 would be expected to only activate FHOD1 and not mDia1. This could therefore lead to a competition between these molecules to bind to actin filament barbed ends, resulting in a reduction of the fast-elongating formins like mDia1 that would get replaced by slow-elongating formins like FHOD1. In addition, FHOD1 also functions as a highly efficient actin filament crosslinker (Schönichen et al., 2013; Antoku et al., 2023). This might further contribute to the loss of actin upon ROCK1 activation, as the action of Myosin on highly crosslinked actin filaments results in their breakage and destabilization (Murrell and Gardel,

2012; Vogel et al., 2013; Vemula et al., 2021). Furthermore, isoform specific effects of ROCK1 and ROCK2 on F-actin were described previously (Newell-Litwa et al., 2015). ROCK2 was shown to stabilize the actin cytoskeleton via an inhibitory phosphorylation of cofilin, while ROCK1 does not have this effect (Newell-Litwa et al., 2015). Thus, the lack of actin stabilization downstream of ROCK1 might also contribute to the observation that forced plasma membrane recruitment of this molecule does not lead to an actin increase at the plasma membrane. It would therefore be interesting for future studies to perform analogous experiments with ROCK2 to investigate its effect on actin.

Taken together, previous studies and results presented in this thesis clearly show that Myosin acts both downstream and upstream of Rho activity in adherent, mammalian cells. Myosin is clearly activated downstream of Rho, however, this activation occurs with a significant temporal delay. Once activated, Myosin also acts upstream and inhibits Rho activity. Together, this closes a negative feedback loop that regulates cell contraction signal network dynamics. The exact mechanism of how Myosin inhibits Rho activity is still unclear and requires further research. One potential mechanism could be mediated by a direct interaction of Myosin with the DH domain of GEF-H1 (Lee et al., 2010), which was previously suggested to compete with the ability of this domain to activate Rho. This would disrupt the positive feedback loop between GEF-H1 and Rho, eventually leading to the inactivation of Rho activity. Another potential explanation is the direct association of RhoGAPs with Myosin. However, the identity of such molecules is unclear in the U2OS cell system.

Our observation that Myosin II functions as a negative feedback mediator is particularly noteworthy, as it demonstrates that adherent mammalian cells employ a distinct molecular mechanism to induce cell contraction pulses compared to Starfish or *Xenopus* oocytes, or *C. elegans* embryos. While these systems generate activity patterns with notable similarities, including oscillations, pulses, and propagating waves, it is important to note that several specific features exhibit significant distinctions. For instance, adherent mammalian cells employ Lbc-type RhoGEFs, such as LARG or GEF-H1, as positive feedback mediators. In contrast, oocytes depend on the non-Lbc type GEF Ect2, which differs in its activation mechanism, and how it can amplify Rho via positive feedback. In addition, the duration of signal network activity pulses is substantially prolonged for the Myosin-dependent mechanism in adherent mammalian cells (approximately 4 minutes (Kamps et al., 2020)) , in

comparison to the Myosin-independent mechanisms in other systems (C. elegans embryos: period approximately 0.5 minutes (Nishikawa et al., 2017); Xenopus oocytes: period approximately 1.5 minutes (Michaud et al., 2022); starfish oocytes: period approximately 1.2 minutes (Bement et al., 2015)). Interestingly, the enforcement of an alternative, actin-dependent negative feedback mechanism in U2OS cells by the expression of the F-actin-associated RhoGAP Myo9b results in significantly shorter signal network activity pulses (period approximately 0.5 min (Graessl et al., 2017)). This is analogous to the pulse periods observed in *C. elegans*, Xenopus, and starfish. These discrepancies in pulse frequency for actin- or Myosin-dependent negative feedback mechanisms are presumably attributable to the varying recruitment kinetics of actin vs Myosin II downstream of Rho activity, which exhibit substantial disparities in adherent mammalian cells (Myosin II: approximately 40s; Actin: approximately 11s (Graessl et al., 2017)).

## 3.2 Mutual inhibition between Rho and Rnd3 reduces cell contraction signal network dynamics

The presented investigations into negative feedback regulation of cell contraction revealed unexpected differences between the phenotypes induced by over-expression of ROCK1 full-length compared to constitutively active CA-ROCK1. Over-expression of either of these proteins is expected to increase the ROCK1 activity, and based on the SDE simulations, this is expected to reduce cell contraction signal network dynamics. Furthermore, based on previous studies, CA-ROCK1 is expected to have a higher activity compared to full-length ROCK1 (Ishizaki et al., 1997), however, it was less effective in inhibiting cell contraction signal network dynamics. This was very surprising, in particular, as our observations support the idea that on long timescales, CA-ROCK1 has higher activity vs full-length ROCK1 (compare Figure 9F to Figure 23E). These distinct effects could be due to additional interactions of ROCK1 with the unconventional Rho GTPase Rnd3 as summarized in Figure 28.

Figure 28A illustrates the network topology that was originally proposed by Graessl et al. (2017) and Kamps et al. (2020), and which is now well-supported by the clear demonstration that Myosin mediates negative feedback. This signaling network is sufficient to explain the basic oscillatory and pulsatile system dynamics that were already observed in previous studies. In the context of this thesis, CA-ROCK1 was integrated as a Rho-independent Myosin

II activator into this scheme (Figure 28B). The simple expectation that a stronger activation of Myosin by CA-ROCK1 should strengthen inhibitory signaling and weaken signal network dynamics was confirmed by corresponding SDE simulations (Figure 9). More precisely, it was concluded that the constitutive over-activation of Myosin II saturates the negative feedback, thereby inhibiting signaling dynamics. It was surprising that over-expression of wildtype ROCK1 has an even stronger effect on dynamics (Figure 26), while it has a weaker effect on Myosin. Results in this thesis suggest that this can be explained by the functional interaction between ROCK1 and Rnd3.

First, overexpressing the Rnd3-binding deficient ROCK1 construct, ROCK1ΔRnd3, does elicit less inhibitory effect compared to over-expression of ROCK1 wild type (Figure 28C), showing that Rnd3 is essential for the inhibitory action of full-length ROCK1. This Rnd3-binding deficient ROCK1 construct is identical to full-length ROCK1, except for its inability to bind, phosphorylate and thereby inhibit Rnd3. Second, this ability of ROCK1 to inhibit Rnd3 is a critical feature of the mutual inhibition between Rho and Rnd3, which leads to bistable dynamics and mutual exclusive activation of either molecule (Figure 26C). Over-expression of wild-type ROCK1 would strengthen the inhibition of Rnd3, thereby changing the balance between Rho and Rnd3 activity (Figure 26D). This would be expected to at least transiently trap the system in the state of high Rho/ROCK and low Rnd3, and thereby inhibit dynamic, oscillatory dynamics (Figure 28D).

In conclusion, the inhibitory effect of ROCK1 full-length over-expression on the cell contraction network pulses in adherend U2OS cells is partly dependent on the activation of Myosin by ROCK1 and the inhibition of Rnd3 by ROCK1. The latter demonstrates that the Rho activity within the cell contraction signaling network is balanced via a toggle-switch network with Rnd3.

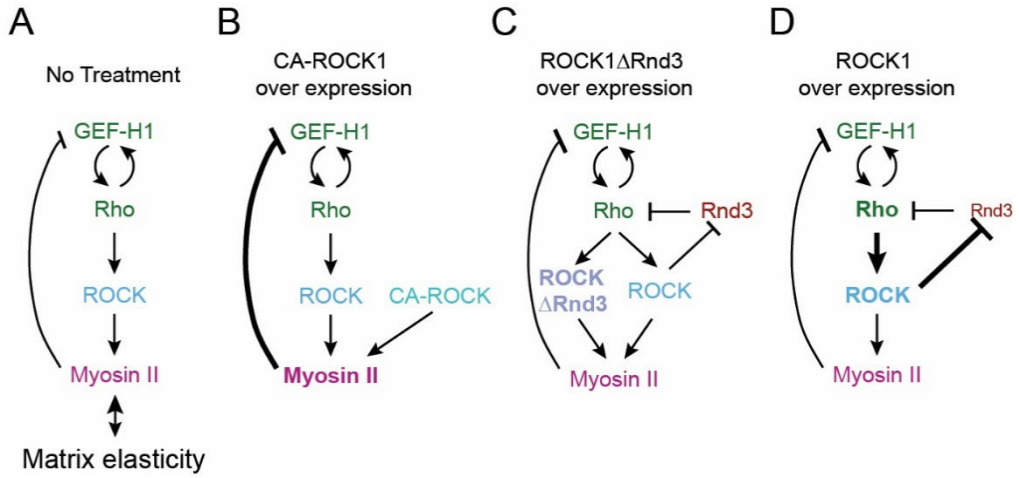


*Figure 28: Schematic representations of the core cell contraction signal network topology and its extension with additional components introduced in this thesis. (A) The core cell contraction signaling network topology as proposed by Graessl et al. (2017), with the addition of full-length, wild-type ROCK1 as a link between Rho and Myosin activities. (B) Proposed changes in signaling upon activation of Myosin II by CA-ROCK1 (non-feedback Myosin II activation). The over-activation of Myosin II leads to increased inhibition of GEF-H1 by Myosin, which is expected to inhibit network dynamics. (C-D) Proposed changes in signaling upon over-expression of a Rnd3 binding deficient mutant (C) or wild-type ROCK1 (D). Mutual inhibition between Rho and Rnd3 is expected to be strengthened by wild-type ROCK1, which is expected to reduce signal network dynamics (D), by locking the system in a high Rho, low Rnd3 state. In contrast, a Rnd3 binding deficient ROCK1 mutant cannot participate in mutual inhibition and therefore has a weaker effect. Apparently, by itself, the relatively weak ability of wild-type ROCK1 to activate Myosin does not have a strong effect on signal network dynamics in the absence of mutual inhibition between Rho and Rnd3.*

## 3.3 Rapid and robust perturbation of signal network activities at the plasma membrane via Cell-Attachment area Molecular Activity Painting (CA-MAP)

In addition to these insights into the biology of cell contraction signaling, the development of the new Molecular Activity Painting variant that acts on the entire cell attachment area might also be useful for other future studies. In previous work, Molecular Activity Painting was used together with immobilized artificial receptors to recruit a signaling molecule of interest into a stable line or point-like perturbation pattern at the plasma membrane (Chen et al., 2017; Kamps et al., 2020; Kowalczyk et al., 2022). Alternatively, a simplified variant that is based on diffusible membrane anchors, or non-immobilized artificial receptors was used to introduce transient, point-like perturbations at the plasma membrane (Chen et al., 2017; Kamps et al., 2020; Kowalczyk et al., 2022). Here, another simplified variant based on non-immobilized artificial receptors was developed, in which the entire cell attachment area was illuminated

using the evanescent wave of a TIRF microscope, to recruit a signaling molecule of interest into this much larger area of the cell. This enables very fast and very efficient recruitment and a corresponding, very robust cell response. Thus, this variant will be very useful for other research questions, in which spatial precision is less important than robust and efficient perturbation strength.

Furthermore, inducing perturbations in the entire cell attachment area has several advantages compared to alternative methods, such as the recruitment of proteins to the entire plasma membrane via chemically-induced dimerization (Spencer et al., 1993; Liu et al., 2014; Nanda et al., 2023). By limiting the recruitment to the cell attachment area, only those areas, for which the response can be easily monitored via TIRF microscopy are targeted. Considering the resulting functional response, this can increase the local effect and reduce the overall effect on the whole cell. Consequently, the potential stress experienced by the cell can also be reduced. Furthermore, this novel variant offers a significant practical advantage over chemically-induced dimerization: It is not necessary to add the small molecule dimerizer during measurements on the microscope stage. Instead, the photochemical dimerizer is incubated prior to measurements, and then selectively activated only within the measured field of view. This enables multiple, independent, sequential measurements of perturbation-response kinetics in different fields of view in a single sample.

Here, this new method was used to robustly activate Myosin II downstream of ROCK1. Usually, Myosin is activated together with actin polymerization to generate typical non-muscle actomyosin structures. This can indeed be seen in the studies from Graessl et al. (2017), in which Myosin II and actin were found to be co-recruited to spontaneous Rho activity pulses. Rho is indeed well-known to stimulate actin polymerization via formins such as mDia1, in parallel to Myosin activation via ROCK. As discussed in more detail in section 3.1, the rapid, light-induced recruitment of ROCK1 to the plasma membrane activates Myosin highly selectively without co-stimulating actin polymerization. In fact, the observation that actin is even reduced after ROCK1 activation offers a unique tool to study the function of non-muscle Myosin II independent of total actin amounts and thus enables functional dissection of Myosin vs actin dependent processes within cells.

## 3.4 Multiple binding sites contribute to the interaction between ROCK1 and active Rho

The investigations of negative feedback regulation of cell contraction revealed significant novel insights into the mechanism by which ROCK transduces signals from Rho to activate Myosin.

First, the substantial local enrichment of ROCK at cell contraction pulses and the robust local stimulation of Myosin after local enrichment of ROCK1 at the plasma membrane unequivocally demonstrate that the translocation of this molecule to the plasma membrane constitutes a pivotal prerequisite for the local control of cell contraction. In essence, to transduce Rho activity to activate Myosin, ROCK1 first needs to be recruited to active Rho at the plasma membrane.

Previous studies revealed several sequences in ROCK1 that can bind to active Rho. This includes the HR1 (Homology Region 1), RID (Rho-interacting domain), and RBD (Rho-binding domain). While the HR1 and RID regions were only identified via sequence similarity searches and only reported in a single study (Blumenstein and Ahmadian, 2004), the RBD region is well-established and was studied in detail both *in vitro* and *in cellulo* (Fujisawa et al., 1996; Dvorsky et al., 2004). Since its initial identification, many studies indicated that the RBD region is a RhoA specific GTPase-binding domain (GBD) that selectively interacts with the active form of RhoA and that it is somehow able to increase the activity of the ROCK kinase domain (Amano et al., 1997). Furthermore, several studies support an important functional role for the RBD region (Ishizaki et al., 1996; Pinner and Sahai, 2008; Munjal et al., 2015; Sidor et al., 2020). In particular, studies of the ROCK ortholog Rok in *Drosophila melanogaster* showed that its RBD participates in plasma membrane recruitment (Munjal et al., 2015, Sidor et al., 2020). Specifically, Rok localization to the plasma membrane of the salivary gland placode was found to be dependent on the RBD (Sidor et al., 2020). Furthermore, in the plasma membrane of vertical junctions during germ band extension, Rok was enriched in a pulsatile manner that correlated with local Rho activity, and this enrichment was partially dependent on the RBD (Munjal et al., 2015).

In contrast to these studies that underlined the importance of the RBD region, Truebestein et al. (2015) have questioned its functional significance. In fact, these authors could not detect

any interaction between RhoA and the ROCK1 or ROCK2 RBDs. Furthermore, Truebestein et al. also were unable to detect binding of full-length ROCK2 to RhoA. It is important to note that the experiments of Truebestein et al. (2015) were not performed *in cellulo* but instead *in vitro* with purified proteins. It is therefore possible that posttranslational modifications in the Rho GBDs or additional proteins or cellular factors are required to enable the interaction between RhoA and ROCK.

In this thesis, a new binding site for active Rho was identified in the C-terminal PHC1 domain (Figure 16). In previous studies, the PHC1 domain was only thought to bind unspecifically to the plasma membrane by a cluster of positively charged amino acids (Wen et al., 2008). In contrast, the present results clearly demonstrate that this binding of the PHC1 tandem domain to the membrane is dependent on Rho activity. Furthermore, in combination with the AlphaFold predictions of the PHC1:Rho complex and AlphaFold-guided mutagenesis, very strong evidence is provided that the mPHC1 domain directly and specifically interacts with active Rho (Figure 16, Figure 17, and Figure 18).

In principle, any of the Rho binding sites on ROCK1, including the PHC1 domain or any of the previously known regions in the coiled-coil, could recruit ROCK1 to Rho activity at the plasma membrane. Detailed analysis based on point mutants provided in this thesis shows that the Rho binding sites in the RBD and in the PHC1 domains contribute most, if not all the recruitment of ROCK to active Rho at the plasma membrane. While introducing four point mutations into the mPHC1 domain ($mutC^{PH}$) or two point mutations into the RBD ($mut^{RBD}$) significantly decreased ROCK1 targeting to pulses of Rho activity (Figure 20), co-recruitment was still clearly detectable. Only the combination of both point mutation sets ($mut^{RBD}mutC^{PH}$) was sufficient to nearly completely abolish recruitment of ROCK1 to pulses of Rho activity (Figure 22).

The residual, very weak plasma membrane recruitment of the combined ROCK1 $mut^{RBD}mutC^{PH}$ mutant could be explained either by the presence of the other two identified Rho GBDs within the coiled-coil domain, by incomplete disruption of the RBD and/or PHC1 domain Rho interactions, or by the heterodimerization of the ROCK1 $mut^{RBD}mutC^{PH}$ mutant with endogenous ROCK1 molecules. In any case, this residual recruitment is very weak. In fact, the standard deviation measurements of the ROCK1 double mutant are only 6% higher than the corresponding measurements of a negative control construct after normalization to

ROCK1 full-length. These observations are also in agreement with studies in Drosophila, which showed that the removal of either the PH domain or of the RBD of Rok decreased the overall membrane accumulation, and that both domains are essential for correct subcellular localization of Rok (Sidor et al., 2020).

The new Rho binding activity of the PHC1 domain can also provide a better understanding of previous studies. As mentioned above, during Drosophila germ band extension, Munjal et al. (2015) observed only a partial loss (approx. 50%) of pulsatile Rok recruitment to the plasma membrane after RBD removal. The authors proposed that the residual pulsatile behavior of Rok could be explained by advective flows powered by Myosin activity. The new findings presented in this thesis offer an alternative explanation: the loss of the RBD only leads to a partial reduction of plasma membrane recruitment, as Rok is still able to bind active Rho via the PHC1 domain. This alternative explanation is not purely based on speculation or hypothetical models, but instead supported by the observations shown in this thesis for mammalian cells, and the conservation of the critical Rho interacting amino acids in the PHC1 domain between human and *Drosophila melanogaster* (Figure 17D).

Taken together, the identification of multiple important Rho binding sites in ROCK fills an important gap in our knowledge about the function of this critical signal molecule. Nevertheless, the controversies between cell biological and biochemical studies suggest that the mechanism of ROCK1 activation is highly complex.

## 3.5 The role of the PHC1 domain and of the RBD region for ROCK1 function

Interestingly, the investigations reported in this thesis show that simply recruiting ROCK1 to the plasma membrane is not sufficient to activate Myosin. This was already previously proposed by Truebestein et al. (2015), who suggested that ROCK is always present in a fully extended conformation at the plasma membrane and that the PHC1 tandem domain binds the plasma membrane. Their so called “Molecular ruler hypothesis” proposes that in this fully extended ROCK, the coiled-coil region acts as a spacer to position the kinase domain approximately 120 nm away from the plasma membrane. In this conformation, the N-terminal kinase domain is capable of accessing the desired Myosin for activation through the cell cortex. However, this novel hypothesis gave rise to the question of how ROCK1 is regulated by

Rho, given that the previously identified GBDs within ROCK's coiled-coil domain are positioned too far away from the membrane for Rho to reach them (Figure 29A).

The novel GBD within the PHC1 domain of ROCK1 has the potential to resolve this issue, as Rho can readily access it. In addition, the "Molecular ruler hypothesis" is also supported by the Myosin response to rapid, light-induced plasma membrane recruitment of ROCK1 constructs with differences in the length of their central coiled-coil domain. ROCK1 full-length recruitment strongly activates Myosin II at the perturbation site. In contrast, the much shorter CA-ROCK, consisting only of the kinase domain and a small region of the coiled-coil domain, was not able to recruit or activate Myosin II at the perturbation site (Figure 23B-D, top and middle1). This finding thus substantiates the hypothesis that the length of ROCK1 is indispensable for the activation of Myosin.

The presence of a Rho binding domain in the PHC1 domain raises the question of which role the additional RBD within the coiled coil region might play. In the fully extended ROCK conformation, this RBD would not be able to reach active Rho in the plasma membrane, however, if the coiled-coil forms a flexible kink C-terminal to the RBD as predicted by AlphaFold2 (Figure 24), the RBD could indeed play an additional role in plasma membrane targeting and positioning of ROCK. This kink allows the otherwise rigid coiled-coil to undergo bending, thereby enabling the RBD region to be close to the plasma membrane. Furthermore, the kink also allows the interaction of ROCK with Rho in its natural, lipid-anchored orientation at the plasma membrane, which would otherwise not be possible for steric reasons (Figure 25).

Vice versa, the presence of the RBD within the coiled coil region raises the question, which role the additional RBD within the PHC1 domain might play. Interestingly, while enforced plasma membrane targeting of ROCK1 wild type induced a strong Myosin response (Figure 23), this effect was completely dependent on the presence of the PHC1 domain (Figure 23). This finding suggests that the PHC1 domain plays a critical role in the process of ROCK1-mediated activation of Myosin II. However, while the domain itself was essential for activating Myosin, its interaction with Rho had the opposite effect. Mutations that prevent Rho binding to mPHC1 paradoxically strengthened Myosin activation. Thus, RhoA binding to mPHC1 appears to inhibit localized kinase activity at the plasma membrane and suggests that the interaction of Rho with the C-terminus of ROCK somehow affects the ability of the very distant

N-terminal kinase to activate Myosin. This was a very surprising observation that could conceivably be explained by one of the following mechanisms:

(a) Via a conformational change at the C-terminus that is induced by Rho binding and transmitted through the coiled-coil domain to modulate the activity of the N-terminal kinase. This behavior has already been observed in dyneins, where sliding of the two helices that originates from a conformational change at one end of a coiled-coil can cause a conformational change at other end of the coiled-coil, resulting in altered affinity to microtubules (Truebestein and Leonard, 2016).

(b) Classical studies of ROCK regulation, suggested an autoinhibitory mechanism, in which the PHC1 domain acts in a dominant-negative fashion by interacting with and inhibiting the N-terminal kinase domain (see section 1.4.1). Based on this model, an interaction of the RBD, of the PHC1 domain, or both with the plasma membrane or Rho was proposed to release this inhibition, freeing the kinase domain and leading to Myosin activation. Notably, in this thesis, no inhibitory effect on cell contraction network activity was detected when various variants of the PHC1 tandem domain were overexpressed in cells, showing that this domain does not act in a dominant negative fashion as proposed earlier (Figure 15 and Figure 16). However, intramolecular interactions are often preferred compared to intermolecular interactions due to the high local proximity of the binding partners within the same molecule. Therefore, the observations presented in this thesis do not entirely rule out an autoinhibitory component in the regulation of ROCK1. Such an autoinhibitory interaction could be affected by the interaction between Rho and the PHC1 and/or RBD domains and might thereby affect the activity of the distant N-terminal kinase domain.

(c) Via a complex that includes several Rho molecules at the plasma membrane that regulate the plasma membrane binding of ROCK1. This idea is developed in more detail in the following section that lays out a potential mechanism that extends the original “molecular ruler hypothesis” of Truebestein et al. (2015).

## 3.6 The “stabilized molecular ruler hypothesis” for ROCK1 function

The new insights about the Rho interaction sites identified in this study form the basis for the following model (Figure 29):

ROCK1 recruitment by Rho can occur via two different Rho binding sites within ROCK1: the previously known RBD within the coiled-coil and/or the novel binding site within the PHC1 tandem domain that was identified in this thesis. The binding of Rho to the RBD could be facilitated through a kink region identified via AlphaFold, that enables bending of the coiled-coil and an interaction between plasma membrane bound Rho and the RBD. The simultaneous binding of the two PHC1 domains to two Rho molecules at the plasma membrane, combined with the binding of a Rho molecule to the RBD, could enable a stable and perpendicular orientation of the coiled-coil domain at the plasma membrane. Presumably, other proteins such as Shroom proteins (Zalewski et al., 2016) could support the correct positioning of ROCK1. In the fully extended conformation, the active kinase domain can reach through the cell cortex to activate non-muscle Myosin II (Salmerón-Sánchez and Dalby, 2016). Other effector proteins within the cell cortex can also be reached by ROCK1.

A mechanism based on interactions of multiple Rho molecules with ROCK at the plasma membrane could also explain how information from interactions between the PHC1 domain and active Rho could be transmitted to the distant N-terminal kinase domain. This transmission could be realized by the modulation of the perpendicular orientation of ROCK. Based on this model, the interaction between the RBD and Rho in the plasma membrane would be most important to stabilize such a perpendicular orientation. The structural model shown in Figure 25 supports this idea. In wild-type ROCK1, three Rho molecules can bind to one ROCK dimer. If Rho binding is disrupted by the point mutations in the mPHC1 domains, the Rho molecules at the plasma membrane can only bind to the RBD. Consequently, this could result in an up to threefold increase in the number of ROCK proteins that bind to Rho via the RBD. In other words, the additional Rho binding sites in the PHC1 domains could compete with the RBD for limiting amounts of active Rho and thereby prevent maximal activation of Myosin. Together with the RBD, the positive charges at the surface of the PHC1 tandem domain are expected to electrostatically interact with the plasma membrane to sufficiently stabilize its interaction, especially after enforced plasma membrane recruitment.

This prompts the question of why such an apparently inefficient activation mechanism for ROCK might have evolved. Firstly, the binding sites in the PHC1 tandem domain ensure that more ROCK can be recruited in the absence of enforced plasma membrane targeting. Secondly, it is conceivable that this mechanism acts as a fail-safe to prevent over-activation of

Myosin at longer time scales. RhoGTPase activity is amplified by positive feedback with its activating Lbc-type GEFs (Medina et al., 2013; Graessl et al., 2017; Kamps et al., 2020). This results in exponential growth in Rho activity. The activation of one ROCK molecule by each Rho molecule might stimulate contraction too rapidly. However, given the necessity of three Rho molecules, a bottleneck emerges, thereby attenuating the amplification of Rho to prevent excessive cell contraction.

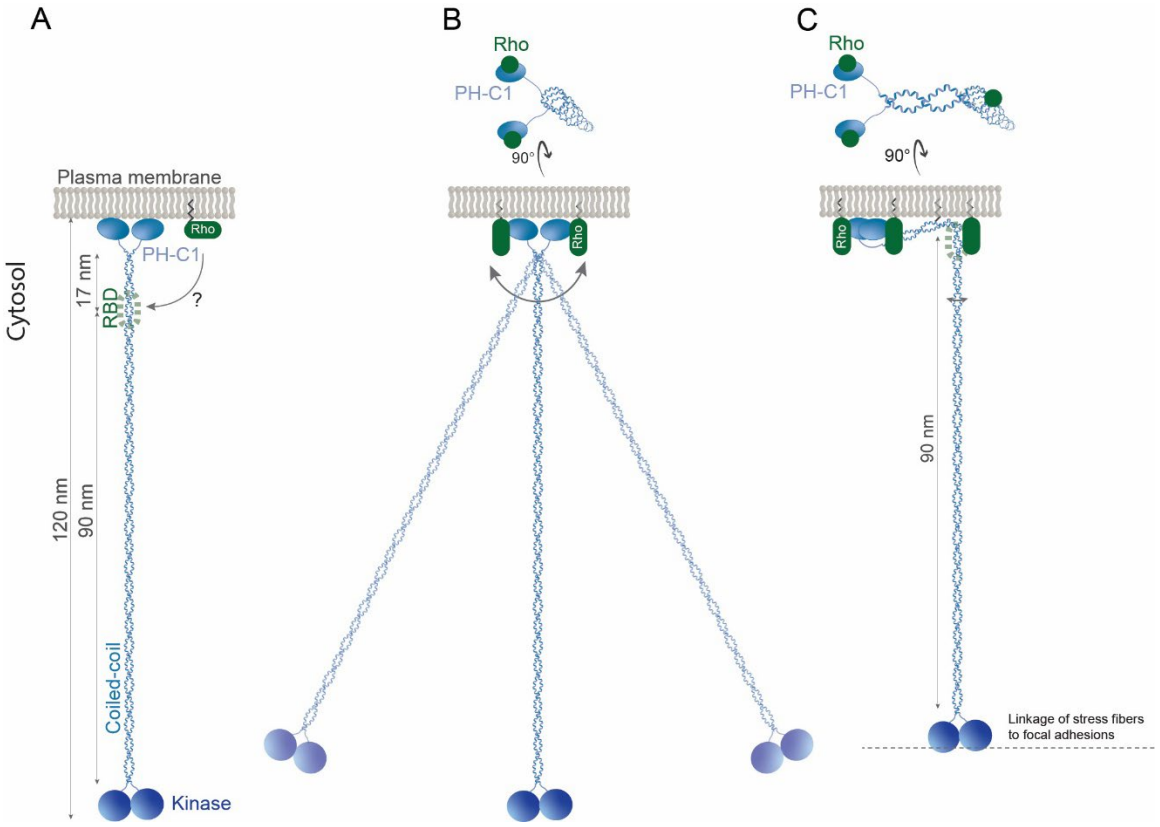


*Figure 29: Proposed model of ROCK1 Activity Regulation. (A) Illustration of the "Molecular Ruler" hypothesis (Truebestein et al., 2015)). According to this model, ROCKs are always bound to the plasma membrane via their PH domain in their fully extended conformation. However, the regulatory mechanism of ROCK in this model was unclear, as the previously identified RBD (Rho binding domain) within the coiled-coil of ROCK is located at a considerable distance from active Rho bound to the plasma membrane. (B) The newly identified Rho binding site in the PHC1 domain can resolve this problem and recruit ROCK1 to active, plasma-membrane bound Rho. The linkers connecting the Rho-bound PHC1 domain to the coiled-coil domain are flexible. Consequently, ROCK can pivot back and forth when it is only bound via the PHC1 tandem domain. This could lead to a reduction of the average distance between the plasma membrane and the ROCK1 kinase domain, thereby reducing its efficiency to reach Myosin within the cell cortex. (C) It is postulated that a more stable perpendicular orientation of ROCK1 could be achieved through additional interactions with the plasma membrane and active Rho molecules. This could be achieved, for instance, by a kink in the coiled-coil structure, directly C-terminal to the RBD domain (see also Figure 25). Figure adapted from Gierse et al. (2025b).*

# Part II: Regulation of cell morphodynamics by microtubules

Part II of this thesis pertains to a collaborative research project aimed at applying a newly synthesized photocaged microtubule stabilizing compound. I investigated the hypothesis that local photo-uncaging of this compound leads to local stabilization of microtubules within cells, and that this leads to a localized change of cell shape. As microtubules actively participate in morphodynamic signal networks, this part is highly relevant to the overarching theme of this thesis.

# 4 Introduction

Changes in cell shape are driven by dynamic rearrangements of the cytoskeleton. Part I focused on the role of the molecule motor Myosin on actin filaments in this process, however, another major cytoskeletal component, the microtubules, can also influence the shape of a cell. Microtubules are best known for their ability to act as tracks for intracellular transport. However, in addition, microtubules can also contribute to the stabilization of the cell shape by resisting compressive forces (Brangwynne et al., 2006; Rhee et al., 2007). Furthermore, recent findings have emerged that underscore their ability to stabilize cell extensions within a three-dimensional culture environment (Martins and Kolega, 2012; Bouchet et al., 2016). In particular, it has been demonstrated that microtubules play a critical role in preventing the retraction of pseudopodia (Bouchet et al., 2016) and promoting efficient migration by acting as supportive struts (Martins and Kolega, 2012; Bouchet and Akhmanova, 2017). This function is particularly important in resisting membrane tension and contractility (Bouchet et al., 2016; Shakiba et al., 2020).

In addition, microtubules have the ability to push the plasma membrane forward, in particular, via forces that are generated by interactions with the motor protein dynein in the cell cortex which pushes microtubules towards the leading edge (Dujardin et al., 2003; Dehmelt et al., 2006; Mazel et al., 2014). Furthermore, the stimulation of cell protrusions by growing microtubules was also shown to be associated with the activation of the protrusion regulator Rac (Waterman-Storer et al., 1999), and microtubules can facilitate cell protrusion by enabling

the transport of recycling endosomes that contain migration-related signaling molecules (Palamidessi et al., 2008).

Cell contraction is also regulated by microtubules. In particular, the Rho activator GEF-H1, which was extensively used primarily as a tool in Part I, is well-known to be inhibited by its interaction with microtubules and can be released from depolymerizing microtubules to stimulate cell contraction (Krendel et al., 2002; Chang et al., 2008; Pineau et al., 2022). Overall, it has been shown that stiff substrates promote the release of GEF-H1 from microtubules, thereby facilitating migration (Seetharaman and Etienne-Manneville, 2020).

## 4.1 Dynamic instability of Microtubules

Many functions of microtubules are enabled by a process that is called “dynamic instability”. This process is defined as the ability of microtubules to transition from a growing to a shrinking state (catastrophe) and vice versa, from shrinkage to growth (rescue) (Mitchison and Kirschner, 1984). Dynamic instability enables a semi-stochastic search-and-capture mechanism that is thought to be involved in targeting of microtubule ends to specialized, focal structures, such as kinetochores or focal adhesions (Kaverina et al., 1998; Stehbens and Wittmann, 2012). Together with GEF-H1, microtubule ends were shown to have a signaling function during such encounters that can stimulate the disassembly of focal adhesions (Kaverina et al., 1998). Furthermore, the release of GEF-H1 from microtubules was also shown to couple Myosin contractility to cell substrate stiffness (Etienne-Manneville, 2013; Schmidt and Stehbens, 2024). The search-and-capture mechanism is particularly important for mitosis, where it facilitates the formation of the metaphase spindle by increasing the likelihood of encounters between dynamic microtubule ends and kinetochores on chromosomes (Kirschner and Mitchison, 1986).

### 4.1.1 Microtubule destabilizing and stabilizing compounds

Especially, due to their role in mitosis, microtubules are prime targets for cancer therapy. As microtubule dynamics are critical for this process, both microtubule-destabilizing and microtubule-stabilizing compounds were developed. Typical destabilizing compounds bind the individual building blocks of microtubules, the alpha-beta tubulin dimer, and prevent them from polymerizing (Keates and Mason, 1981; Sackett and Varma, 1993; Carney et al., 2016).

Stabilizing compounds typically bind to the tubulin polymer surface and interfere with the depolymerization process (Fanale et al., 2015).

The first microtubule stabilizing drugs that were discovered and utilized in anticancer chemotherapy were taxanes (Wani et al., 1971). Over the years, a variety of other microtubule stabilizing drugs were identified and developed (Ojima et al., 1999), including the epothilones. In dividing cells, such as cancer cells, these compounds induce mitotic arrest, leading to cell death due to the formation of an aberrant mitotic spindle (Wartmann and Altmann, 2002). Due to their high solubility in water and high activity, they present an alternative to paclitaxel in anticancer therapy. Furthermore, they are easy to modify, which facilitates the synthesis of analogs (Altmann et al., 2000; Wartmann and Altmann, 2002).

In addition to their application in cancer therapy, microtubule-stabilizing and -destabilizing compounds can also be utilized in research to investigate the function of the cytoskeleton. In contrast to standard genetic perturbations, or ectopic expression of cytoskeletal regulators, which only enable long-term perturbations, the application of such compounds enables much faster perturbation. However, typical applications of these compounds affect microtubules throughout the cell, thus lacking spatiotemporal precision.

### 4.1.2 Cou-Epo: a photouncageable microtubule stabilizer

One method to circumvent these limitations involves the utilization of photocontrolled compounds. In the past, several photocontrollable microtubule destabilizers were developed, however, the number of microtubule stabilizers was limited. This is a significant problem, as stabilization facilitates a more direct way to investigate microtubule-dependent processes (Schmitt et al., 2024).

Photocontrol includes both reversible photoswitching and irreversible photouncaging. Previous studies reported reversible photoswitchable microtubule stabilizers based both on taxanes (Müller-Deku et al., 2020) and epothilones (Gao et al., 2022). It has been demonstrated that these agents indeed facilitate the controlled stabilization of microtubules within specific spatial and temporal parameters. However, a notable disadvantage associated with this approach is that the magnitude of increased bioactivity upon light activation is limited to approximately sixfold, which was primarily due to a weaker potency compared to

the parental drugs. Moreover, these compounds have not demonstrated efficacy *in vivo*, but rather, their activity has been observed exclusively in cell culture settings.

Due to the aforementioned disadvantages, Schmitt and colleagues (Schmitt et al., 2024) endeavored to develop novel derivatives of ZK-epothilone (ZK-Epo), with the objective of producing the first photouncageable epothilone for irreversible photoactivation. The ZK-Epo compound was selected as the starting point due to its high potency of less than 1 nM in combination with its solubility in water at that specific concentration. Moreover, it has been demonstrated to enter cells with high efficiency and it evades efflux pumps that typically confer multidrug resistance (Klar et al., 2006).

Introducing a photocage group at the C7 position of this compound yielded CouEpo (Schmitt et al., 2024), which was effectively uncaged with wavelengths in the range from 385-460 nm. This enabled uncaging with common lasers used for microscopy, including the 405 and 440 nm lines. This characteristic represents a substantial benefit, as it eliminates the necessity for UV light. A notable benefit of this approach is that the photocage remains largely intact when illuminated with the 514nm laser line which can be used to excite the very common GFP or YFP fluorescent proteins (Schmitt et al., 2024).

Initial investigations of CouEpo focused on cell proliferation, which confirmed the photoactivatable ability of this compound to interfere with this cellular process. More detailed analysis was based on the EB3 comet assay, which is a method to monitor the dynamics of microtubule polymerization. In this assay, microtubule ends are visualized and tracked based on their fluorescent labeling using end binding protein EB3. In this assay, the growing tips of microtubules are typically visualized in the shape of comets. Previous work has shown that microtubule stabilization paradoxically leads to an inhibition of microtubule growth. This has been attributed to the quick consumption of tubulin monomers, thus inhibiting microtubule dynamics, which is associated with a decrease in both velocity and the number of EB3 comets. Indeed, it was observed that the EB3 comet count decreased significantly in CouEpo-treated cells (75 nM) when exposed to laser scanning illumination at 405 nm (whole field of view illumination) (Schmitt et al., 2024).

# 5 Results

These previous results already demonstrated that CouEpo can be controlled via photouncaging, however, the measured effect was indirect and was based on the depletion of tubulin in the entire cell, thus lacking subcellular selectivity.

The subsequent experiments performed in this thesis focused on more direct investigation of local microtubule enrichment related to local uncaging of CouEpo in Ptk1 cells that stably express GFP-tubulin[4].

## 5.1 Localized and time resolved CouEpo uncaging

### 5.1.1 Increased microtubule density at uncaging spot

The first objective was to test if the local uncaging of CouEpo (100 nM total concentration) results in the local enrichment of microtubules. To test this hypothesis, a diffraction limited spot at the cell edge of Ptk1 cells was illuminated (cyan spot in Figure 30A). At this position, light pulses were applied at 100-second intervals while acquiring images in TIRF mode at 514 nm. As these images were acquired in TIRF mode, the observation was limited to microtubule sections that get very close to the plasma membrane at the cell cortex. The remaining, cytosolic, long microtubule filament sections were not detected. It was hypothesized that an increase in microtubule density in one cell region would also lead to an increase in their density within the TIRF field, leading to an increase in the corresponding fluorescent signal. Indeed, as expected based on this hypothesis, a substantial increase in the GFP signal close to the photoactivation spot was observed (Figure 30A-B).

To analyze this effect quantitatively, the front versus back regions of the cell were defined with respect to the location of the photoactivation spot. First, the front-back axis was defined based on the photoactivation spot and the cell's centroid, which was detected automatically using a custom-made ImageJ macro. Subsequently, the fluorescence intensity was measured at the periphery of the cell within 22.5° of the front-back axis in both directions to define the front and back regions of the cell (Figure 30C). A comparison of the front (Figure 30D left and Figure 30F) to the back (Figure 30E left and Figure 30F) reveals that the GFP-tubulin signal increases

[4] Generated by Anja Biesemann (TU Dortmund) in the lab of Leif Dehmelt (TU Dortmund).

only in the front, while the back exhibits no response. The DMSO control exhibited a slight decrease in GFP-tubulin intensity in the front (Figure 30D) of the cell, which may be attributable to bleaching or phototoxicity. Thus, the effect in the front of CouEpo treated cells is rather underestimated. The statistical analysis confirmed the increase in microtubule density originating from the CouEpo-uncaging. A comparison of the front region intensity change in microtubules of CouEpo-treated cells and a DMSO control reveals a statistically significant difference (Figure 30D, right). In addition, a comparison of the CouEpo-treated front and back measurements reveals a substantial difference (Figure 30F), confirming the effectiveness of photoactivation as well as caging in absence of light.

### 5.1.2 Local photoactivation induces cell protrusion

Interestingly, it was observed that a significant number of cells extended protrusions towards the photoactivation spot (Figure 30G). To quantify this effect, a region of interest (ROI, illustrated in yellow in Figure 30G) was defined around the illumination spot, and the area within this ROI that is covered by the cell was measured (see right panel in Figure 31G). A subsequent statistical analysis confirmed this effect after uncaging of CouEpo, while no effect was detected in DMSO control cells (Figure 30H and Figure 30I, right). The control cells even exhibited a slight retraction from the photoactivation site. A paired analysis on a single cell basis also confirmed this observation (Figure 30I).

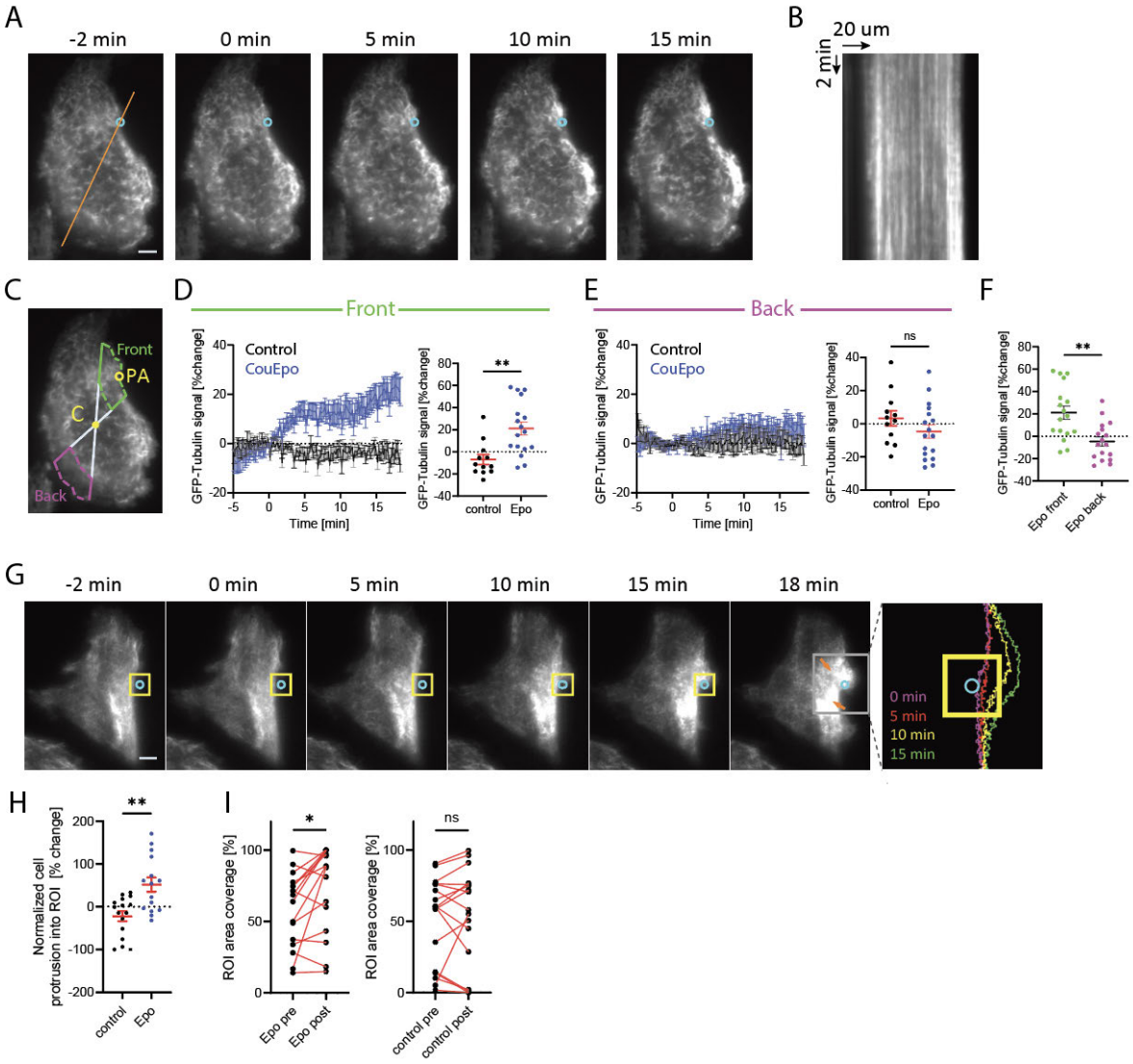


*Figure 30: Local increase in microtubule density in response to local uncaging of a photocaged Epothilone microtubule stabilizer. (A) Representative total internal reflection fluorescence microscopy (TIRF-M) images of Ptk1 cells expressing GFP-tubulin. Cells were treated with 100 nM caged Epothilone (CouEpo) and local photoactivation started at time point 0 min at the cell edge indicated by cyan circles. (B) Kymograph analysis of GFP-tubulin signals in the cell shown in A. Analysis was performed along the indicated orange line. (C) Schematic representation for quantification of GFP-tubulin signals near the photoactivation site (Front) and at the opposite side of the cell (Back). The indicated front and back regions were defined based on a line that connects the photoactivation site (PA) and the cell centroid (C), spanning 45° laterally within 12µm from the cell edge. (D) Kinetics of GFP-tubulin signal change in the front regions in control (vehicle DMSO) or caged Epothilone treated cells (left) together with quantification and statistical analysis of the signals, 18 min after starting the photoactivation pulses. (E) Kinetics of GFP-tubulin signal change in the back regions in control (vehicle DMSO) or caged Epothilone treated cells (left) together with quantification and statistical analysis of the signals, 18 min after starting photoactivation. (F) Quantification and statistical analysis of the response of cells treated with CouEpo, right before and 18 min after starting photoactivation. (G) Representative total internal reflection fluorescence microscopy (TIRF-M) images of Ptk1 cells treated analogously as in A. The time series demonstrates the cell protrusion into the yellow measurement region. The right panel represents the region corresponding to the grey dotted box in the adjacent panel. Colored lines indicate the cell border at successive timepoints during photoactivation. The yellow box indicates the region of interest (ROI) that was used to quantify*

*protrusion near the photoactivation site (cyan circle). (H) Quantification and statistical analysis of the cells' protrusion into the given ROI, 18 min after starting photoactivation. (I) Quantification and statistical analysis of the migrative response of cells treated with CouEpo, right before and 18* min after starting photoactivation. *Error bars represent standard error of the mean (SEM) from 3 independent experiments each. *: p < 0.05. **: p < 0.01, ns: non-significant, unpaired t-test (D-F, H) and paired t-test (I), scale bar = 10 µm, 0.26 µm/pixel.* Figure adapted from Schmitt et al. (2024).

# 6 Discussion

## 6.1 CouEpo facilitates the spatiotemporal stabilization of microtubules

The experimental results demonstrated that CouEpo photouncaging can be used to manipulate microtubule stability with subcellular resolution. During photouncaging of CouEpo at a specific location in the periphery of the cell, a consistent increase in GFP-tubulin intensity was observed (Figure 30A, G). In this region, the signal exhibited significant variation, likely attributable to the intrinsic dynamics exhibited by microtubules.

It has been well documented that microtubules exert a positive influence on cell protrusions in fibroblasts and epithelial cells, such as the Ptk1 cells utilized in this study (Etienne-Manneville, 2013). As delineated in the introduction, this positive regulation of protrusion can be attributed to multiple mechanisms. On the simplest level, the process of microtubule growth can generate a pushing force in simplified *in vitro* models (Dogterom and Yurke, 1997). Additionally, microtubules have been shown to counteract contractile forces due to their bending rigidity (Gittes et al., 1993). Also, microtubule-dependent transport of signaling molecules that positively affect protrusion (Palamidessi et al., 2008) could contribute to the observed effect. Finally, the interaction of microtubules with dynein motors at the cell cortex could also transduce a mechanical force on individual microtubule filaments into a forward pushing force (Dehmelt et al., 2006). The stabilization of microtubules resulting from photouncaging of CouEpo could enhance the effects of the aforementioned mechanisms. The observed reduction in the area of ROI coverage in DMSO control cells could be attributed to cell stress resulting from photoactivation, which typically leads to cell contraction (Boudreau et al., 2016).

In conclusion, these results demonstrate that CouEpo can be uncaged both with high temporal and high spatial precision. This enables more direct investigations into the subcellular role of microtubules in cells and potentially also in more complex systems, such as cancer spheroids, tissue models or living organisms.

# 7 Methods

## 7.1 Molecular Biology

### 7.1.1 Plasmid construction

The following section will describe the various methods for generating new plasmids.

#### *7.1.1.1 PCR amplification*

To truncate plasmids and to amplify fragments for Gibson Assembly reactions (see below), Q5® High Fidelity DNA Polymerase from NEB was utilized. The PCR reactions were set up in two distinct formats: 50 µl reactions, subdivided into three tubes to perform the reaction at multiple annealing temperatures, and 20 µl reactions, set up to perform the reaction at a single, specific annealing temperature. The composition of these reactions is outlined in the subsequent table.

*Table 1: Composition of Q5 High Fidelity Polymerase Chain Reaction.*

| **Component** | **Volume [µL]** | **final concentration** |
|---|---|---|
| 5X Q5 reaction buffer | 10 | 1 X |
| 10 mM dNTPs | 1 | 200 µM |
| Fwd Primer (10 µM) | 2.5 | 0.5 µM |
| Rev Primer (10 µM) | 2.5 | 0.5 µM |
| Template DNA | X | 100 ng |
| Q5 High-Fidelity DNA Polymerase | 0.5 | 0.02 U/µL |
| Enhancer | 0-10 | 0-10 % |
| total Volume | Up to 50 | |

Following the setup of the reaction on ice, in which the polymerase was added as the final step, the tubes were loaded into a thermocycler, and the following settings were employed:

*Table 2: Q5® High Fidelity Polymerase Chain Reaction Thermocycler settings.*

| Step | T/ °C | t/ sec | |
|---|---|---|---|
| **Initial Denaturation** | 98 | 50 | |
| **Denaturation** | 98 | 25 | |
| **Annealing** | 55-72 | 30 | 35x |
| **Extension** | 72 | 30s/kp | |
| **Final Extension** | 72 | 120 | |
| **Hold** | 10 | | |

### *7.1.1.2 Site directed mutagenesis*

Two introduce mutations into existing DNA sequences, two distinct site-directed mutagenesis protocols were used:

For the Rnd3 binding domain within ROCK1 the Phusion® Polymerase was used. The linear product of the PCR reaction was purified using a QIAquick PCR Purification Kit and subsequently transformed into chemical competent Top10 E. coli (see later). The composition of the PCR reactions is outlined in the subsequent table.

*Table 3: Composition of Phusion® Polymerase Chain Reaction.*

| Component | Volume [µL] | Final concentration |
|---|---|---|
| 5x Phusion HF Buffer | 4 | 1X |
| 10 mM dNTPs | 0,4 | 200 µM |
| Fwd Primer (10 µM) | 1 | 0.5 µM |
| Rev Primer (10 µM) | 1 | 0.5 µM |
| Template DNA | X | 100 ng |
| DMSO | 0-2 | 0-10% |
| Phusion High Fidelity DNA Polymerase | 0,2 | 2 U/mL |
| $H_2O$ | Up to 20 | |

Following the setup of the reaction on ice, the tubes were loaded into a thermocycler, and the following settings were employed:

*Table 4: Phusion® Polymerase Chain Reaction Thermocycler settings.*

| Step | T / °C | T / min | |
|---|---|---|---|
| **Initial denaturation** | 98 | 03:00 | |
| **Denaturation** | 98 | 00:10 | 30 |
| **Annealing** | 55-60 | 00:15/kb | |
| **Extension** | 72 | 02:00 | |
| **Final extension** | 72 | 20:00 | |
| **Hold** | 10 | | |

To introduce mutations within the RBD domain of ROCK1, standard QuickChange mutagenesis was performed via PCR using Novagen® KOD Hot Start DNA Polymerase. In order to introduce the desired mutations, the primers for the reaction overlapped by at least 10 base pairs. This ensured cyclization of the PCR product in the reaction tube. The product was transformed into chemical competent GH371 E. coli (see later). The composition of the PCR reactions is outlined in the subsequent table.

*Table 5: Composition of KOD Hot Start DNA Polymerase Chain Reaction.*

| Component | Volume [µL] | final concentration |
|---|---|---|
| DNA | 1.0 | 1 ng/µL |
| Fwd primer (10 µM) | 0.6 | 0.3 µM |
| Rev primer (10 µM) | 0.6 | 0.3 µM |
| MgSO4 (25 mM) | 1.2 | 1.5 mM |
| dNTPs (2mM) | 2.0 | 0.2 mM |
| KOD buffer (10X) | 2.0 | 1X |
| KOD polymerase | 0.4 | 0.02 U/µL |
| MilliQ H2O | up to 20 | |

Following the setup of the reaction on ice, the tubes were loaded into the pre-heated (95°C) thermocycler, and the following settings were carried out:

*Table 6: KOD Hot Start DNA Polymerase Chain Reaction Thermocycler settings.*

| Step | Temp. (°C) | Time [min] | |
|---|---|---|---|
| **Initial denaturation** | 95.0 | 02:00 | |
| **Denaturation** | 95.0 | 00:20 | |
| **Annealing** | X* | 0:15/kb | 30x |
| **Extension** | 70.0 | 05:00 | |
| **Final extension** | 70.0 | 04:00 | |
| **Hold** | 4.0 | Hold | |

X*: lowest melting temp. of your primer

### *7.1.1.3 DNA restriction*

Plasmid DNA was subjected to restriction enzyme digestion using enzymes from New England Biolabs to linearize the vector backbones for Gibson assembly. The reactions were prepared on ice and subsequently subjected to incubation in a pre-heated thermocycler at 37°C for a duration of three hours. After the incubation period, the enzymes were subjected to heat inactivation at temperatures of 65°C or 80°C, depending on the specific enzyme utilized. The quantity of restriction enzyme and DNA was used in accordance with the protocol provided by NEB and adjusted based on previous results.

### *7.1.1.4 DNA analysis and purification by Agarose gel*

The analysis of PCR products and restriction digests was conducted using agarose gel electrophoresis. For the purpose of analysis, 3 µL of the product under consideration was loaded onto the gel. The gels were prepared according to the following formulae:

*Table 7: Agarose gel concentration for resolving DNA fragments.*

| Gel Percentage [w/v] | DNA size range [bp] |
|---|---|
| 0.5 | 1-30 kb |
| 0.7 | 800 bp - 12 kb |
| 1.0 | 500 bp - 10 kb |
| 1.2 | 400 bp - 7 kb |
| 1.5 | 200 bp - 3 kb |
| 2.0 | 50 bp - 2 kb |

In certain instances, the purification of PCR products or restriction digests necessitated the utilization of the QIAquick Gel Extraction Kit. For the aforementioned purpose, the PCR/digestion products were applied to the gel in the following manner: first, the ladder; subsequently, a small quantity of the product; then, as many pockets as necessary loaded with a substantial amount of the product; finally, again, a small quantity of the product and ladder. Prior to the UV illumination or incubation with ethidium bromide, the lines that contained the bulk of the desired product were meticulously excised from the gel and saved for the next step. The remaining gel pieces with the small quantity of the product were incubated with ethidium bromide for 15 min and washed with $ddH_2O$ for 2 min. The bands of interest in these gel pieces were excised under the illumination of UV light. Then, all gel pieces were meticulously reassembled, and the bulk of the desired product was precisely excised without exposure to ethidium bromide or UV light. The isolation of the DNA from the excised gel fragment was carried out using the QIAquick Gel Extraction kit. The manufacturer's protocol was followed for this procedure.

#### *7.1.1.5 Gibson assembly reaction*

The Gibson assembly reaction was performed in accordance with the manufacturer's guidelines, employing the HiFi Assembly reaction kit from NEB or a self-made 1.33x Gibson Master mix.

Plasmid backbone and PCR-amplified inserts with compatible overlaps were mixed in a molar ratio of either 1:2 or 1:3, depending on the reaction. The total volume of the plasmid/insert mixture was 5 µL. This was added to the 15 µl 1.33x Gibson Master mix, and the reaction was

subsequently incubated for 3-5 hours at 50°C. Subsequently, the product was transformed into *E. coli* (see below).

To generate the ROCK1 PH domain mutants, synthetic DNA strands (GeneStrands) were synthesized by Eurofins and amplified with primers containing the desired overhangs to obtain the insert for the assembly reaction. The corresponding backbone was subjected to PCR amplification due to the absence of suitable restriction sites within this region.

A modified version of Gibson assembly was used to truncate specific regions from plasmids. In this procedure, the entire plasmid was amplified, with the exception of the specific segment intended for deletion. For the amplification process, one of the utilized primers was designed to possess a compatible overhang with the other primer. This was done to ensure the efficient cyclization of the primers within the reaction tube prior to the process of transformation.

The web tool NEBuilder from New England Biolabs was used to design the primers for all Gibson reactions.

#### *7.1.1.6 Sequencing of plasmid DNA*

Plasmid DNA was subjected to sequencing using the Economy Run, E. coli NightSeq, or full plasmid sequencing from Microsynth/Seqlab. The plasmids and colonies were prepared in accordance with the established protocols. In the course of conducting full plasmid sequencing reactions, it was determined that a concentration of 25 ng/µL should be utilized instead of the recommended concentration of 20 ng/µL. This adjustment was made based on the frequently observed tendency that DNA concentrations were overestimated using the NanoDrop method (see below).

### 7.1.2 Determination of DNA concentration

The concentration of purified DNA was measured with a Nanodrop™ 2000 UV-Vis spectrophotometer by detecting the light absorption of the DNA sample at 260 nm. The ratio of the absorption maxima of DNA (260 nm) and (280 nm) was used to assess the purity of the DNA sample. A ratio of ~1.8 was considered pure DNA. Autoclaved ddH2O was utilized as a reference standard for the calibration process.

### 7.1.3 Transformation of competent *E. Coli* cells

In this thesis, two distinct transformation methodologies were used: heat shock and electroporation.

#### *7.1.3.1 Heat shock*

Chemical competent cells (see Table 16) were thawed on ice for approximately 10 minutes. Subsequently, 1-5 µl of plasmid DNA from Gibson assembly reactions were added to a 25 µl aliquot of cells. The mixture was then incubated for 30 minutes on ice. Afterwards, a 45-second heat shock at 42°C was initiated, followed by a two-minute incubation on ice. Prior to the initiation of the incubation process at 37°C and 600 rpm for a duration of 1 h, 400 µl of SOC medium was added to the cells. Subsequent to this incubation period, the cells were subjected to a centrifugal process at 8,000 rpm for a duration of 10 seconds. This procedure was followed by the removal of 300 µL of the cell's culture supernatant. The pellet was resuspended in the remaining liquid, and the suspension was plated onto an LB agar plate containing the corresponding antibiotic. The samples were then spread out using glass beads. The plates were subsequently inverted and incubated at 37°C overnight. For storage, the agar plates were sealed with parafilm and stored at 4°C for up to 6 weeks.

For the retransformation of established plasmids, 0.5 µl of plasmid was added to 25 µl of cell suspension, and the cells were only incubated for 10 min on ice instead of 30 min. Subsequent to the completion of each step as delineated above, 50 µL of the suspension was applied to an agar plate, and the cells were incubated over night as described above.

#### *7.1.3.2 Electroporation*

The application of electroporation was only pursued when a sufficient quantity of colonies could not be obtained through the utilization of the heat shock transformation protocol.

A total of 25 µL of electrocompetent cells were thawed on ice for a brief period. Subsequently, 1-2 µL of plasmid DNA derived from assembly reactions or 0.5 µL of previously purified plasmid were added to the cells. Next, the cell suspension was transferred into the electroporation cuvette, and electroporation was performed at 1800 V for 3 seconds. Immediately following the electroporation, 400 µl of SOC medium were added to the cells, and the suspension was then incubated for 1 h at 37°C at 600 rpm. The spreading of the

sample onto the agar plates and subsequent incubation over the course of a night period was performed analogous to the chemical competent heat shock transformation protocol.

### 7.1.4 Colony PCR

In the event that the process of subcloning proved challenging, a procedure known as colony PCR was performed. The objective of this procedure was to identify potential positive clones based on their band size prior to the process of sequencing. To this end, a Taq polymerase PCR was prepared as outlined in the NEB protocol. The initial DNA educt was designated as 0 µL since the volume of the bacterial colony used as the DNA template was negligible.

The colonies were picked using a pipette tip and subsequently transferred into PCR tubes and then exposed to microwave radiation for 20 seconds and subsequently frozen for 10-20 minutes to ensure the lysis of the cells. After the preparation of a PCR master mix on ice, 10 µL of the solution were transferred into each PCR tube containing the lysed cells. Finally, the PCR cycling reaction was performed, and the resulting product was subjected to agarose gel electrophoresis for analysis.

### *7.1.5* Preparation of Glycerol stocks of transformed *E. Coli* and inoculation of new cultures for plasmid isolation

A volume of 500 µL of freshly cultivated *E. coli* cells, characterized by a relatively low density and thus still within their growth phase, was added to 500 µL of 50% glycerol in a cryotube. The contents of the cryotube were then subjected to a process of inversion, thereby facilitating the mixture of the two liquids. For the purpose of long-term storage, the mixture was stored at -70°C.

In instances where the production of new plasmids preps was required, a small volume of the frozen glystock was added directly into LB medium containing the appropriate antibiotic. The mixture was then cultivated at 37°C overnight. Subsequently, the purification of the plasmid was carried out (see next section).

### 7.1.6 Isolation of plasmid DNA from *E. Coli* cells

For isolation and purification of plasmids, 5 mL of LB medium containing the necessary antibiotics were inoculated with a single E. coli colony in a 15 mL reaction tube. The cell suspension was then subjected to an overnight incubation at a temperature of 37°C and 200

rotations per minute (rpm). The lid of the reaction tube was not firmly closed, thus facilitating the exchange of air. Following the incubation period, the suspension was transferred into a 2 mL microcentrifugation tube and subjected to a centrifugation process at 8,000 rpm for a duration of 3 minutes. The supernatant was then discarded, and the DNA was isolated from the pellet using the QIAprep Spin Miniprep Kit from Quiagen. The elution of the plasmid was accomplished by adding 50 µL of autoclaved ddH2O.

In instances where a significant quantity of plasmid was required, a Maxiprep procedure was conducted using the Plasmid Plus Maxi Kit from Quiagen with 200 mL of cell culture. The protocol from Qiagen was performed for the high copy plasmids.

## 7.2 Cell Culture

### 7.2.1 Maintenance of adherent mammalian cells

U2OS or Ptk1 cells were cultured using standard protocols. Briefly, cultures were split at about 80% confluency. Following the removal of the culture medium, the cells were promptly washed with Dulbecco's phosphate-buffered saline (DPBS) and detached using 2 mL of trypsin/EDTA for 4 minutes at 37°C and 5% carbon dioxide. Next, warm medium was added to the cells, followed by discarding a fraction of the cells. Typically, cell density was reduced to 20% confluency if the next splitting was scheduled in two days, and to 10% confluency if it was scheduled in three days. In the final step, cells were seeded into a new cell culture dish, in a volume of 10 mL. The cells were then incubated at 37°C and 5% CO2 until the next splitting procedure.

### 7.2.2 Cryopreservation of mammalian cells

To harvest the cells for freezing, they were first treated identical to the maintenance procedure described above until the resuspension step after centrifugation. During centrifugation, a 10% DMSO-containing medium was prepared and 500 µL were added to cryotubes. Subsequently, cells were resuspended in ice-cooled medium, and 500 microliters (containing half the cell suspension of one 100 mm dish) of the cell suspension were transferred into the previously filled cryotube and stored on ice. Subsequently, the tubes were placed in a specialized cryogenic storage apparatus (Mr. Frosty$^{TM}$), to facilitate slow freezing

at a temperature of -70 or -80°C for a duration of 24 hours. Finally, the cryotubes were stored at a temperature of -150°C.

In order to avert any potential damage to the cells caused by DMSO, it was essential to execute the thawing process promptly. Initially, the cryotube, which had been frozen, was placed in a water bath set at 37°C. This was done until only a small piece of ice could be seen. Subsequently, the cell suspension was transferred into 9 mL of warm medium, and the cells were subjected to a centrifugation process at 1000 rpm for a duration of 5 minutes. Lastly, the cells were seeded as outlined in the preceding section.

### 7.2.3 Preparation of microscopy samples

For microscopy, 400 µL of the mammalian cell suspension were placed on an 8-well LabTek (Thermo Fisher Scientific) borosilicate glass-bottom dish. The cells were suspended by trypsinization and then centrifuged for five minutes at 1,000 rpm in a tabletop centrifuge (Eppendorf *Centrifuge 5810 R*). The cell count was then determined using a hemocytometer after resuspension of the pellet in 3 mL culture medium. Depending on the cell line and type of experiment, the cells were diluted to the required density to prepare the desired number of wells in one dish from one single suspension.

For U2OS cells, glass-bottom dishes were coated with a 1% collagen solution (Sigma-Aldrich) in DPBS at room temperature for 30 to 40 minutes. Subsequently, dishes were washed once with DPBS before seeding the cells (14 000-17 000 cells/well) two days prior to microscopy. Ptk1 cells were plated onto untreated glass-bottom dishes (25000 cells/well) one day prior to microscopy.

#### *7.2.3.1 Transient transfection of adherent mammalian cells*

One day after seeding U2OS cells, they were transfected with the required plasmid DNAs for the respective experiment. Transfection was carried out using Lipofectamine 2000 (Invitrogen) and a serum-free medium (Opti-MEM, Gibco), according to the manufacturer's protocol. A 5:2 ratio of Lipofectamine to DNA was used (V/m). For each µl of lipofectamine, 33.33 µl of OptiMEM was added and the mixture was incubated for 5 min prior to addition of plasmid DNA. After 15 min incubation, the mixture was added to the respective well.

#### *7.2.3.2 Sample preparation for imaging of fixed mammalian cells*

Mammalian cells were fixed with formaldehyde 18-22 hours after transfection. 4% formaldehyde in DPBS was warmed to 37 °C and added dropwise to the cells after they were washed once with DPBS. The sample was incubated for 20 minutes at 37 °C, after which it was washed three times with DPBS. The cells were then chemically stained with phalloidin Atto488 (1:1000, Sigma-Aldrich, 49409) and DAPI-Hoechst (1:1000, Sigma-Adrich, 33342) in DPBS overnight. The next day, the cells were washed 3x with DPBS.

The fixed and stained cells were stored for up to five days at 4 °C, sealed with parafilm, and kept in DPBS supplemented with a small amount of formaldehyde as short-term preservative. The formaldehyde-supplemented DPBS was exchanged with fresh DPBS before they were imaged at the microscope. Alternatively, the cells were imaged directly at the microscope.

#### *7.2.3.3 Sample preparation for live-cell imaging of adherent mammalian cells*

Before imaging, the cell culture medium was replaced with a phenol red-free imaging medium supplemented with 10% FBS (Gibco).

#### *7.2.3.4 Nocodazole treatment of adherent mammalian cells*

Nocodazole was used as a microtubule-destabilizing drug, to release GEF-H1 from microtubules and thereby increase Rho activity dynamics within cells (see section 1.3.1). Approximately one hour before imaging, the cell medium was replaced with a phenol red-free imaging medium supplemented with 10% FBS and 30 µM nocodazole.

## 7.3 Microscopy

Live cell experiments were carried out with the incubator set to 37 °C. The actual temperature in the microscope chamber was typically in the range from 32 to 35 °C. Fixed cell experiments were performed at room temperature.

## 7.4 Total Internal Reflection Fluorescence (TIRF)-Microscopy

All TIRF microscopy experiments were performed on an Olympus IX-81 microscope. The microscope was equipped with an Apo TIRF 60x 1.45 oil immersion objective, as well as a TIRF-MITICO motorized TIRF illumination combiner. Images were detected with an EMCCD camera at medium gain (EM gain 100) without binning. Before each experiment, the lasers necessary

for that day's experiment were aligned using a glass-bottom dish marked with black dots on the bottom and filled with water to focus on the correct plane for alignment. TIRF angle adjustments were made individually for each experiment.

All further information about the setup is given in Table 9.

## 7.5 Molecular Activity Painting (MAP)

### 7.5.1 Sample preparation for immobilized Molecular Activity Painting

Experiments were performed according to the protocol described by Kamps et al. (2020). Further optimizations are detailed in the following paragraphs. The workflow is shown in Figure 31 and example transfections are given in Table 21 and Table 22.

For the functionalized/immobilized molecular activity painting (MAP) experiments, 100,000–140,000 U2OS cells were seeded in 6-well plates or 30 mm cell culture dishes on day 1 (Sarstedt, Cell+). The cultures were incubated overnight at 37 °C and 5% $CO_2$. On day two, the glass-bottom dish to be used for imaging was coated with 150 µL of 0.1% poly-L-lysine overnight at 4 °C and sealed with parafilm. At the same time, cells were transfected with the activator presenting artificial receptor construct (activator-PARC), the perturbation construct (eDHFR fused to the protein to be recruited), and the fluorescently labeled response construct (see Section 7.2.3.1, Transfection). Example transfections are given in Table 21 and Table 22.

Day 3 started with further functionalization of the glass-bottom dish. First, the poly-L-lysine was removed, and the surface was washed three times with DPBS. For the next hour, the glass-bound poly-L-lysine was biotinylated using E/Z-Biotin (1 mg/mL). During biotinylation, antibody (12 µl DPBS + 3 µl biotin-labeled anti-VSVG (1 mg/ml, ab34774, abcam)) and streptavidin/Cy7-streptavidin (12µl DPBS + 1 µl Streptavidin (1 mg/ml, Serva) + 1 µl Streptavidin alexa fluor 750 (0.1 mg/ml, life technologies)) solutions were prepared on ice. After biotinylation, the glass bottom dish was washed three times with DPBS, and the remaining liquid was allowed to evaporate at room temperature until the surface was dry. Then, the antibody and streptavidin solutions were mixed, and five 2 µL drops were added to each well (illustrated in Figure 31). The dish was incubated for two more minutes after the last drop was added. Lastly, the dish was washed with DPBS to stop the functionalization. In parallel, the cells were prepared for reseeding about 24 hours post-transfection. First, the cells

were washed with DPBS. Next, cells were treated with either a 25 mM EDTA solution at 37 °C for 25 minutes (old protocol) or an enzyme-free cell dissociation solution for 8-10 minutes (new protocol). After detaching the cells with the aforementioned solutions, they were washed and resuspended in serum-free cell culture medium after centrifugation for five minutes at 1000 RPM. If cells were treated with EDTA for detachment, this washing step was repeated another time. The final pellet was resuspended in 200 µL of FBS-free cell culture medium, and the suspension was plated onto the functionalized glass surface after the DPBS was removed from the wells. After the cells attached for 30-45 minutes at 37°C and 5% $CO_2$, 200 µL of 20% FBS-containing cell culture medium was added on top. The cells were then incubated overnight.

The cells were investigated on day 4. Prior to performing the MAP experiments, however, the cells were incubated with 20 mM photochemical dimerizer (Chen et al., 2017) for 1 hour in FBS-containing imaging medium in the dark. After incubation, the cells were washed three times with medium. Then, after half an hour, a final washing step was performed.

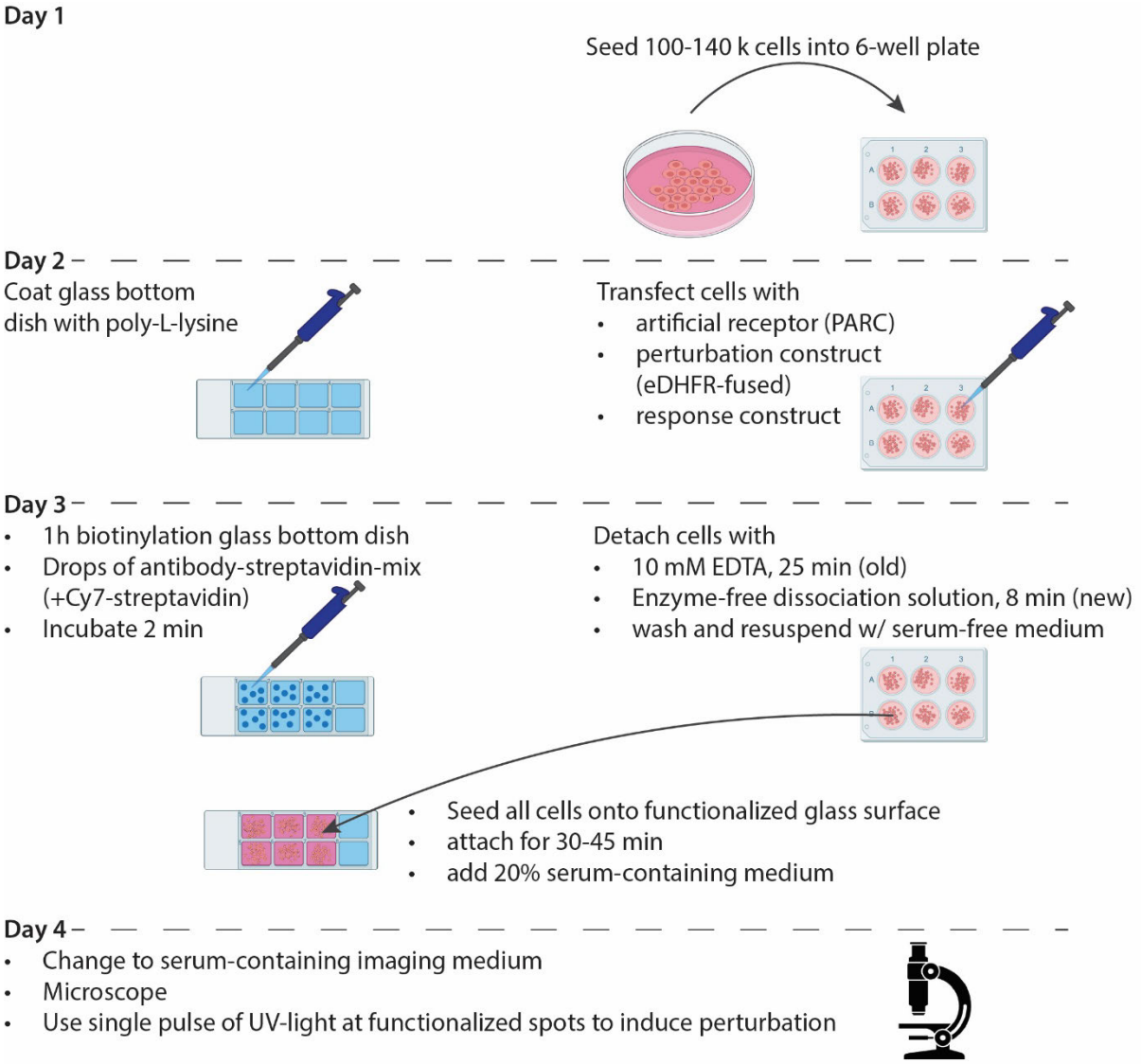


*Figure 31: Workflow for sample preparation in Molecular Activity Painting. Some illustrations were created with BioRender.com.*

### 7.5.2 Photo-uncaging for immobilized Molecular Activity Painting

The TIRF-MITICO illumination combiner was set to FRAP mode and used to focus the 405 nm CellR diode laser into a single spot for the photouncaging of the Nvoc-TMP-Cl photochemical dimerizer.

The uncaging was performed for 400 ms at 180 nW, which was measured directly at the objective (Kamps et al., 2020) and corresponds to 20% laser power. Only one uncaging step was performed per cell.

## 7.6 Cell Attachment Area – Molecular Activity Painting (CA-MAP)

The cell sample preparation was performed as described in section 7.2.3 and sub-section 7.2.3.1. The cells were transfected with the same constructs as described for the immobilized Molecular Activity Painting assay (section 7.5.1, example transfection given in Table 23).

The uncaging of the Nvoc-TMP-Cl photochemical dimerizer was carried out using a 405 nm CellR diode laser set to total internal reflection fluorescence (TIRF) mode in the TIRF-MITICO illumination combiner. The laser intensity was set to 60% (three times more than for spot illumination for functionalized molecular activity painting), and uncaging was performed for 400 ms. Thus, uncaging occurred throughout the entire cell attachment area within the evanescent wave of the TIRF microscope (up to about 100nm distance from the coverslip).

## 7.7 LOVTRAP mediated release of CA-ROCK1

To optogenetically increase the cytosolic concentration of CA-ROCK1 in living cells, the LOVTRAP system was used (Wang et al., 2016). To reduce phototoxicity and enable the release of CA-ROCK1 from mitochondria-targeted LOV domains, a 100x neutral density filter was inserted into the light path of the 445 CellR diode laser. To facilitate release, the laser was set to widefield mode with an intensity of 100% and the cells were illuminated throughout the entire perturbation period, except when taking pictures.

## 7.8 Numerical simulations

To integrate inhibition of Myosin and ROCK in SDE simulations, the equations and parameters determined by Kamps et al. (2020) were utilized and only the respective Myosin concentration or activation was adjusted. The ODEs are given in the introduction section of this thesis.

Here, the previously published SDE system (Kamps et al., 2020), already described in the introduction (section 1.3.5) was extended by incorporating an additional Michaelis-Menten term with a rate constant, $k_7$, and a Michaelis constant, $K_{m7}$, representing the Rho-independent activation of Myosin by CA-ROCK:

$$dG = (k_3(G_T - G) \cdot R - k_4 G \cdot M)dt \quad \text{equation (1)}$$

$$dR = \left(\frac{k_1 G \cdot (R_T - R)}{K_{m1} + (R_T - R)} - \frac{k_2 \cdot R}{K_{m2} + R}\right) dt \quad \text{equation (2)}$$

$$dM = \left(\frac{k_5 R \cdot (M_T - M)}{K_{m5} + (M_T - M)} - \frac{k_6 \cdot M}{K_{m6} + M} + \frac{k_7 \cdot M}{K_{m7} + M}\right) dt + \sigma \cdot dW \quad \text{equation (4)}$$

$$with: dW = r \cdot \sqrt{dt}$$

The total concentration of GEF-H1, Rho, and Myosin are assumed to be constant over time and are represented by $G_T$, $R_T$, and $M_T$, respectively. The rate constants are represented by $k_1$-$k_7$, while the Michaelis constants are represented by $K_{m1}$, $K_{m2}$, $K_{m5}$, $K_{m6}$, and $K_{m7}$. Finally, σ represents the level of Gaussian noise.

In the current study, the already published parameters to simulate the unperturbed states of this system were utilized. This included increasing the total GEF-H1 concentration to $G_T$=0.3, the absence of CA-ROCK1 with $k_7$=0, and the level of gaussian noise was set to σ=0.001.

The over-activation of Myosin by CA-ROCK1 was achieved by increasing the activation rate constant, $k_7$, of CA-ROCK1.

## 7.9 Acute uncaging of CouEpo

Ptk1 cells that stably express GFP-tubulin were prepared as described in 7.2.3.3. Prior to imaging, the cells were treated with 100nM of CouEpo or an equivalent volume of dimethyl sulfoxide (DMSO) as a control. Imaging started between 10 minutes and 2 hours after the compound was added.

The TIRF-MITICO illumination combiner was set to FRAP mode and used to focus the 405 nm CellR diode laser (20 % laser power) into a single spot for the photoactivation of CouEpo. Cells were imaged first using TIRF illumination for 30 frames over 5 minutes. Then, 110 frames were captured with photouncaging pulses every 100 seconds. The photoactivation spot location was chosen at the cell edge prior to imaging onset.

## 7.10 Data analysis

The imaging data were analyzed using MATLAB R2022b and ImageJ 1.54p with Java 21.0.7 (64-bit or 86-bit) (http://imagej.nih.gov/ij/). GraphPad Prism 10 was used for statistical analysis

and graph generation. All figures were prepared with Adobe Illustrator version 29.6.1 (64-bit). All image analysis steps were performed using custom ImageJ macros.

### 7.10.1 Preparation of single cell regions for image analysis

In order to avoid mistakes in data handling, scripts were written in ImageJ (Java) that represent an automated analysis pipeline for consistent assignment and sorting of imaging data.

The scripts were all constructed in a similar manner:

1. The microscope folder, which contains subfolders for each run, is selected. The script itself traverses all subfolders.
2. Each .vsi file (microscope file) is opened and saved as a .tif file for subsequent image analysis.
3. Subsequently, the various .tif files are organized into folders that comprise a single field of view. To do so, a new folder must be selected in the same directory as the microscope folder. Within this folder, the new field of view folders are created automatically, into which the aforementioned files are copied. The files are renamed for further processing in the order of acquisition.
4. In the context of light perturbation protocols, distinct stacks from the microscope are recorded for a single cell. These stacks were now concatenated into a single stack. It should be noted that this step is not performed for protocols without light-based perturbations.
5. The final general step entails the stabilization of the (concatenated) stacks.

Subsequently, the files are ready for examination, sorted into meaningful folders and accessible as stabilized and concatenated image stacks. This procedure is undertaken to ascertain the efficacy of the stabilization and concatenation processes. In instances where the initial stabilization proved to be unsatisfactory, manual corrections were implemented.

All analysis scripts are available on request.

### 7.10.2 Cell Contraction Network Pulse analysis

Scripts for the analysis of pulsatile dynamics of the cell contraction signaling network were published previously (Graessl et al., 2017). Changes to the image preparation for analysis and the implementation of analyses in different channels were implemented in this thesis. Image

sequences were recorded at a frame rate of 7.5 or 15 frames/minute. Briefly, ImageJ was used to isolate individual cells via a custom-made script. Rescaling 10x10 pixel areas to single pixels in image stacks was conducted to reduce noise. The subsequent thresholding process was facilitated by the ImageJ Threshold adjuster, accessible through the *Image > Adjust > Threshold* menu option. Subsequently, the cells were masked and corrected for background intensity. For comparative analysis of network dynamics between two distinct channels, the masking process was executed within channel 1, and subsequently, this mask was applied on channel 2.

When the image series was captured at a frame rate of 15 frames/minute, a walking average of 7 was employed, while a frame rate of 7.5 frames/minute was analyzed with a walking average of 4.

### 7.10.3 Temporal Cross-correlation analysis of Pulses

For the cross-correlation analysis of different proteins, the prepared channels were selected after the thresholding process for cell contraction network pulse analysis in section 7.10.2.

A script that automated the sorting of the two channels under investigation, including a mask image, into separate folders for further analysis in Matlab was provided by Suchet Nanda. Utilizing custom Matlab scripts (Graessl et al., 2017), the Pearson cross-correlation coefficient between the two time-shifted corresponding images was calculated pixel-wise.

### 7.10.4 Quantification of MAP perturbation and response kinetics

For the analysis, a custom-made ImageJ script was developed based on the analysis steps in Kamps et al. (2020). Image sequences were recorded at a frame rate of 6 frames/min.

### 7.10.5 Quantification of CA-MAP

Given that the CA-MAP method was utilized to induce and measure disturbances in the cell contraction network dynamics, two distinct analyses were conducted on the recorded cells.

#### *7.10.5.1 Quantification of perturbation and response kinetics*

As for MAP analysis, the perturbation and response strength of the light perturbation were subjected to quantification. In this experiment, the fluorescence differences within the entire cell attachment area were measured.

Image sequences were recorded at a frame rate of 7.5 frames/min. The utilization of ImageJ entailed the isolation of individual cells from the aforementioned images, already concatenated, executed through the implementation of a custom-made script. The subsequent thresholding process was facilitated by the ImageJ Threshold adjuster, accessible through the *Image > Adjust > Threshold* menu option or automatically determined by the Threshold adjuster. Subsequently, the cells were masked. Next, the fluorescence intensity within the entire generated mask was measured over time and averaged for each time point within the perturbation as well as the response channel stacks. The measurements were saved and normalized as described for MAP quantification in section 7.10.4.

#### *7.10.5.2 Cell Contraction Network Pulse analysis*

Subsequent to a reduction in pixel size and the implementation of a thresholding strategy on the cells the stacks were divided into before and after light-induced recruitment of the protein of interest to the plasma membrane and the cell contraction network analysis, section 7.10.2, was performed on the individual stacks.

### 7.10.6 Cell Profiler analysis of phalloidin staining

For the morphological analysis of cytoskeletal organization based on phalloidin staining, the "Human Cells" pipeline example from cell profiler served as a starting point. DAPI staining was utilized to identify the location of cell nuclei which served as primary objects, and phalloidin staining was employed to select whole cells as secondary objects, and cytoplasmic regions were obtained by subtracting the nuclei regions. The morphometric measurements were conducted in the phalloidin channel. Subsequently, only cells that express ROCK1 constructs were included in the analysis, based on a threshold for the corresponding total fluorescence intensity in the corresponding channel.

## 7.11 Figure and movie preparation

All figures and movies were prepared using ImageJ. ImageJ tools were used to add time stamps and scale bars. Kymographs were created using the ImageJ plugin KymographBuilder (https://imagej.net/plugins/kymograph-builder).

## 7.12 AI-use in this Thesis

This thesis was grammatically and linguistically corrected using the AI-powered writing tool DeepL Write (https://www.deepl.com/en/write). No paragraphs were generated using AI.

In addition to this, ChatGPT (https://chatgpt.com/) was used to generate python-based code to simulate signal network topology outputs for Figure 1.

# 8 Materials

## 8.1 Consumables and instruments

*Table 8: Consumables and instruments used for cell culture and molecular biology.*

| Instrument/Equipment | Manufacturer |
|---|---|
| "Vortex Genie 2" touch mixer | Scientific Industries |
| 8-well LabTek® chambers No. 1.0 | ThermoFischer Scientific |
| Agarose gel electrophoresis system | Bio-rad |
| BioRad Power Pac 300 | Bio-Rad Laboratories, Inc. |
| Cell culture dishes (35/60/100 mm) | Sarstedt |
| CellXpert Cell Culture Incubator C170i | Eppendorf |
| Centrifuge 5410R | Eppendorf |
| Centrifuge 5415R | Eppendorf |
| Centrifuge tubes (15ml/50ml) | Sarstedt |
| Microwave | Sharp |
| Mr. Frosty® Cryo 1°C freezing chamber | Thermo scientific |
| NALGENEÔ Cryo 1°C freezing chamber | Thermofisher Scientific |
| Nanodrop ND-2000 | Thermofischer Scientific |
| NUAIREÔ class II biological safety cabinet | Integra Biosciences |
| Parafilm® | Bemis |
| Purelab flex, Water purification system | Veolia Water |
| Research plus pipettes | Eppendorf |
| SafeSeal microfuge tubes, 2 ml, 1.5ml, 0.5ml, 0.1ml | Sarstedt |
| safety cabinet | Integra Biosciences |
| Sarstedt serological pipettes | Sarstedt |
| Serological pipettes (5, 10, 25, 50, 100 ml) | Sarstedt |
| Thermocycler, Mastercycler 5341 | Eppendorf |
| Thermocycler, Mastercycler personal | Eppendorf |
| Thermocycler, SimpliAmp | Thermofisher Scientific |

| | |
|---|---|
| Thermomixer compact | Eppendorf |
| TIRF-Microscope see specific table | |
| UVP GelSolo, M-20V Geldokumentationssystem | analytikjena |
| Vacusafe comfort Vacuum pump | IBS Integra Bioscience |
| Water bath | Kottermann |

*Table 9: Setup (Total Internal Reflection Fluorescence (TIRF)) Microscope.*

| Description | Model | Manufacturer |
|---|---|---|
| 405 nm Laser | CellR diode laser (100 mW) | Olympus |
| 445 nm Laser | CellR diode laser (200 mW) | Olympus |
| 488 nm Laser | 400 mW Agron ion Laser, 543-A-A03 | Melles Griot |
| 514 nm Laser | OBIS diode laser (150 mW) | Coherent, Inc. |
| 561 nm Laser | CellR diode laser (100 mW) | Olympus |
| Camera | EMCCD C9100-13 | Hamamatsu |
| Emission filters | HC 520/35, HC 629/53 | AHF Analysetechnik |
| Fluorescent lamp | Lumencor light Engine S/N 20192 (SpectraX-LCR-6N-B10) | Lumencor |
| Microscope | IX-81-3 | Olympus |
| Quadruple bandpass dichroic mirror | U-M3TIR405/445/541/561 | Olympus |
| TIRF Illumination Combiner | cellTIRF MITICO-4L | Olympus |
| TIRF objective | UPlanAPO 60x/1.50-Oil HR TIRF | Olympus |
| Widefield objective | UPlanAPO 20x/0.80 | Olympus |

*Table 10: Software used for cell culture, molecular biology, analysis, figure preparation, and writing.*

| Software | Version/Source | Used for |
|---|---|---|
| ChimeraX | 1.10 | Visualization of Alphafold predictions and models from Ingrid Vetter |
| Prism8 | 8.0.1 (244) | Plotting, Statistical Analysis |
| Prism10 | 10.4.1 (627) | Plotting, Statistical Analysis |
| MatLab | R2022b | Correlation analysis, SDE Simulations |
| Cell Sense Dimension | 3.2 (Build 23706) | Software TIRF microscope |
| Coherent connection | 4.0.1.2 | Connection Software for YFP laser TIRF microscope |
| ImageJ | 2.9.0, Java 1.8.0_172 | Image Analysis and preparation of example images and movies |
| Ape | 2.0.70.0 | |
| Snapgene | 6.2.2 | Edit plasmid maps |
| Vision Works LS Analysis Software | 10.2.21302.8427 | Software GelDoc for agarose gel imagig |
| Adobe Illustrator | 29.6.1 (64bit) | Preparation Figures and Illustrations |
| PowerPoint Microsoft Office 365 | Office16 | Preparation Presentations and figures |
| Word Microsoft Office 365 | Office16 | Writing Thesis |
| Excel Microsoft Office 365 | Office16 | Calculations for image analysis, transfections, transformations |
| NEBuilder | New England Biolabs | Planning Gibson Assembly reactions |
| Image Stabilizer and log applier | Schneider et al., 2012 | Cell movie stabilization |
| KymographBuilder | Hadrien Mary | Generation of cell kymographs |

| | | |
|---|---|---|
| Clustal 2.1 multiple sequence alignment | https://www.ebi.ac.uk/jdispatcher/msa/clustalo?stype=protein | Amino acid sequence alignment |
| BioRender | https://www.biorender.com/ | Visualization Workflow functionalized Molecular Activity Painting |
| Citavi | 7.0, Swiss Academic Software GmbH | Citation |
| DeepL Write | https://www.deepl.com/en/write | Grammar and linguistic correction text |
| Nanodrop 200 | 1.6.198, Thermo Fischer Scientific Inc. | Measuring DNA concentrations |

## 8.2 Chemicals, Media and Enzymes

*Table 11: Chemicals and buffers used for cell culture and molecular biology.*

| Chemical | Manufacturer | Cat.no. |
|---|---|---|
| 100 bp DNA Ladder | New England Biolabs | N3231S |
| 10x Buffer for KOD Hot Start DNA Polymerase | Novagen | 71155 |
| 10x Buffer T4 DNA Ligase with 10 mM ATP | New England Biolabs | B0202A |
| 1kb+ DNA Ladder | New England Biolabs | N3200S |
| 25 mM MgSO4 for KOD Polymerase | Novagen | 71156 |
| Agarose Broad Range | Roth | T846.3 |
| Ampicillin Natriumsalz | Roth | K029.1 |
| Carbenicillin Dinatriumsalz | Roth | 6344.2 |
| Collagen | Sigma Aldrich | C8919 |
| Cou-Epothilione | Lab Thorn-Seshold | - |
| CutSmart Buffer | New England Biolabs | B7204S |
| DAPI/Hoechst | Sigma Aldrich | 33342 |
| Deoxynucleotide (dNTP) Solution Mix | New England Biolabs | N0447S |
| DMEM (1x) + GlutaMAX^TM-I | gibco | 31966-021 |

| | | |
|---|---|---|
| DMEM (w/o phenol red) | PAN Biotech | P04-01163 |
| DMSO anhydrous | Thermo Fisher | D12345 |
| DPBS | PAN Biotech | P04-36500 |
| EDTA | GERBU | 10.341.000 |
| Enzyme Free Cell Dissociation Solution | EMD Millipore Corp. | S-014-B |
| Ethanol | Fisher Chemicals | E/0650DF/15 |
| Ethidiumbromidlösung 1% | Roth | 2218.2 |
| EZ-Link Sulfo-NHS-Biotin | Thermo Scientific | 21217 |
| Fetal Bovine Serum (FBS) | Gibco | A5256701 (Lot: 2453039) |
| Formaldehydlösung 35% | Roth | 4980.1 |
| Gel Loading Dye Purple | New England Biolabs | B7024A |
| Geneticindisulfat (G480)-Lösung | Roth | CP11.2 |
| Glycerol | Sigma Life Science | G2025-500ML |
| IMMOIL-F30CC | Olympus | N5218700 |
| Isopropanol | Roth | |
| Kanamycinsulfat | Roth | T832.1 |
| LB-Agar (Lennox) | Roth | X965.3 |
| LB-Medium (Lennox) | Roth | X964.3 |
| L-Glutamine | PAN Biotech | P04-80100 |
| Lipofectamine 2000 | invitrogen | 11668-019 |
| MEM NEAA (100x) | PAN Biotech | P08-32100 |
| Nocodazole | Sigma-Aldrich | M1404 |
| Nuclease-free Water | Ambion | AM9932 |
| Nvoc-TMP-Cl photocaged chemical dimerizer | Chen et al., 2017 | - |
| Opt-iMEM | Gibco | 11058-021 |
| Penicillin/ Streptomycin (P/S) | PAN Biotech | P06-07100 |
| Phalloidin-Atto 488 | Sigma-Aldrich | 49409-10NMOL |
| Poly-L-lysine-hydrobromide | Sigma-Aldrich | P1274-100MG |
| Q5 High Fidelity Polymerase Buffer | New England Biolabs | B9028A |
| Q5 High GC Enhancer | New England Biolabs | B9028A |

| | | |
|---|---|---|
| SLF-TMP | Lab Yaowen Wu | - |
| Sodium Pyruvate | PAN Biotech | P04-43100 |
| Streptavidin lyophil. Salt-free | Serva | 35490.01 |
| Streptavidin-Cy3 | Sigma Life Technologies | S6402-1ML |
| TMP | Lab Yaowen Wu | - |
| Trypsin/EDTA (0.05%/0.02%) | PAN Biotech | P10-02355P |

*Table 12: Used commercial kits for molecular biology.*

| Kit | Manufacturer | Cat.no. |
|---|---|---|
| Gateway lR Clonase II Enzyme Mix | invitrogen | 11791-020 |
| NEBuilder HiFi DNA Assemby Cloning Kit | NEB | E5520 |
| Plasmid Plus Maxi Kit | Quiagen | 12963 |
| QIAprep Spin Miniprep Kit | Quiagen | 27106 |
| QIAquick Gel Extraction kit | Quiagen | 28706 |
| QIAquick PCR Purification Kit | Quiagen | 28106 |

*Table 13: Enzymes used for molecular biology.*

| Enzyme | Supplier | Cat.no. |
|---|---|---|
| T4 DNA ligase | New England Biolabs | M0202S |
| T5 Exonuclease | New England Biolabs | M0663S |
| Phusion DNA polymerase | New England Biolabs | M0273S |
| Taq DNA ligase | New England Biolabs | M0208L |
| Restriction enzymes and associated buffers | New England Biolabs | - |
| KOD Hot Start DNA Polymerase | Novagen | 71316 |
| Q5 HF DNA Polymerase | New England Biolabs | M0491L |
| Phusion HF DNA Polymerase | New England Biolabs | M0530L |
| Taq DNA Polymerase | New England Biolabs | M0273S |
| Dpn1 | New England Biolabs | R0176S |

*Table 14: Media composition and Master Mix recipes.*

| Name | Composition |
|---|---|
| 10 mM EDTA | DPBS<br>EDTA<br>pH7.4 |
| Agar | LB Medium<br>1.5% Agar |
| Gibson Master mix | 100 µL 5x Isothermal Buffer<br>2 µL T5 Exonuclease (2 U/µL)<br>6.25 µL Phusion DNA Polymerase (2 U/µL)<br>50 µL Taq DNA Ligase (40 U/µL)<br>up to 375 µL with nfH2O |
| Imaging medium | DMEM (w/o Phenol Red)<br>10 % FBS |
| LB | 5 g/L Yeast-Extract<br>10 g/L NaCl<br>10 g/L Tryptone<br>ddH2O (pH 7.4) |
| LB agar plate (premixed) + Carbenicillin | Carbenicillin 100 mg/L |
| LB agar plate (premixed) + Chloramphenicol | Chloramphenicol 50 mg/mL |
| LB agar plate (premixed) + Kanamycin | Kanamycin 50 mg/L |
| LB agar plate (premixed) + Spectomycin | Spectomycin 100 mg/L |
| LB medium (premixed) + Carbenicillin | Carbenicillin 100 mg/L |
| LB medium (premixed) + Chloramphenicol | Chloramphenicol 50 mg/mL |
| LB medium (premixed) + Kanamycin | Kanamycin 50 mg/L |
| LB medium (premixed) + Spectomycin | Spectomycin 100 mg/L |

| | |
|---|---|
| Ptk1 medium | DMEM (PAN Biotech)<br>10 % FBS (gibco)<br>100 U/mL Penicillin + 100 µg/mL Streptomycin<br>2 mM L-Glutamine (PAN Biotech)<br>1 mM Sodium Pyruvate (PAN Biotech)<br>100 ng/mL G418 (Sigma) |
| SOC medium (in house, media facility MPI Dortmund) | 2 % Bactotryptone<br>0.5 % Yeast-Extract<br>10 mM NaCl<br>2.5 mM KCl<br>10 mM MgCl2<br>20 mM Glucose |
| TAE buffer | 40 mM Tris-Acetate |
| U2OS medium | DMEM with GlutaMAX (gibco)<br>10 % FBS (gibco)<br>100 U/mL Penicillin + 100 µg/mL Streptomycin |

## 8.3 Cell lines

*Table 15: Mammalian cell lines used for microscopic experiments.*

| **Name** | **Organism** | **Tissue** | **Generation time** | **Morphology** | **ATTCC No.** |
|---|---|---|---|---|---|
| U2OS | Human | Bone, female osteosarcoma cells | 24 h | Epithelial | HTB-96 |
| Ptk1 GFP-Tubulin | *Potorous tridactylus*, potoroo | kidney, female | 24 h | Epithelial | CRL-6493 |

*Table 16: Competent cells used for amplification of newly designed plasmid DNAs.*

| Name | competency | Supplier |
|---|---|---|
| Top 10 *F– mcrA Δ(mrr-hsdRMS-mcrBC) Φ80lacZΔ M15 Δ lacX74 recA1 araD139Δ(ara-leu) 7697 galU galK rpsL (StrR)endA1 nupG Λ-* | chemical competent | Invitrogen |
| Top 10 *F– mcrA Δ(mrr-hsdRMS-mcrBC) Φ80lacZΔ M15 Δ lacX74 recA1 araD139Δ(ara-leu) 7697 galU galK rpsL (StrR)endA1 nupG Λ-* | electrocompetent | Invitrogen |
| XL 10 Gold *TetR Δ(mcrA)183 Δ(mcrCB-hsdSMR mrr) 173 endA1 supE44 thi-1 recA1gyrA96 relA1 lac Hte [F' proAB lacIqZ ΔM15 Tn10(TetR) Amy CamR]* | chemical competent | Stratagene |
| XL 10 Gold *TetR Δ(mcrA)183 Δ(mcrCB-hsdSMR mrr) 173 endA1 supE44 thi-1 recA1gyrA96 relA1 lac Hte [F' proAB lacIqZ ΔM15 Tn10(TetR) Amy CamR]* | electrocompetent | Stratagene |
| GH371 *F – mcrA Δ(mrrhsdRMSmcrBC)φ80lacZΔM15 Δ(lac)X74 recA1 endA1 araD139 Δ(araAleu)7697 galU galK rpsL(Strr ) nupG fhuA::IS2 upp –* | chemical competent | obtained from J. W. Chin |

## 8.4 DNA Plasmids and Oligos

*Table 17: DNA Plasmids from other sources.*

| Plasmid No. | Name | source |
|---|---|---|
| 163 | delCMV-mCitrine | Nanda et al. 2023 |
| 229 | delCMV-mCherry-Rhotekin-GBD | Graessl et at., 2017 |
| 257 | delCMV-mCitrine-RBD | Kamps et al. 2020 |
| 326 | EGFP-GEF-H1_C53R | Krendel et al. 2002 |
| 331 | mTurquoise2-NES-eDHFR-RhoADCAAX | Kamps et al., 2020 |

| | | |
|---|---|---|
| 338 | Dimerizer-PARC-CCL-mcitrine-Halotag | Chen et al. 2017 |
| 385 | mTurquoise2-NES-Linker-eDHFR-Linker-GEF-H1 (C53R) | Kamps et al. 2020 |
| 388 | mTurquoise2-NES-Linker-eDHFR | Dominic Kamps |
| 748 | mCherry-NMHC2a (human) | Kowalczyk et al. 2022 |
| 749 | mCitrine-NMHCIIA | Dominic Kamps |
| 847 | R777-E283 Hs.ROCK1 | Esposito lab |
| 860 | pDEST-CMV-N-mCherry | Agrotis et al., 2019 |
| 907 | mApple-GEF-H1 C53R | Nalbant lab |
| 913 | R777-E285 Hs.ROCK2 | Esposito lab |
| 915 | CMV-EGFP-RhoE | Addgene #23229 |
| 956 | mTurquoise2-NES-eDHFR-RhoA Q63L DCAAX | Kamps et al., 2020 |

The following table presents a comprehensive list of all the plasmids that were examined in this study. Plasmids that proved ineffective and did not yield the anticipated results are not enumerated in this thesis. Individuals seeking further information regarding these plasmids are advised to contact Leif Dehmelt.

*Table 18: Plasmids generated for this thesis.*

| Plasmid No. | Name | parental plasmid 1 no. | parental plasmid 2 no. | fwd no. | rev no. | Method |
|---|---|---|---|---|---|---|
| 905 | CMV-mTur2-ROCKID4-eDHFR | 388 | 847 | 1125 | 1126 | 1-fragment Gibson, digest 388 XhoI |
| 912 | CMV-mCherry-attB1-ROCK1-attB2 | 860 | 847 | | | Gateway Cloning |
| 921 | CMV-mCherry-attB1-ROCKI S288R N292D-attB2 | 912 | | 1155 | 1156 | Mutagenesis |
| 922 | CMV-mCherry-attB1-ROCKID4-attB2 | 912 | | 1146 | 1147 | 1-fragment Gibson |

| | | | | | | |
|---|---|---|---|---|---|---|
| 923 | CMV-mCherry-attB1-ROCKID4DRhoE-attB2 | 921 | | 1146 | 1147 | 1-fragment Gibson |
| 929 | CMV-mCitrine-GEF-H1 C53R | 326 | 163 | 1168 | 1169 | 2-fragment Gibson, digest 326 KpnI-HF + EcoRI-HF |
| 930 | CMV-mCherry-attB1-ROCK2-attB2 | 860 | 912 | | | Gateway Cloning |
| 931 | pTriEX-mCherry-Zdk1-ROCKID4 | 358 | 905 | 1128 | 1132 | 2-fragment Gibson, digest 358 KpnI+NotI |
| 937 | CMV-mCherry-attB1-PHROCK1-attB2 | 912 | | 1152 | 1151 | 1-fragment Gibson |
| 938 | CMV-mCherry-attB1-PHGBDROCK1-attB2 | 912 | | 1150 | 1151 | 1-fragment Gibson |
| 942 | CMV-mCherry-attB1-3GS-E-mPHC1ROCK1-attB2 | 912 | | 1176 | 1151 | 1-fragment Gibson |
| 944 | CMV-mCherry-attB1-3GS-mPHC1ROCK1-attB2 | 912 | | 1175 | 1151 | 1-fragment Gibson |
| 947 | mPH(N)-3xGS-PH(C)ROCK1 | 944 | | 1184 | 1183 | 1-fragment Gibson |
| 949 | CMV-mCherry-mC1ROCK1 | | | | | 2-fragment Gibson |
| | Backbone | 944 | | 1178 | 1179 | |
| | Insert | | 944 | 1180 | 1181 | |
| 950 | CMV-mCherry-mPHC1ROCK1-A1292R | | | | | 2-fragment Gibson |
| | Backbone | 942 | | 1186 | 1188 | |
| | Insert | | GeneStrand B | 1189 | 1191 | |

| | | | | | | |
|---|---|---|---|---|---|---|
| 952 | CMV-mCherry-mPHC1ROCK1-F1174A-L1199A-E1203K-A1292R | | | | | 3-fragment Gibson |
| | Backbone | 942 | | 1186 | 1187 | |
| | Insert 1 | | GeneStrand B | 1189 | 1191 | |
| | Insert 2 | | GeneStrand A | 1190 | 1188 | |
| 955 | CMV-mCherry-mPHC1ROCK1-F1174A-L1199A-E1203K | | | | | 2-fragment Gibson |
| | Backbone | 942 | | 1189 | 1187 | |
| | Insert | | GeneStrand A | 1190 | 1188 | |
| 971 | mCherry-GBD1ROCK1(920-1021) | | | | | 2-fragment Gibson |
| | Backbone | 942 | | 1201 | 1179 | |
| | Insert | | 912 | 1203 | 1204 | |
| 973 | CMV-mTur2-RhoCQ63LΔCAAX-eDHFR | | | | | 2-fragment Gibson |
| | Backbone | 956 | | 1223 | 1224 | |
| | Insert | | 874 | 1220 | 1221 | |
| 974 | CMV-mTur2-ROCK1-eDHFR | 912 | 388 | 1207 | 1208 | 2-fragment Gibson, digest 388 XhoI |
| 975 | CMV-mTur2-ROCK1DPHDRnd3-eDHFR.ape | 921 | 388 | 1125 | 1200 | 1-fragment Gibson |
| 984 | mTur2-eDHFR-RhoACAAX | 331 | | 1237 | 1238 | 1-fragment Gibson |
| 985 | CMV-mCherry-ROCK1-F1174A-L1199A-E1203K-A1292R | | | | | 2-fragment Gibson |
| | Backbone | 912 | | 1245 | 1246 | |

| | | | | | | |
|---|---|---|---|---|---|---|
| | Insert | | 952 | 1247 | 1248 | |
| 986 | CMV-mTur2-ROCK1PHmut4-eDHFR | | | | | 2-fragment Gibson |
| | Backbone | 974 | | 1245 | 1246 | |
| | Insert | | 952 | 1247 | 1248 | |
| 988 | CMV-mCherry-ROCK1DPHC1 | 912 | | 1243 | 1244 | 1-fragment Gibson |
| 999 | CMV-mTur2-ROCK1ΔPHC1-eDHFR | 388 | 912 | | | Cloned by VectorBuilder |
| 1000 | mCherry-GBD1ROCK1mutRBD | 971 | | 1257 | 1258 | QuickChange |
| 1001 | CMV-mCherry-ROCKImutRBDmutCPH | 985 | | 1257 | 1258 | QuickChange |
| 1002 | CMV-mCherry-ROCK1mutRBD | 912 | | 1257 | 1258 | QuickChange |

*Table 19: Oligos used for molecular biology (generation plasmids).*

| Primer no. | Primer sequence |
|---|---|
| 1125 | gatctggactcgtacaagatatcatccggttctggaagtggatcgactggggacagttttg |
| 1126 | gccgcaatcagactgatcatagctccacttccagaaccggatagatttcttctttgatttccctcttc |
| 1128 | acaaggacgacgacgacaaaaccggttccggttctggaagtggatcgactggggacagttttg |
| 1132 | tgtgcggccgcaagcttttagctagcttatagatttcttctttgatttccctcttc |
| 1146 | gaaatcaaagaagaaatctaTAATCAACTTTCTTGTACAAAGTG |
| 1147 | TAGATTTCTTCTTTGATTTCCC |
| 1150 | tgtacaaaaaagttggcaccatgctaaccaaagatattgaaatattaag |
| 1151 | ggtgccaacttttttgtac |
| 1152 | tgtacaaaaaagttggcaccaaaattgatagaaagaaagctaatac |
| 1155 | tatggACCATAAAAATTCACTTACC |
| 1156 | attttcCTGTAAGTTCCAACCAAAG |
| 1168 | ctcgtttagtgaaccgtcagaattcgccaccatggtgagcaagggcgag |
| 1169 | ttcgatccgagacatggtacccttgtacagctcgtccatgc |
| 1175 | tgtacaaaaaagttggcacctccggttctggaagtggaTCAAGAATTGAAGGTTGG |
| 1176 | tgtacaaaaaagttggcacctccggttctggaagtggaGAGTCAAGAATTGAAGGTTG |

| | |
|---|---|
| 1178 | agaaagaggacttaatttgttaatcaactttcttgtacaaagtggtg |
| 1179 | tccacttccagaaccggag |
| 1180 | cctccggttctggaagtggacatgagtttattcctacactc |
| 1181 | acaaattaagtcctctttcttatc |
| 1183 | gcctttgtgattttggaaattag |
| 1184 | atttccaaaatcacaaaggcccatgtaaagtaagttatgatg |
| 1186 | tctggaaaaactagttaatcaac |
| 1187 | ccaaccttcaattcttgac |
| 1188 | ctagggcagggggtggcttaaaaacatg |
| 1189 | taagccacccccctgccctagagtgtcgaag |
| 1190 | agtcaagaattgaaggttggctttcagtaccaaatagagg |
| 1191 | gattaactagtttttccagatgtatttttgaccactttccgg |
| 1200 | gcaatcagactgatcatagcgttaattaaacctgaacctgatcctctggcgcgccttgggaggttaccatcagtttc |
| 1201 | tttaaaattgatagaaagaaataatcaactttcttgtacaaagtggtg |
| 1203 | cctccggttctggaagtggaagcaagaaagctgcttcaag |
| 1204 | tttctttctatcaattttaaaatcttttcg |
| 1207 | ctggactcgtacaagatatcaatgtcgactggggacagttttg |
| 1208 | gcaatcagactgatcatagccgatccacttccagaaccggaactagtttttccagatgtatttttgacc |
| 1220 | aattgagttaGCCCCTCCGACGCTTGTT |
| 1221 | aattgagttaTTAGAGAATGGGACAGCC |
| 1223 | tcggaggggcTAACTCAATTGTTGTTGTTAAC |
| 1224 | ggattgcagcGGATCTAGAGGTGGATCC |
| 1237 | aaaatctggttgccttgtcttgtaactcaattgttgttgttaac |
| 1238 | caagacaaggcaaccagatttttttcttccc |
| 1243 | cctcccagagTAATCAACTTTCTTGTACAAAGTG |
| 1244 | aagttgattaCTCTGGGAGGTTACCATC |
| 1245 | aacatcacgaAGAGATATGCTGCTGTTAG |
| 1246 | taacgtgagcCAGTTTATCTATGTCCAATACC |
| 1247 | agataaactgGCTCACGTTAGACCTGTAAC |
| 1248 | gcatatctctTCGTGATGTTACATCATAACTTAC |
| 1257 | cccttaaaacacaggctgttaccacattggc |
| 1257 | tcgattcattatttctgccaatgtggtaacagcct |

*Table 20: GeneStrands used for generation of PH mutant plasmids.*

| GeneStrand | Sequence |
|---|---|
| | AGTCAAGAAT TGAAGGTTGG CTTTCAGTAC CAAATAGAGG |
| | AAATATCAAA CGATATGGCT GGAAGAAACA GTATGTTGTG |
| | GTAAGCAGCA AAAAAATTTT GTTCTATAAT GACGAACAAG |
| | ATAAGGAGCA ATCCAATCCA TCTATGGTAT TGGACATAGA |
| | TAAACTGGCT CACGTTAGAC CTGTAACCCA AGGAGATGTG |
| | TATAGAGCTG AAACTGAAGA AATTCCTAAA ATATTCCAGA |
| | TAGCATATGC AAATAAAGGT GAATGTAGAA AAGATGTAGA |
| | GATGGAACCA GTACAACAAG CTGAAAAAAC TAATTTCCAA |
| | AATCACAAAG GCCATGAGTT TATTCCTACA CTCTACCACT |
| | TTCCTGCCAA TTGTGATGCC TGTGCCAAAC CTCTCTGGCA |
| A | TGTTTTTAAG CCACCCCCTG CCCTAG |
| | TAAGCCACCC CCTGCCCTAG AGTGTCGAAG ATGCCATGTT |
| | AAGTGCCACA GAGATCACTT AGATAAGAAA GAGGACTTAA |
| | TTTGTCCATG TAAAGTAAGT TATGATGTAA CATCACGAAG |
| | AGATATGCTG CTGTTAGCAT GTTCTCAGGA TGAACAAAAA |
| | AAATGGGTAA CTCATTTAGT AAAGAAAATC CCTAAGAATC |
| | CACCATCTGG TTTTGTTCGT GCTTCCCCTC GAACGCTTTC |
| | TACAAGATCC ACTGCAAATC AGTCTTTCCG GAAAGTGGTC |
| B | AAAAATACAT CTGGAAAAAC TAGTTAATC |

# 9 References


Abdelghany, L., C. Sillapachaiyaporn, and B. Zhivotovsky. 2024. The concealed side of caspases: beyond a killer of cells. *Cell. Mol. Life Sci.* 81(1):474. doi:10.1007/s00018-024-05495-7.

Adelstein, R. S., T. D. Pollard, and W. M. Kuehl. 1971. Isolation and characterization of myosin and two myosin fragments from human blood platelets. *Proceedings of the National Academy of Sciences of the United States of America* 68(11):2703–2707. doi:10.1073/pnas.68.11.2703.

Aguilar-Cuenca, R., A. Juanes-García, and M. Vicente-Manzanares. 2014. Myosin II in mechanotransduction: master and commander of cell migration, morphogenesis, and cancer. *Cell. Mol. Life Sci.* 71(3):479–492. doi:10.1007/s00018-013-1439-5.

Alanko, J., M. C. Uçar, N. Canigova, J. Stopp, J. Schwarz, J. Merrin, E. Hannezo, and M. Sixt. 2023. CCR7 acts as both a sensor and a sink for CCL19 to coordinate collective leukocyte migration. *Science immunology* 8(87):eadc9584. doi:10.1126/sciimmunol.adc9584.

Altmann, K. H., G. Bold, G. Caravatti, A. Flörsheimer, V. Guagnano, and M. Wartmann. 2000. Synthesis and biological evaluation of highly potent analogues of epothilones B and D. *Bioorganic & Medicinal Chemistry Letters* 10(24):2765–2768. doi:10.1016/S0960-894X(00)00555-2.

Amano, M., K. Chihara, K. Kimura, Y. Fukata, N. Nakamura, Y. Matsuura, and K. Kaibuchi. 1997. Formation of actin stress fibers and focal adhesions enhanced by Rho-kinase. *Science* 275(5304):1308–1311. doi:10.1126/science.275.5304.1308.

Amano, M., Y. Fukata, and K. Kaibuchi. 2000. Regulation and functions of Rho-associated kinase. *Experimental cell research* 261(1):44–51. doi:10.1006/excr.2000.5046.

Amano, M., M. Ito, K. Kimura, Y. Fukata, K. Chihara, T. Nakano, Y. Matsuura, and K. Kaibuchi. 1996. Phosphorylation and activation of myosin by Rho-associated kinase (Rho-kinase). *The Journal of biological chemistry* 271(34):20246–20249. doi:10.1074/jbc.271.34.20246.

Antoku, S., T. U. Schwartz, and G. G. Gundersen. 2023. FHODs: Nuclear tethered formins for nuclear mechanotransduction. *Front. Cell Dev. Biol.* 11:1160219. doi:10.3389/fcell.2023.1160219.

Asp, P., M. Wihlborg, M. Karlén, and A.-K. O. Farrants. 2002. Expression of BRG1, a human SWI/SNF component, affects the organisation of actin filaments through the RhoA signalling pathway. *Journal of cell science* 115(Pt 13):2735–2746. https://pubmed.ncbi.nlm.nih.gov/12077364/.

Beach, J. R., K. S. Bruun, L. Shao, D. Li, Z. Swider, K. Remmert, Y. Zhang, M. A. Conti, R. S. Adelstein, N. M. Rusan, E. Betzig, and J. A. Hammer. 2017. Actin dynamics and competition for myosin monomer govern the sequential amplification of myosin filaments. *Nat Cell Biol* 19(2):85–93. doi:10.1038/ncb3463.

Beck, M., A. Schmidt, J. Malmstroem, M. Claassen, A. Ori, A. Szymborska, F. Herzog, O. Rinner, J. Ellenberg, and R. Aebersold. 2011. The quantitative proteome of a human cell line. *Mol Syst Biol* 7(1):549. doi:10.1038/msb.2011.82.

Bement, W. M., M. Leda, A. M. Moe, A. M. Kita, M. E. Larson, A. E. Golding, C. Pfeuti, K.-C. Su, A. L. Miller, A. B. Goryachev, and G. von Dassow. 2015. Activator-inhibitor coupling between Rho signalling and actin assembly makes the cell cortex an excitable medium. *Nature cell biology* 17(11):1471–1483. doi:10.1038/ncb3251.

Benink, H. A., and W. M. Bement. 2005. Concentric zones of active RhoA and Cdc42 around single cell wounds. *The Journal of cell biology* 168(3):429–439. doi:10.1083/jcb.200411109.

Bieling, P., and K. Rottner. 2023. From WRC to Arp2/3: Collective molecular mechanisms of branched actin network assembly. *Current Opinion in Cell Biology* 80:102156. doi:10.1016/j.ceb.2023.102156.

Billington, N., A. Wang, J. Mao, R. S. Adelstein, and J. R. Sellers. 2013. Characterization of three full-length human nonmuscle myosin II paralogs. *Journal of Biological Chemistry* 288(46):33398–33410. doi:10.1074/jbc.M113.499848.

Blumenstein, L., and M. R. Ahmadian. 2004. Models of the cooperative mechanism for Rho effector recognition: implications for RhoA-mediated effector activation. *The Journal of biological chemistry* 279(51):53419–53426. doi:10.1074/jbc.M409551200.

Bouchet, B. P., and A. Akhmanova. 2017. Microtubules in 3D cell motility. *J Cell Sci* 130(1):39–50. doi:10.1242/jcs.189431.

Bouchet, B. P., I. Noordstra, M. van Amersfoort, E. A. Katrukha, Y.-C. Ammon, N. D. ter Hoeve, L. Hodgson, M. Dogterom, P. W. B. Derksen, and A. Akhmanova. 2016. Mesenchymal Cell Invasion Requires Cooperative Regulation of Persistent Microtubule Growth by SLAIN2 and CLASP1. *Developmental Cell* 39(6):708–723. doi:10.1016/j.devcel.2016.11.009.

Boudreau, C., T.-L. E. Wee, Y.-R. S. Duh, M. P. Couto, K. H. Ardakani, and C. M. Brown. 2016. Excitation Light Dose Engineering to Reduce Photo-bleaching and Photo-toxicity. *Sci Rep* 6(1):30892. doi:10.1038/srep30892.

Brangwynne, C. P., F. C. MacKintosh, S. Kumar, N. A. Geisse, J. Talbot, L. Mahadevan, K. K. Parker, D. E. Ingber, and D. A. Weitz. 2006. Microtubules can bear enhanced compressive loads in living cells because of lateral reinforcement. *The Journal of cell biology* 173(5):733–741. doi:10.1083/jcb.200601060.

Bray, D. 1995. Protein molecules as computational elements in living cells. *Nature* 376(6538):307–312. doi:10.1038/376307a0.

Buchsbaum, R. J. 2007. Rho activation at a glance. *J Cell Sci* 120(Pt 7):1149–1152. doi:10.1242/jcs.03428.

Cappell, S. D., M. Chung, A. Jaimovich, S. L. Spencer, and T. Meyer. 2016. Irreversible APC(Cdh1) Inactivation Underlies the Point of No Return for Cell-Cycle Entry. *Cell* 166(1):167–180. doi:10.1016/j.cell.2016.05.077.

Carlier, M. F., V. Laurent, J. Santolini, R. Melki, D. Didry, G. X. Xia, Y. Hong, N. H. Chua, and D. Pantaloni. 1997. Actin depolymerizing factor (ADF/cofilin) enhances the rate of filament

turnover: implication in actin-based motility. *J Cell Biol* 136(6):1307–1322. doi:10.1083/jcb.136.6.1307.

Carlsson, L., L. E. Nyström, I. Sundkvist, F. Markey, and U. Lindberg. 1977. Actin polymerizability is influenced by profilin, a low molecular weight protein in non-muscle cells. *Journal of molecular biology* 115(3):465–483. doi:10.1016/0022-2836(77)90166-8.

Carney, D. W., J. C. Lukesh, D. M. Brody, M. M. Brütsch, and D. L. Boger. 2016. Ultrapotent vinblastines in which added molecular complexity further disrupts the target tubulin dimer-dimer interface. *Proceedings of the National Academy of Sciences of the United States of America* 113(35):9691–9698. doi:10.1073/pnas.1611405113.

Chang, Y.-C., P. Nalbant, J. Birkenfeld, Z.-F. Chang, and G. M. Bokoch. 2008. GEF-H1 couples nocodazole-induced microtubule disassembly to cell contractility via RhoA. *MBoC* 19(5):2147–2153. doi:10.1091/mbc.e07-12-1269.

Chen, W. W., M. Niepel, and P. K. Sorger. 2010. Classic and contemporary approaches to modeling biochemical reactions. *Genes Dev.* 24(17):1861–1875. doi:10.1101/gad.1945410.

Chen, X., I. Tan, C. H. Ng, C. Hall, L. Lim, and T. Leung. 2002. Characterization of RhoA-binding kinase ROKalpha implication of the Pleckstrin homology domain in ROKalpha function using region-specific antibodies. *The Journal of biological chemistry* 277(15):12680–12688. doi:10.1074/jbc.M109839200.

Chen, X., M. Venkatachalapathy, D. Kamps, S. Weigel, R. Kumar, M. Orlich, R. Garrecht, M. Hirtz, C. M. Niemeyer, Y.-W. Wu, and L. Dehmelt. 2017. "Molecular Activity Painting": Switch-like, Light-Controlled Perturbations inside Living Cells. *Angewandte Chemie (International ed. in English)* 56(21):5916–5920. doi:10.1002/anie.201611432.

Cherfils, J., and M. Zeghouf. 2013. Regulation of small GTPases by GEFs, GAPs, and GDIs. *Physiological reviews* 93(1):269–309. doi:10.1152/physrev.00003.2012.

Chugh, P., and E. K. Paluch. 2018. The actin cortex at a glance. *Journal of cell science* 131(14). doi:10.1242/jcs.186254.

Coleman, M. L., E. A. Sahai, M. Yeo, M. Bosch, A. Dewar, and M. F. Olson. 2001. Membrane blebbing during apoptosis results from caspase-mediated activation of ROCK I. *Nature cell biology* 3(4):339–345. doi:10.1038/35070009.

Cooper, G. M., editor. 2000. The Cell: A Molecular Approach. 2nd edition. Sinauer Associates.

Csikász-Nagy, A., D. Battogtokh, K. C. Chen, B. Novák, and J. J. Tyson. 2006. Analysis of a generic model of eukaryotic cell-cycle regulation. *Biophysical Journal* 90(12):4361–4379. doi:10.1529/biophysj.106.081240.

Cui, Y., F. M. Hameed, B. Yang, K. Lee, C. Q. Pan, S. Park, and M. Sheetz. 2015. Cyclic stretching of soft substrates induces spreading and growth. *Nat Commun* 6(1):6333. doi:10.1038/ncomms7333.

Dehmelt, L., P. Nalbant, W. Steffen, and S. Halpain. 2006. A microtubule-based, dynein-dependent force induces local cell protrusions: Implications for neurite initiation. *Brain cell biology* 35(1):39–56. doi:10.1007/s11068-006-9001-0.

Dogterom, M., and B. Yurke. 1997. Measurement of the Force-Velocity Relation for Growing Microtubules. *American Association for the Advancement of Science,* 10/31/1997. https://www.science.org/doi/10.1126/science.278.5339.856. Accessed 07/16/2025.

Dovas, A., and J. R. Couchman. 2005. RhoGDI: multiple functions in the regulation of Rho family GTPase activities. *The Biochemical journal* 390(Pt 1):1–9. doi:10.1042/BJ20050104.

Dujardin, D. L., L. E. Barnhart, S. A. Stehman, E. R. Gomes, G. G. Gundersen, and R. B. Vallee. 2003. A role for cytoplasmic dynein and LIS1 in directed cell movement. *The Journal of cell biology* 163(6):1205–1211. doi:10.1083/jcb.200310097.

Dunlap, J. C. 1999. Molecular bases for circadian clocks. *Cell* 96(2):271–290. doi:10.1016/s0092-8674(00)80566-8.

Dvorsky, R., L. Blumenstein, I. R. Vetter, and M. R. Ahmadian. 2004. Structural insights into the interaction of ROCKI with the switch regions of RhoA. *The Journal of biological chemistry* 279(8):7098–7104. doi:10.1074/jbc.M311911200.

Elowitz, M. B., and S. Leibler. 2000. A synthetic oscillatory network of transcriptional regulators. *Nature* 403(6767):335–338. doi:10.1038/35002125.

Etienne-Manneville, S. 2013. Microtubules in cell migration. *Annual Review of Cell and Developmental Biology* 29:471–499. doi:10.1146/annurev-cellbio-101011-155711.

Fanale, D., G. Bronte, F. Passiglia, V. Calò, M. Castiglia, F. Di Piazza, N. Barraco, A. Cangemi, M. T. Catarella, L. Insalaco, A. Listì, R. Maragliano, D. Massihnia, A. Perez, F. Toia, G. Cicero, and V. Bazan. 2015. Stabilizing versus destabilizing the microtubules: a double-edge sword for an effective cancer treatment option? *Analytical Cellular Pathology* 2015(1):690916. doi:10.1155/2015/690916.

Ferrell, J. E. 2002. Self-perpetuating states in signal transduction: positive feedback, double-negative feedback and bistability. *Current Opinion in Cell Biology* 14(2):140–148. doi:10.1016/s0955-0674(02)00314-9.

Ferrell, J. E., and S. H. Ha. 2014. Ultrasensitivity part III: cascades, bistable switches, and oscillators. *Trends in Biochemical Sciences* 39(12):612–618. doi:10.1016/j.tibs.2014.10.002.

Ferrell, J. E., and E. M. Machleder. 1998. The Biochemical Basis of an All-or-None Cell Fate Switch in Xenopus Oocytes. *American Association for the Advancement of Science,* 8/5/1998. https://www.science.org/doi/full/10.1126/science.280.5365.895?casa_token=-JRbJ4_SLH8AAAAA%3AxL_PhCaovGRmDqftsSasT2WFGWB262yAxCa2cyB4tOasLzvQJmNZMmMmnRLngds3V4gEMXpWvu7WlA. Accessed 07/13/2025.

Fujisawa, K., A. Fujita, T. Ishizaki, Y. Saito, and S. Narumiya. 1996. Identification of the Rho-binding domain of p160ROCK, a Rho-associated coiled-coil containing protein kinase. *Journal of Biological Chemistry* 271(38):23022–23028. doi:10.1074/jbc.271.38.23022.

Gabet, A.-S., S. Coulon, A. Fricot, J. Vandekerckhove, Y. Chang, J.-A. Ribeil, L. Lordier, Y. Zermati, V. Asnafi, Z. Belaid, N. Debili, W. Vainchenker, B. Varet, O. Hermine, and G. Courtois. 2011. Caspase-activated ROCK-1 allows erythroblast terminal maturation

independently of cytokine-induced Rho signaling. *Cell death and differentiation* 18(4):678–689. doi:10.1038/cdd.2010.140.

Gao, L., J. C. M. Meiring, C. Heise, A. Rai, A. Müller-Deku, A. Akhmanova, J. Thorn-Seshold, and O. Thorn-Seshold. 2022. Photoswitchable Epothilone-Based Microtubule Stabilisers Allow GFP-Imaging-Compatible, Optical Control over the Microtubule Cytoskeleton. *Angewandte Chemie (International ed. in English)* 61(10):e202114614. doi:10.1002/anie.202114614.

Garrido-Casado, M., G. Asensio-Juárez, and M. Vicente-Manzanares. 2021. Nonmuscle Myosin II Regulation Directs Its Multiple Roles in Cell Migration and Division. *Annual Review of Cell and Developmental Biology* 37(Volume 37, 2021):285–310. doi:10.1146/annurev-cellbio-042721-105528.

Gasteier, J. E., R. Madrid, E. Krautkrämer, S. Schröder, W. Muranyi, S. Benichou, and O. T. Fackler. 2003. Activation of the Rac-binding partner FHOD1 induces actin stress fibers via a ROCK-dependent mechanism. *Journal of Biological Chemistry* 278(40):38902–38912. doi:10.1074/jbc.M306229200.

Gierse, C., J. Hanemann, and L. Dehmelt. 2025a. Non-muscle Myosin II acts as a negative feedback mediator to control cell contraction dynamics.

Gierse, C., I. R. Vetter, and L. Dehmelt. 2025b. The ROCK1 PHC1 domain interacts with active Rho to transduce cell contraction signals.

Gittes, F., B. Mickey, J. Nettleton, and J. Howard. 1993. Flexural rigidity of microtubules and actin filaments measured from thermal fluctuations in shape. *J Cell Biol* 120(4):923–934. doi:10.1083/jcb.120.4.923.

Graessl, M., J. Koch, A. Calderon, D. Kamps, S. Banerjee, T. Mazel, N. Schulze, J. K. Jungkurth, R. Patwardhan, D. Solouk, N. Hampe, B. Hoffmann, L. Dehmelt, and P. Nalbant. 2017. An excitable Rho GTPase signaling network generates dynamic subcellular contraction patterns. *The Journal of cell biology* 216(12):4271–4285. doi:10.1083/jcb.201706052.

Grecco, H. E., M. Schmick, and P. I. H. Bastiaens. 2011. Signaling from the living plasma membrane. *Cell* 144(6):897–909. doi:10.1016/j.cell.2011.01.029.

Gülcüler Balta, G. S., C. Monzel, S. Kleber, J. Beaudouin, E. Balta, T. Kaindl, S. Chen, L. Gao, M. Thiemann, C. R. Wirtz, Y. Samstag, M. Tanaka, and A. Martin-Villalba. 2019. 3D Cellular Architecture Modulates Tyrosine Kinase Activity, Thereby Switching CD95-Mediated Apoptosis to Survival. *Cell Reports* 29(8):2295-2306.e6. doi:10.1016/j.celrep.2019.10.054.

Hall, A. 1998. Rho GTPases and the actin cytoskeleton. *Science* 279(5350):509–514. doi:10.1126/science.279.5350.509.

Hanahan, D. 2022. Hallmarks of Cancer: New Dimensions. *Cancer discovery* 12(1):31–46. doi:10.1158/2159-8290.CD-21-1059.

Hodge, R. G., and A. J. Ridley. 2016. Regulating Rho GTPases and their regulators. *Nat Rev Mol Cell Biol* 17(8):496–510. doi:10.1038/nrm.2016.67.

HODGKIN, A. L., and A. F. Huxley. 1952. A quantitative description of membrane current and its application to conduction and excitation in nerve. *The Journal of Physiology* 117(4):500–544. doi:10.1113/jphysiol.1952.sp004764.

Hogenesch, J. B., and E. D. Herzog. 2011. Intracellular and intercellular processes determine robustness of the circadian clock. *FEBS Letters* 585(10):1427–1434. doi:10.1016/j.febslet.2011.04.048.

Holle, A. W., N. Govindan Kutty Devi, K. Clar, A. Fan, T. Saif, R. Kemkemer, and J. P. Spatz. 2019. Cancer Cells Invade Confined Microchannels via a Self-Directed Mesenchymal-to-Amoeboid Transition. *Nano letters* 19(4):2280–2290. doi:10.1021/acs.nanolett.8b04720.

Horwitz, R., and D. Webb. 2003. Cell migration. *Current Biology* 13(19):R756-9. doi:10.1016/j.cub.2003.09.014.

Hotulainen, P., and P. Lappalainen. 2006. Stress fibers are generated by two distinct actin assembly mechanisms in motile cells. *J Cell Biol* 173(3):383–394. doi:10.1083/jcb.200511093.

Hu, S., K. Dasbiswas, Z. Guo, Y.-H. Tee, V. Thiagarajan, P. Hersen, T.-L. Chew, S. A. Safran, R. Zaidel-Bar, and A. D. Bershadsky. 2017. Long-range self-organization of cytoskeletal myosin II filament stacks. *Nat Cell Biol* 19(2):133–141. doi:10.1038/ncb3466.

Huxley, A. F. 1974. Muscular contraction. *The Journal of Physiology* 243(1):1–43. https://pmc.ncbi.nlm.nih.gov/articles/PMC1330687/.

Ikebe, M. 2008. Regulation of the function of mammalian myosin and its conformational change. *Biochemical and biophysical research communications* 369(1):157–164. doi:10.1016/j.bbrc.2008.01.057.

Ishizaki, T., M. Maekawa, K. Fujisawa, K. Okawa, A. Iwamatsu, A. Fujita, N. Watanabe, Y. Saito, A. Kakizuka, N. Morii, and S. Narumiya. 1996. The small GTP-binding protein Rho binds to and activates a 160 kDa Ser/Thr protein kinase homologous to myotonic dystrophy kinase. *The EMBO journal* 15(8):1885–1893. https://pubmed.ncbi.nlm.nih.gov/8617235/.

Ishizaki, T., M. Naito, K. Fujisawa, M. Maekawa, N. Watanabe, Y. Saito, and S. Narumiya. 1997. p160 ROCK a Rho-associated coiled-coil forming protein kinase, works downstream of Rho and induces focal adhesions. *FEBS Letters* 404(2-3):118–124. doi:10.1016/S0014-5793(97)00107-5.

Kamps, D., and L. Dehmelt. 2017. Deblurring Signal Network Dynamics. *ACS chemical biology* 12(9):2231–2239. doi:10.1021/acschembio.7b00451.

Kamps, D., J. Koch, V. O. Juma, E. Campillo-Funollet, M. Graessl, S. Banerjee, T. Mazel, X. Chen, Y.-W. Wu, S. Portet, A. Madzvamuse, P. Nalbant, and L. Dehmelt. 2020. Optogenetic Tuning Reveals Rho Amplification-Dependent Dynamics of a Cell Contraction Signal Network. *Cell reports* 33(9):108467. doi:10.1016/j.celrep.2020.108467.

Kaverina, I., K. Rottner, and J. V. Small. 1998. Targeting, capture, and stabilization of microtubules at early focal adhesions. *J Cell Biol* 142(1):181–190. doi:10.1083/jcb.142.1.181.

Keates, R. A., and G. B. Mason. 1981. Inhibition of microtubule polymerization by the tubulin-colchicine complex: inhibition of spontaneous assembly. *Canadian journal of biochemistry* 59(5):361–370. doi:10.1139/o81-050.

Khalil, R. A., editor. 2010. Regulation of Vascular Smooth Muscle Function. Morgan & Claypool Life Sciences.

Kim, E. J. Y., E. Korotkevich, and T. Hiiragi. 2018. Coordination of Cell Polarity, Mechanics and Fate in Tissue Self-organization. *Trends in Cell Biology* 28(7):541–550. doi:10.1016/j.tcb.2018.02.008.

Kimura, K., M. Ito, M. Amano, K. Chihara, Y. Fukata, M. Nakafuku, B. Yamamori, J. Feng, T. Nakano, K. Okawa, A. Iwamatsu, and K. Kaibuchi. 1996. Regulation of myosin phosphatase by Rho and Rho-associated kinase (Rho-kinase). *Science (New York, N.Y.)* 273(5272):245–248. doi:10.1126/science.273.5272.245.

Kirschner, M., and T. Mitchison. 1986. Beyond self-assembly: from microtubules to morphogenesis. *Cell* 45(3):329–342. doi:10.1016/0092-8674(86)90318-1.

Klar, U., B. Buchmann, W. Schwede, W. Skuballa, J. Hoffmann, and R. B. Lichtner. 2006. Total Synthesis and Antitumor Activity of ZK-EPO: The First Fully Synthetic Epothilone in Clinical Development. *Angewandte Chemie* 118(47):8110–8116. doi:10.1002/ange.200602785.

Komander, D., R. Garg, P. T. C. Wan, A. J. Ridley, and D. Barford. 2008. Mechanism of multi-site phosphorylation from a ROCK-I:RhoE complex structure. *The EMBO journal* 27(23):3175–3185. doi:10.1038/emboj.2008.226.

Kowalczyk, M., D. Kamps, Y. Wu, L. Dehmelt, and P. Nalbant. 2022. Monitoring the Response of Multiple Signal Network Components to Acute Chemo-Optogenetic Perturbations in Living Cells. *Chembiochem a European journal of chemical biology* 23(4):e202100582. doi:10.1002/cbic.202100582.

Krendel, M., F. T. Zenke, and G. M. Bokoch. 2002. Nucleotide exchange factor GEF-H1 mediates cross-talk between microtubules and the actin cytoskeleton. *Nature cell biology* 4(4):294–301. doi:10.1038/ncb773.

Kühn, S., and M. Geyer. 2014. Formins as effector proteins of Rho GTPases. *Small GTPases* 5:e29513. doi:10.4161/sgtp.29513.

Lazarides, E., and K. Burridge. 1975. Alpha-actinin: immunofluorescent localization of a muscle structural protein in nonmuscle cells. *Cell* 6(3):289–298. doi:10.1016/0092-8674(75)90180-4.

Lee, C.-S., C.-K. Choi, E.-Y. Shin, M. A. Schwartz, and E.-G. Kim. 2010. Myosin II directly binds and inhibits Dbl family guanine nucleotide exchange factors: a possible link to Rho family GTPases. *The Journal of cell biology* 190(4):663–674. doi:10.1083/jcb.201003057.

Leung, T., X. Q. Chen, E. Manser, and L. Lim. 1996. The p160 RhoA-binding kinase ROK alpha is a member of a kinase family and is involved in the reorganization of the cytoskeleton. *Molecular and cellular biology* 16(10):5313–5327. doi:10.1128/MCB.16.10.5313.

Liu, P., A. Calderon, G. Konstantinidis, J. Hou, S. Voss, X. Chen, F. Li, S. Banerjee, J.-E. Hoffmann, C. Theiss, L. Dehmelt, and Y.-W. Wu. 2014. A bioorthogonal small-molecule-

switch system for controlling protein function in live cells. *Angewandte Chemie International Edition* 53(38):10049–10055. doi:10.1002/anie.201403463.

Liu, Y., B. Sun, X. Zhao, Q. Gu, Z.-Y. Liu, X.-Y. Dong, N. Che, and J. Mo. 2013. Basal caspase-3 activity promotes migration, invasion, and vasculogenic mimicry formation of melanoma cells. *Melanoma research* 23(4):243–253. doi:10.1097/CMR.0b013e3283625498.

Mangan, S., and U. Alon. 2003. Structure and function of the feed-forward loop network motif. *Proceedings of the National Academy of Sciences of the United States of America* 100(21):11980–11985. doi:10.1073/pnas.2133841100.

Martin, A. C., M. Kaschube, and E. F. Wieschaus. 2009. Pulsed contractions of an actin-myosin network drive apical constriction. *Nature* 457(7228):495–499. doi:10.1038/nature07522.

Martins, G. G., and J. Kolega. 2012. A role for microtubules in endothelial cell protrusion in three-dimensional matrices. *Biology of the cell* 104(5):271–286. doi:10.1111/boc.201100088.

Matsui, T., M. Amano, T. Yamamoto, K. Chihara, M. Nakafuku, M. Ito, T. Nakano, K. Okawa, A. Iwamatsu, and K. Kaibuchi. 1996. Rho-associated kinase, a novel serine/threonine kinase, as a putative target for small GTP binding protein Rho. *The EMBO journal* 15(9):2208–2216. doi:10.1002/j.1460-2075.1996.tb00574.x.

Matsumura, F. 2005. Regulation of myosin II during cytokinesis in higher eukaryotes. *Trends in Cell Biology* 15(7):371–377. doi:10.1016/j.tcb.2005.05.004.

Mayer, T., M. Meyer, A. Janning, A. C. Schiedel, and A. Barnekow. 1999. A mutant form of the rho protein can restore stress fibers and adhesion plaques in v-src transformed fibroblasts. *Oncogene* 18(12):2117–2128. doi:10.1038/sj.onc.1202537.

Mazel, T., A. Biesemann, M. Krejczy, J. Nowald, O. Müller, and L. Dehmelt. 2014. Direct observation of microtubule pushing by cortical dynein in living cells. *MBoC* 25(1):95–106. doi:10.1091/mbc.E13-07-0376.

Medina, F., A. M. Carter, O. Dada, S. Gutowski, J. Hadas, Z. Chen, and P. C. Sternweis. 2013. Activated RhoA is a positive feedback regulator of the Lbc family of Rho guanine nucleotide exchange factor proteins. *Journal of Biological Chemistry* 288(16):11325–11333. doi:10.1074/jbc.M113.450056.

Michaelson, D., J. Silletti, G. Murphy, P. D'Eustachio, M. Rush, and M. R. Philips. 2001. Differential localization of Rho GTPases in live cells: regulation by hypervariable regions and RhoGDI binding. *J Cell Biol* 152(1):111–126. doi:10.1083/jcb.152.1.111.

Michaud, A., M. Leda, Z. T. Swider, S. Kim, J. He, J. Landino, J. R. Valley, J. Huisken, A. B. Goryachev, G. von Dassow, and W. M. Bement. 2022. A versatile cortical pattern-forming circuit based on Rho, F-actin, Ect2, and RGA-3/4. *The Journal of cell biology* 221(8). doi:10.1083/jcb.202203017.

Michaux, J. B., F. B. Robin, W. M. McFadden, and E. M. Munro. 2018. Excitable RhoA dynamics drive pulsed contractions in the early C. elegans embryo. *J Cell Biol* 217(12):4230–4252. doi:10.1083/jcb.201806161.

Milroy, L.-G., S. Rizzo, A. Calderon, B. Ellinger, S. Erdmann, J. Mondry, P. Verveer, P. Bastiaens, H. Waldmann, L. Dehmelt, and H.-D. Arndt. 2012. Selective chemical imaging of static actin in live cells. *Journal of the American Chemical Society* 134(20):8480–8486. doi:10.1021/ja211708z.

Mitchison, T., and M. Kirschner. 1984. Dynamic instability of microtubule growth. *Nature* 312(5991):237–242. doi:10.1038/312237a0.

Mott, H. R., J. W. Carpenter, S. Zhong, S. Ghosh, R. M. Bell, and S. L. Campbell. 1996. The solution structure of the Raf-1 cysteine-rich domain: a novel ras and phospholipid binding site. *Proceedings of the National Academy of Sciences of the United States of America* 93(16):8312–8317. doi:10.1073/pnas.93.16.8312.

Müller, R. T., U. Honnert, J. Reinhard, and M. Bähler. 1997. The rat myosin myr 5 is a GTPase-activating protein for Rho in vivo: essential role of arginine 1695. *Molecular biology of the cell* 8(10):2039–2053. doi:10.1091/mbc.8.10.2039.

Müller-Deku, A., J. C. M. Meiring, K. Loy, Y. Kraus, C. Heise, R. Bingham, K. I. Jansen, X. Qu, F. Bartolini, L. C. Kapitein, A. Akhmanova, J. Ahlfeld, D. Trauner, and O. Thorn-Seshold. 2020. Photoswitchable paclitaxel-based microtubule stabilisers allow optical control over the microtubule cytoskeleton. *Nat Commun* 11(1):4640. doi:10.1038/s41467-020-18389-6.

Munjal, A., J.-M. Philippe, E. Munro, and T. Lecuit. 2015. A self-organized biomechanical network drives shape changes during tissue morphogenesis. *Nature* 524(7565):351–355. doi:10.1038/nature14603.

Murrell, M. P., and M. L. Gardel. 2012. F-actin buckling coordinates contractility and severing in a biomimetic actomyosin cortex. *Proceedings of the National Academy of Sciences of the United States of America* 109(51):20820–20825. doi:10.1073/pnas.1214753109.

Nakagawa, O., K. Fujisawa, T. Ishizaki, Y. Saito, K. Nakao, and S. Narumiya. 1996. ROCK-I and ROCK-II, two isoforms of Rho-associated coiled-coil forming protein serine/threonine kinase in mice. *FEBS Letters* 392(2):189–193. doi:10.1016/0014-5793(96)00811-3.

Nalbant, P., and L. Dehmelt. 2018. Exploratory cell dynamics: a sense of touch for cells? *Biological chemistry* 399(8):809–819. doi:10.1515/hsz-2017-0341.

Nanda, S., A. Calderon, A. Sachan, T.-T. Duong, J. Koch, X. Xin, D. Solouk-Stahlberg, Y.-W. Wu, P. Nalbant, and L. Dehmelt. 2023. Rho GTPase activity crosstalk mediated by Arhgef11 and Arhgef12 coordinates cell protrusion-retraction cycles. *Nat Commun* 14(1):8356. doi:10.1038/s41467-023-43875-y.

Newell-Litwa, K. A., M. Badoual, H. Asmussen, H. Patel, L. Whitmore, and A. R. Horwitz. 2015. ROCK1 and 2 differentially regulate actomyosin organization to drive cell and synaptic polarity. *J Cell Biol* 210(2):225–242. doi:10.1083/jcb.201504046.

Niederman, R., and T. D. Pollard. 1975. Human platelet myosin. II. In vitro assembly and structure of myosin filaments. *The Journal of cell biology* 67(1):72–92. doi:10.1083/jcb.67.1.72.

Nishikawa, M., S. R. Naganathan, F. Jülicher, and S. W. Grill. 2017. Controlling contractile instabilities in the actomyosin cortex. *eLife* 6. doi:10.7554/eLife.19595.

NOBLE, D. 1962. A modification of the Hodgkin--Huxley equations applicable to Purkinje fibre action and pace-maker potentials. *The Journal of Physiology* 160(2):317–352. doi:10.1113/jphysiol.1962.sp006849.

Novák, B., and J. J. Tyson. 2008. Design principles of biochemical oscillators. *Nat Rev Mol Cell Biol* 9(12):981–991. doi:10.1038/nrm2530.

Ojima, I., S. Chakravarty, T. Inoue, S. Lin, L. He, S. B. Horwitz, S. D. Kuduk, and S. J. Danishefsky. 1999. A common pharmacophore for cytotoxic natural products that stabilize microtubules. *Proceedings of the National Academy of Sciences of the United States of America* 96(8):4256–4261. doi:10.1073/pnas.96.8.4256.

Oosterheert, W., M. Boiero Sanders, J. Funk, D. Prumbaum, S. Raunser, and P. Bieling. 2024. Molecular mechanism of actin filament elongation by formins. *Science* 384(6692):eadn9560. doi:10.1126/science.adn9560.

Özdemir, A., B. İbişoğlu, Y. D. Şimay Demir, E. Benhür, F. Valipour, and M. Ark. 2021. A novel proteolytic cleavage of ROCK 1 in cell death: Not only by caspases 3 and 7 but also by caspase 2. *Biochemical and biophysical research communications* 547:118–124. doi:10.1016/j.bbrc.2021.02.024.

Palamidessi, A., E. Frittoli, M. Garré, M. Faretta, M. Mione, I. Testa, A. Diaspro, L. Lanzetti, G. Scita, and P. P. Di Fiore. 2008. Endocytic trafficking of Rac is required for the spatial restriction of signaling in cell migration. *Cell* 134(1):135–147. doi:10.1016/j.cell.2008.05.034.

Pearl, J. 2013. Causality. Cambridge University Press.

Pertz, O., L. Hodgson, R. L. Klemke, and K. M. Hahn. 2006. Spatiotemporal dynamics of RhoA activity in migrating cells. *Nature* 440(7087):1069–1072. doi:10.1038/nature04665.

PhD Thesis Melanie Graessl. 2015. Dynamic regulation of Rho GTPase networks and correlation with effector pathways. PhD Thesis.

Pineau, J., L. Pinon, O. Mesdjian, J. Fattaccioli, A.-M. Lennon Duménil, and P. Pierobon. 2022. Microtubules restrict F-actin polymerization to the immune synapse via GEF-H1 to maintain polarity in lymphocytes. *eLife* 11. doi:10.7554/eLife.78330.

Pinner, S., and E. Sahai. 2008. PDK1 regulates cancer cell motility by antagonising inhibition of ROCK1 by RhoE. *Nature cell biology* 10(2):127–137. doi:10.1038/ncb1675.

Pollard, T. D., and G. G. Borisy. 2003. Cellular Motility Driven by Assembly and Disassembly of Actin Filaments. *Cell* 112(4):453–465. doi:10.1016/S0092-8674(03)00120-X.

Ponti, A., M. Machacek, S. L. Gupton, C. M. Waterman-Storer, and G. Danuser. 2004. Two distinct actin networks drive the protrusion of migrating cells. *Science* 305(5691):1782–1786. doi:10.1126/science.1100533.

Powis, G., E. J. Meuillet, M. Indarte, G. Booher, and L. Kirkpatrick. 2023. Pleckstrin Homology PH domain, structure, mechanism, and contribution to human disease. *Biomedicine & pharmacotherapy = Biomedecine & pharmacotherapie* 165:115024. doi:10.1016/j.biopha.2023.115024.

Raouf A. Khalil. 2010. Rho Kinase in Vascular Smooth Muscle. In Regulation of Vascular Smooth Muscle Function. R. A. Khalil, editor. Morgan & Claypool Life Sciences.

Rayment, I., H. M. Holden, M. Whittaker, C. B. Yohn, M. Lorenz, K. C. Holmes, and R. A. Milligan. 1993. Structure of the actin-myosin complex and its implications for muscle contraction. *Science* 261(5117):58–65. doi:10.1126/science.8316858.

Ren, X. D., W. B. Kiosses, and M. A. Schwartz. 1999. Regulation of the small GTP-binding protein Rho by cell adhesion and the cytoskeleton. *The EMBO journal* 18(3):578–585. doi:10.1093/emboj/18.3.578.

Rhee, S., H. Jiang, C.-H. Ho, and F. Grinnell. 2007. Microtubule function in fibroblast spreading is modulated according to the tension state of cell-matrix interactions. *Proceedings of the National Academy of Sciences of the United States of America* 104(13):5425–5430. doi:10.1073/pnas.0608030104.

Ridley, A. J. 2011. Life at the leading edge. *Cell* 145(7):1012–1022. doi:10.1016/j.cell.2011.06.010.

Ridley, A. J. 2015. Rho GTPase signalling in cell migration. *Current Opinion in Cell Biology* 36:103–112. doi:10.1016/j.ceb.2015.08.005.

Riento, K., R. M. Guasch, R. Garg, B. Jin, and A. J. Ridley. 2003. RhoE binds to ROCK I and inhibits downstream signaling. *Molecular and cellular biology* 23(12):4219–4229. doi:10.1128/MCB.23.12.4219-4229.2003.

Riento, K., and A. J. Ridley. 2006. Inhibition of ROCK by RhoE. *Methods in enzymology* 406:533–541. doi:10.1016/S0076-6879(06)06041-1.

Riou, P., S. Kjær, R. Garg, A. Purkiss, R. George, R. J. Cain, G. Bineva, N. Reymond, B. McColl, A. J. Thompson, N. O'Reilly, N. Q. McDonald, P. J. Parker, and A. J. Ridley. 2013. 14-3-3 proteins interact with a hybrid prenyl-phosphorylation motif to inhibit G proteins. *Cell* 153(3):640–653. doi:10.1016/j.cell.2013.03.044.

Riou, P., P. Villalonga, and A. J. Ridley. 2010. Rnd proteins: multifunctional regulators of the cytoskeleton and cell cycle progression. *BioEssays news and reviews in molecular, cellular and developmental biology* 32(11):986–992. doi:10.1002/bies.201000060.

Romero, S., C. Le Clainche, D. Didry, C. Egile, D. Pantaloni, and M.-F. Carlier. 2004. Formin is a processive motor that requires profilin to accelerate actin assembly and associated ATP hydrolysis. *Cell* 119(3):419–429. doi:10.1016/j.cell.2004.09.039.

Sackett, D. L., and J. K. Varma. 1993. Molecular mechanism of colchicine action: induced local unfolding of beta-tubulin. *Biochemistry* 32(49):13560–13565. doi:10.1021/bi00212a023.

Saez-Rodriguez, J., A. MacNamara, and S. Cook. 2015. Modeling Signaling Networks to Advance New Cancer Therapies. *Annual review of biomedical engineering* 17:143–163. doi:10.1146/annurev-bioeng-071813-104927.

Saha, S., T. L. Nagy, and O. D. Weiner. 2018. Joining forces: crosstalk between biochemical signalling and physical forces orchestrates cellular polarity and dynamics. *Philosophical transactions of the Royal Society of London. Series B, Biological sciences* 373(1747). doi:10.1098/rstb.2017.0145.

Salmerón-Sánchez, M., and M. J. Dalby. 2016. Synergistic growth factor microenvironments. *Chemical communications (Cambridge, England)* 52(91):13327–13336. doi:10.1039/c6cc06888j.

Sampayo, R. G., M. Sakamoto, M. Wang, S. Kumar, and D. V. Schaffer. 2023. Mechanosensitive stem cell fate choice is instructed by dynamic fluctuations in activation of Rho GTPases. *Proceedings of the National Academy of Sciences of the United States of America* 120(22):e2219854120. doi:10.1073/pnas.2219854120.

Scarpa, E., and R. Mayor. 2016. Collective cell migration in development. *J Cell Biol* 212(2):143–155. doi:10.1083/jcb.201508047.

Schaefer, A., N. R. Reinhard, and P. L. Hordijk. 2014. Toward understanding RhoGTPase specificity: structure, function and local activation. *Small GTPases* 5(2):6. doi:10.4161/21541248.2014.968004.

Schmidt, C. J., and S. J. Stehbens. 2024. Microtubule control of migration: Coordination in confinement. *Current Opinion in Cell Biology* 86:102289. doi:10.1016/j.ceb.2023.102289.

Schmitt, C., P. Mauker, N. A. Vepřek, C. Gierse, J. C. M. Meiring, J. Kuch, A. Akhmanova, L. Dehmelt, and O. Thorn-Seshold. 2024. A Photocaged Microtubule-Stabilising Epothilone Allows Spatiotemporal Control of Cytoskeletal Dynamics. *Angewandte Chemie (International ed. in English)* 63(43):e202410169. doi:10.1002/anie.202410169.

Schönichen, A., H. G. Mannherz, E. Behrmann, A. J. Mazur, S. Kühn, U. Silván, C.-A. Schoenenberger, O. T. Fackler, S. Raunser, L. Dehmelt, and M. Geyer. 2013. FHOD1 is a combined actin filament capping and bundling factor that selectively associates with actin arcs and stress fibers. *J Cell Sci* 126(Pt 8):1891–1901. doi:10.1242/jcs.126706.

Seetharaman, S., and S. Etienne-Manneville. 2020. Cytoskeletal Crosstalk in Cell Migration. *Trends in Cell Biology* 30(9):720–735. doi:10.1016/j.tcb.2020.06.004.

Seger, R., and E. G. Krebs. 1995. The MAPK signaling cascade. *FASEB journal official publication of the Federation of American Societies for Experimental Biology* 9(9):726–735. https://pubmed.ncbi.nlm.nih.gov/7601337/.

Seze, J. de, M. Bongaerts, B. Boulevard, and M. Coppey. 2025. Optogenetic control of a GEF of RhoA uncovers a signaling switch from retraction to protrusion. *eLife* 12. doi:10.7554/eLife.93180.

Seze, J. de, J. Gatin, and M. Coppey. 2023. RhoA regulation in space and time. *FEBS Letters* 597(6):836–849. doi:10.1002/1873-3468.14578.

Shakiba, D., F. Alisafaei, A. Savadipour, R. A. Rowe, Z. Liu, K. M. Pryse, V. B. Shenoy, E. L. Elson, and G. M. Genin. 2020. The Balance between Actomyosin Contractility and Microtubule Polymerization Regulates Hierarchical Protrusions That Govern Efficient Fibroblast-Collagen Interactions. *ACS nano* 14(7):7868–7879. doi:10.1021/acsnano.9b09941.

Sidor, C., T. J. Stevens, L. Jin, J. Boulanger, and K. Röper. 2020. Rho-Kinase Planar Polarization at Tissue Boundaries Depends on Phospho-regulation of Membrane Residence Time. *Developmental Cell* 52(3):364-378.e7. doi:10.1016/j.devcel.2019.12.003.

Smith, R. C., W. Z. Cande, R. Craig, P. J. Tooth, J. M. Scholey, and J. Kendrick-Jones. 1983. Regulation of myosin filament assembly by light-chain phosphorylation. *Philosophical transactions of the Royal Society of London. Series B, Biological sciences* 302(1108):73–82. doi:10.1098/rstb.1983.0039.

Spencer, D. M., T. J. Wandless, S. L. Schreiber, and G. R. Crabtree. 1993. Controlling signal transduction with synthetic ligands. *Science* 262(5136):1019–1024. doi:10.1126/science.7694365.

Spudich, J. A. 2001. The myosin swinging cross-bridge model. *Nature reviews. Molecular cell biology* 2(5):387–392. doi:10.1038/35073086.

Stanoev, A., A. Mhamane, K. C. Schuermann, H. E. Grecco, W. Stallaert, M. Baumdick, Y. Brüggemann, M. S. Joshi, P. Roda-Navarro, S. Fengler, R. Stockert, L. Roßmannek, J. Luig, A. Koseska, and P. I. H. Bastiaens. 2018. Interdependence between EGFR and Phosphatases Spatially Established by Vesicular Dynamics Generates a Growth Factor Sensing and Responding Network. *Cell Systems* 7(3):295-309.e11. doi:10.1016/j.cels.2018.06.006.

Stanoev, A., C. Schröter, and A. Koseska. 2021. Robustness and timing of cellular differentiation through population-based symmetry breaking. *Development (Cambridge, England)* 148(3). doi:10.1242/dev.197608.

Stehbens, S., and T. Wittmann. 2012. Targeting and transport: how microtubules control focal adhesion dynamics. *J Cell Biol* 198(4):481–489. doi:10.1083/jcb.201206050.

Svitkina, T. M. 2020. Actin Cell Cortex: Structure and Molecular Organization. *Trends in Cell Biology* 30(7):556–565. doi:10.1016/j.tcb.2020.03.005.

Sweeney, H. L., and A. Houdusse. 2010. Structural and functional insights into the Myosin motor mechanism. *Annual review of biophysics* 39:539–557. doi:10.1146/annurev.biophys.050708.133751.

Totsukawa, G., Y. Wu, Y. Sasaki, D. J. Hartshorne, Y. Yamakita, S. Yamashiro, and F. Matsumura. 2004. Distinct roles of MLCK and ROCK in the regulation of membrane protrusions and focal adhesion dynamics during cell migration of fibroblasts. *J Cell Biol* 164(3):427–439. doi:10.1083/jcb.200306172.

Truebestein, L., D. J. Elsner, E. Fuchs, and T. A. Leonard. 2015. A molecular ruler regulates cytoskeletal remodelling by the Rho kinases. *Nat Commun* 6(1):10029. doi:10.1038/ncomms10029.

Truebestein, L., and T. A. Leonard. 2016. Coiled-coils: The long and short of it. *BioEssays news and reviews in molecular, cellular and developmental biology* 38(9):903–916. doi:10.1002/bies.201600062.

Truong Quang, B. an, R. Peters, D. A. D. Cassani, P. Chugh, A. G. Clark, M. Agnew, G. Charras, and E. K. Paluch. 2021. Extent of myosin penetration within the actin cortex regulates cell surface mechanics. *Nat Commun* 12(1):6511. doi:10.1038/s41467-021-26611-2.

Trybus, K. M., T. W. Huiatt, and S. Lowey. 1982. A bent monomeric conformation of myosin from smooth muscle. *Proceedings of the National Academy of Sciences of the United States of America* 79(20):6151–6155. doi:10.1073/pnas.79.20.6151.

Tu, D., Y. Li, H. K. Song, A. V. Toms, C. J. Gould, S. B. Ficarro, J. A. Marto, B. L. Goode, and M. J. Eck. 2011. Crystal structure of a coiled-coil domain from human ROCK I. *PloS one* 6(3):e18080. doi:10.1371/journal.pone.0018080.

Tyson, J. J., K. C. Chen, and B. Novak. 2003. Sniffers, buzzers, toggles and blinkers: dynamics of regulatory and signaling pathways in the cell. *Current Opinion in Cell Biology* 15(2):221–231. doi:10.1016/S0955-0674(03)00017-6.

UMBARGER, H. E. 1961. Feedback control by endproduct inhibition. *Cold Spring Harbor symposia on quantitative biology* 26:301–312. doi:10.1101/sqb.1961.026.01.036.

Vemula, V., T. Huber, M. Ušaj, B. Bugyi, and A. Månsson. 2021. Myosin and gelsolin cooperate in actin filament severing and actomyosin motor activity. *Journal of Biological Chemistry* 296:100181. doi:10.1074/jbc.RA120.015863.

Vetter, I. R., and A. Wittinghofer. 2001. The Guanine Nucleotide-Binding Switch in Three Dimensions. *American Association for the Advancement of Science,* 9/11/2001. https://www.science.org/doi/10.1126/science.1062023?url_ver=Z39.88-2003&rfr_id=ori:rid:crossref.org&rfr_dat=cr_pub%20%200pubmed. Accessed 07/09/2025.

Vicente-Manzanares, M., and A. R. Horwitz. 2010. Myosin light chain mono- and di-phosphorylation differentially regulate adhesion and polarity in migrating cells. *Biochemical and biophysical research communications* 402(3):537–542. doi:10.1016/j.bbrc.2010.10.071.

Vogel, S. K., Z. Petrasek, F. Heinemann, and P. Schwille. 2013. Myosin motors fragment and compact membrane-bound actin filaments. *eLife Sciences Publications, Ltd,* 8/1/2013. https://elifesciences.org/articles/00116?utm_source=chatgpt.com. Accessed 10/06/2025.

Wang, H., M. Vilela, A. Winkler, M. Tarnawski, I. Schlichting, H. Yumerefendi, B. Kuhlman, R. Liu, G. Danuser, and K. M. Hahn. 2016. LOVTRAP: an optogenetic system for photoinduced protein dissociation. *Nature methods* 13(9):755–758. doi:10.1038/nmeth.3926.

Wani, M. C., H. L. Taylor, M. E. Wall, P. Coggon, and A. T. McPhail. 1971. Plant antitumor agents. VI. The isolation and structure of taxol, a novel antileukemic and antitumor agent from Taxus brevifolia. *Journal of the American Chemical Society* 93(9):2325–2327. doi:10.1021/ja00738a045.

Wartmann, M., and K.-H. Altmann. 2002. The biology and medicinal chemistry of epothilones. *Current medicinal chemistry. Anti-cancer agents* 2(1):123–148. doi:10.2174/1568011023354489.

Watanabe, G., Y. Saito, P. Madaule, T. Ishizaki, K. Fujisawa, N. Morii, H. Mukai, Y. Ono, A. Kakizuka, and S. Narumiya. 1996. Protein kinase N (PKN) and PKN-related protein rhophilin as targets of small GTPase Rho. *Science* 271(5249):645–648. doi:10.1126/science.271.5249.645.

Watanabe, N., and T. J. Mitchison. 2002. Single-Molecule Speckle Analysis of Actin Filament Turnover in Lamellipodia. *American Association for the Advancement of Science,*

8/2/2002. https://www.science.org/doi/10.1126/science.1067470?url_ver=Z39.88-2003&rfr_id=ori:rid:crossref.org&rfr_dat=cr_pub%20%200pubmed. Accessed 07/09/2025.

Waterman-Storer, C. M., R. A. Worthylake, B. P. Liu, K. Burridge, and E. D. Salmon. 1999. Microtubule growth activates Rac1 to promote lamellipodial protrusion in fibroblasts. *Nature cell biology* 1(1):45–50. doi:10.1038/9018.

Wegner, A. 1976. Head to tail polymerization of actin. *Journal of molecular biology* 108(1):139–150. doi:10.1016/s0022-2836(76)80100-3.

Wen, W., W. Liu, J. Yan, and M. Zhang. 2008. Structure basis and unconventional lipid membrane binding properties of the PH-C1 tandem of rho kinases. *The Journal of biological chemistry* 283(38):26263–26273. doi:10.1074/jbc.M803417200.

Wennerberg, K., K. L. Rossman, and C. J. Der. 2005. The Ras superfamily at a glance. *J Cell Sci* 118(Pt 5):843–846. doi:10.1242/jcs.01660.

Wollrab, V., J. M. Belmonte, L. Baldauf, M. Leptin, F. Nédeléc, and G. H. Koenderink. 2018. Polarity sorting drives remodeling of actin-myosin networks. *J Cell Sci* 132(4). doi:10.1242/jcs.219717.

Wozniak, M. A., and C. S. Chen. 2009. Mechanotransduction in development: a growing role for contractility. *Nat Rev Mol Cell Biol* 10(1):34–43. doi:10.1038/nrm2592.

Zalewski, J. K., J. H. Mo, S. Heber, A. Heroux, R. G. Gardner, J. D. Hildebrand, and A. P. VanDemark. 2016. Structure of the Shroom-Rho Kinase Complex Reveals a Binding Interface with Monomeric Shroom That Regulates Cell Morphology and Stimulates Kinase Activity*. *The Journal of biological chemistry* 291(49):25364–25374. doi:10.1074/jbc.M116.738559.

Zheng, Y. 2001. Dbl family guanine nucleotide exchange factors. *Trends in Biochemical Sciences* 26(12):724–732. doi:10.1016/S0968-0004(01)01973-9.

# 10 Supplement

## 10.1 Supplementary figures

### 10.1.1 Validation of CMV-mCitrine-GEF-H1C53R

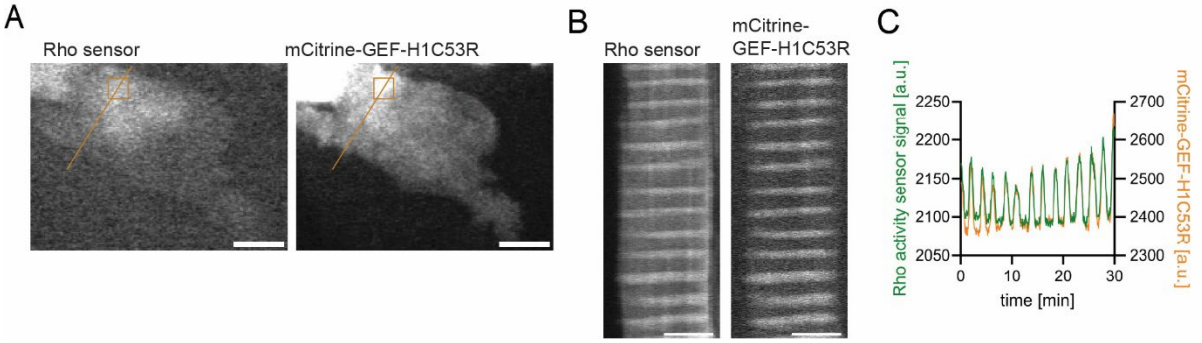


*FigureS 1: Validation of new mCitrine-GEF-H1C53R. (A) Representative TIRF images of cells expressing rhotekin-based Rho activity sensor (mCherry) and mCitrine-GEF-H1. (B) Kymographs corresponding to lines in A. (C) Fluorescence signals within rectangular regions of interest in A.*

### 10.1.2 LOVTRAP release of CA-ROCK1 tends to reduce network activity in adherent mammalian cells

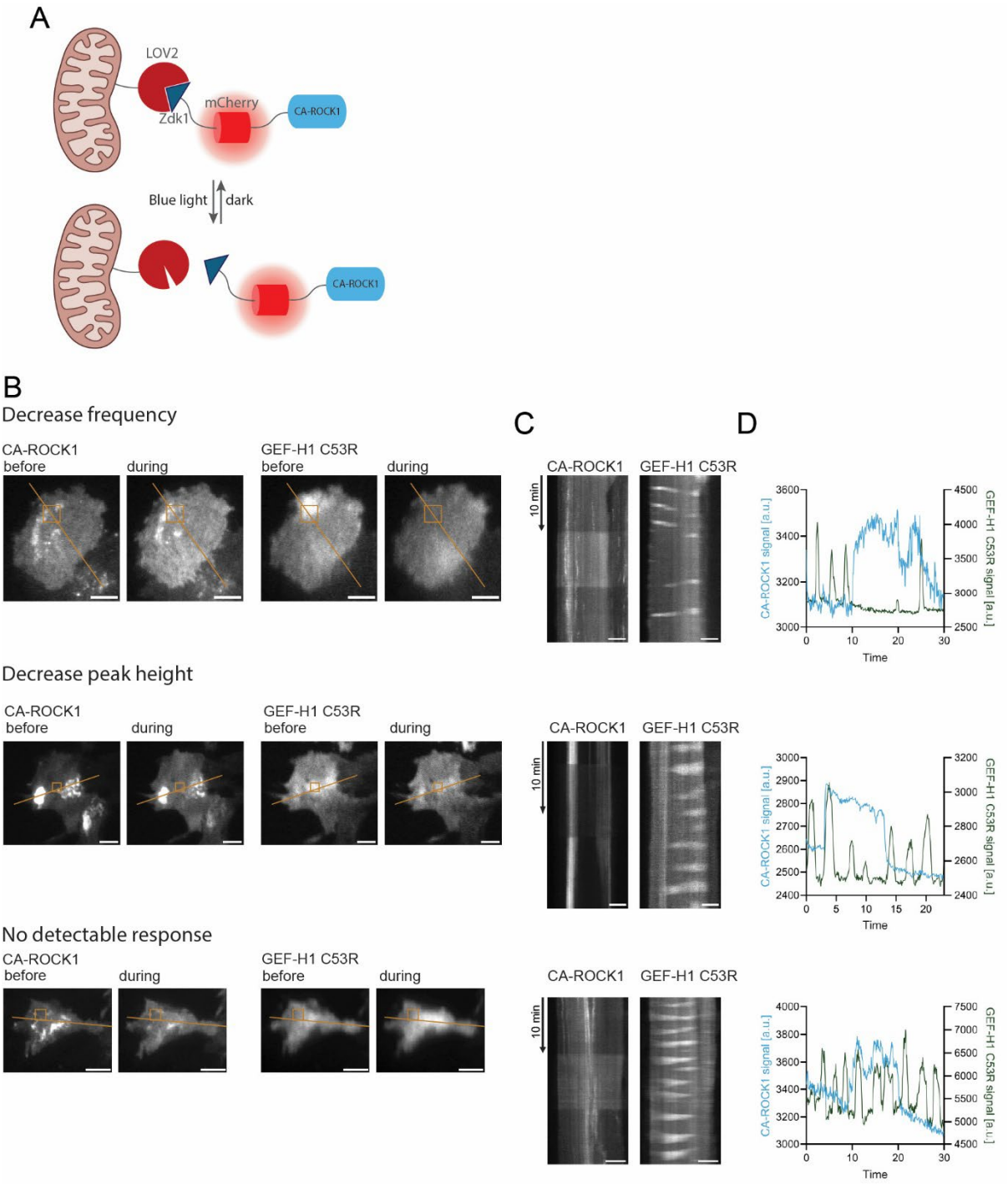


*FigureS 2: Light induced release of mitochondria bound CA-ROCK1 tends to decrease GEF-H1 C53R network dynamics at the plasma membrane in adherent mammalian cells. (A) Schematic of the LOVTRAP method. Without light illumination, the light oxygen voltage (LOV) domain anchored to mitochondria serves as trap for the Zdk1-linked protein of interest (here: CA-ROCK1) to sequester the protein from the cytosol. Upon illumination with blue light, the Zdk1-mCherry-CA-ROCK1 is released from mitochondria due to a conformation change within the LOV domain. The cytosolic CA-ROCK1 can now activate effectors. If light illumination is stopped, the conformation of the LOV domain reverts to the dark state and Zdk1-mCherry-CA-ROCK1 gets*

*trapped again. (B) Representative TIRF images of cells expressing pTriEx-NTOM20-GS-moxBFP-cc-GS-LOV2 as mitochondrial anchor, Zdk1-mCherry-CA-ROCK1 (left) as perturbation construct and mCitrine-GEF-H1 (right) as readout. As indicated, the response of the cell contraction signal network varied from cell to cell upon CA-ROCK1 release: (B) Kymographs corresponding to lines in A. (C) Fluorescence signals within rectangular regions of interest in A. Scale bar: 10 µm.*

## 10.2 Supplementary tables

### 10.2.1 Transfection plans main experiments

*Table 21: Transfection plan functionalized MAP experiment w/ GEF-H1 C53R and different mPHC1 ROCK1 variants.*

| Plasmid | m [ng] | DNA_total [ng] | lipofectamine 2000 [µl] | OptiMEM [µl] |
|---|---|---|---|---|
| 338_mCitrine-PARC | 650 | 1150 | 2,875 | 95,8 |
| 385_mTurquoise2-NES-eDHFR-GEF-H1 C53R | 250 | | | |
| 860_ pDEST-CMV-N-mCherry | 250 | | | |
| | | | | |
| 338_mCitrine-PARC | 650 | 1150 | 2,875 | 95,8 |
| 385_mTurquoise2-NES-eDHFR-GEF-H1 C53R | 250 | | | |
| 942_CMV-mCherry-attB1-3GS-E-mPHC1ROCK1-attB2 | 250 | | | |
| | | | | |
| 338_mCitrine-PARC | 650 | 1150 | 2,875 | 95,8 |
| 385_mTurquoise2-NES-eDHFR-GEF-H1 C53R | 250 | | | |
| 952_CMV-mCherry-mPHC1ROCK1-F1174A-L1199A-E1203K-A1292R | 250 | | | |

*Table 22: Transfection plan functionalized MAP experiment w/ different ROCK1 perturbation variants and Myosin IIa as readout.*

| Plasmid | m [ng] | DNA_total [ng] | lipofectamine 2000 [µl] | OptiMEM [µl] |
|---|---|---|---|---|
| 338_mCitrine-PARC | 650 | 1200 | 3 | 100,0 |
| 974_CMV-mTur2-ROCK1-eDHFR | 300 | | | |
| 748_mCherry-NMHC2a (human) | 250 | | | |
| | | | | |
| 338_mCitrine-PARC | 650 | 1200 | 3 | 100,0 |
| 999_CMV-mTur2-ROCK1ΔPHC1-eDHFR | 300 | | | |
| 748_mCherry-NMHC2a (human) | 250 | | | |
| | | | | |
| 338_mCitrine-PARC | 650 | 1200 | 3 | 100,0 |
| 986_CMV-mTur2-ROCK1PHmutC-eDHFR | 300 | | | |
| 748_mCherry-NMHC2a (human) | 250 | | | |

*Table 23: Transfection plan CA-MAP with ROCK1 perturbation and Rho sensor, Myosin IIa, or Actin as readout.*

| Plasmid | m [ng] | DNA_total [ng] | lipofectamine 2000 [µl] | OptiMEM [µl] |
|---|---|---|---|---|
| 338_mCitrine-PARC | 150 | 350 | 0,875 | 29,2 |
| 388_mTur2-NES-L-eDHFR | 100 | | | |
| 229_delCMV-mCherry-RBD | 100 | | | |
| | | | | |
| 338_mCitrine-PARC | 150 | 350 | 0,875 | 29,2 |
| 974_CMV-mTur2-ROCK1-eDHFR | 100 | | | |
| 748_mCherry-NMHC2a (human) | 100 | | | |
| | | | | |
| 338_mCitrine-PARC | 150 | 350 | 0,875 | 29,2 |
| 974_CMV-mTur2-ROCK1-eDHFR | 100 | | | |
| 95_pmCherry-actin-UB | 100 | | | |

*Table 24: Transfection plan Pulse experiment with ROCK1 wild type, ROCK1mutRBD, and ROCK1mutRBDPHmutC and GEF-H1 C53R for cell contraction network stimulation and as readout.*

| Plasmid | m [ng] | DNA_total [ng] | lipofectamine 2000 [µl] | OptiMEM [µl] |
|---|---|---|---|---|
| 929_CMV-mCitrine_GEF-H1 C53R | 150 | 290 | 0,725 | 24,2 |
| 860_ pDEST-CMV-N-mCherry | 140 | | | |
| | | | | |
| 929_CMV-mCitrine_GEF-H1 C53R | 150 | 290 | 0,725 | 24,2 |
| 912_CMV-mCherry-attB1-ROCKI-attB2 | 140 | | | |
| | | | | |
| 929_CMV-mCitrine_GEF-H1 C53R | 150 | 290 | 0,725 | 24,2 |
| 992_CMV-mCherry-attB1-ROCKImutRBD-attB2 | 140 | | | |
| | | | | |
| 929_CMV-mCitrine_GEF-H1 C53R | 150 | 290 | 0,725 | 24,2 |
| 994_CMV-mCherry-attB1-ROCKIPHmutCmutRBD-attB2 | 140 | | | |

*Table 25: Transfection plan Pulse experiment with CA-ROCK1 and GEF-H1 C53R for cell contraction network stimulation and as readout.*

| Plasmid | m [ng] | DNA_total [ng] | lipofectamine 2000 [µl] | OptiMEM [µl] |
|---|---|---|---|---|
| 929_CMV-mCitrine_GEF-H1 C53R | 150 | 290 | 0,725 | 24,2 |
| 860_ pDEST-CMV-N-mCherry | 140 | | | |
| | | | | |
| 929_CMV-mCitrine_GEF-H1 C53R | 150 | 290 | 0,725 | 24,2 |
| 922_CMV-mCherry-attB1-ROCKID4-attB2 | 140 | | | |

*Table 26: Transfection plan Myosin II response experiment to CA-ROCK1 over expression.*

| Plasmid | m [ng] | DNA_total [ng] | lipofectamine 2000 [µl] | OptiMEM [µl] |
|---|---|---|---|---|
| 749_mCitrine-NMHC2a (human) | 100 | 240 | 0,6 | 20,0 |
| 860_ pDEST-CMV-N-mCherry | 140 | | | |
| | | | | |
| 749_mCitrine-NMHC2a (human) | 100 | 240 | 0,6 | 20,0 |
| 922_CMV-mCherry-attB1-ROCKID4-attB2 | 140 | | | |

### 10.2.2 Parameters Network simulations

*Table 27: Michaelis constants. Values obtained by Bayesian fitting approach from Kamps et al. (2020)(Kamps et al., 2020).*

| Michaelis constants in 10^6 molecules/cell | Value |
|---|---|
| Km0 | 2.423 |
| Km1 | 2.423 |
| Km2 | 0.075 |
| Km3 | 1.000 |
| Km4 | 1.000 |
| Km5 | 0.014 |
| Km6 | 0.786 |
| Km7 | 1.000 |

*Table 28: Rate constants. Values obtained by Bayesian fitting approach from Kamps et al. (2020)(Kamps et al., 2020). Values changed for simulation of Myosin II feedback independent activation by CA-ROCK1 and ROCK inhibition are bold.*

| rate constants | Value CA-ROCK1 | Values Myosin Inhibition 1 | Values Myosin Inhibition 2 | Values ROCK inhibition |
|---|---|---|---|---|
| k0 | 3.88*Km0 | 3.88*Km0 | 3.88*Km0 | 3.88*Km0 |
| k1 | 0 | 0 | 0 | 0 |
| k2 | 2.036*Km2 | 2.036*Km2 | 2.036*Km2 | 2.036*Km2 |
| k3 | 1.195 | 1.195 | 1.195 | 1.195 |
| k4 | 3.982 | 3.982 | 3.982 | 3.982 |
| k5 | 0.417*Km5 | 0.417*Km5 | 0.417*Km5 | **0.417*Km5*(1-F)** |
| k6 | 0.005*Km6 | 0.005*Km6 | 0.005*Km6 | 0.005*Km6 |
| k7 | **F** | 0 | 0 | 0 |
| F | **0:0.2:6*10^4** | | | **0.0:0.02:1.0** |

*Table 29: Concentration of the molecules in cells. Values obtained by Bayesian fitting approach from Kamps et al. (2020)(Kamps et al., 2020) for GEF-H1 concentration (G(t)). Rho (R(t)) and Myosin (M(t)) concentrations are constant and based on Beck et al (2011)(Beck et al., 2011). Values changed for simulation of Myosin inhibition are bold.*

| Concentrations in 10^6 molecules/cell | Value CA-ROCK1 | Values Myosin Inhibition 1 | Values Myosin Inhibition 2 | Values ROCK inhibition |
|---|---|---|---|---|
| R(t) | 0.443 | 0.443 | 0.443 | 0.443 |
| M(t) | 1.240 | **1.24*(1-F)** | **1.24*(1-F)** | 1.240 |
| G(t) | 0.300 | 0.300 | 0.300 | 0.300 |
| F | | **0.0:0.05:1.0** | **0.8:0.01:1.0** | |

technische universität
dortmund

Fakultät für Chemie
und Chemische Biologie

Datum: 07.11.2025

An die/den Vorsitzende/n des Promotionsausschusses
der Fakultät für Chemie und Chemische Biologie der TU Dortmund

## Eigenständigkeitserklärung für Dissertationen

nach der Ergänzung zur Promotionsordnung vom 29.10.2010
(Promotionsstudiengang) am 20.11.2023

Ich versichere hiermit an Eides statt, dass ich die vorliegende Dissertation mit dem folgenden Titel

Transduction and feedback regulation in morphodynamic signaling networks

selbstständig und ohne unzulässige fremde Hilfe verfasst habe. Ich habe keine anderen als die angegebenen Quellen und Hilfsmittel benutzt sowie wörtliche und sinngemäße Zitate kenntlich gemacht. Ich erkläre zudem, dass ich beim Einsatz von Schreib- und Bildwerkzeugen, die durch Künstliche Intelligenz (KI) unterstützt werden, diese in der Übersicht verwendeter Hilfsmittel mit ihrem Produktnamen, meiner Bezugsquelle sowie der spezifischen Methodik vollständig aufgeführt habe und, bei Übernahme von durch generative Schreibwerkzeuge erstellten Texten, die betreffenden Textstellen in der Arbeit als mit KI-generierter Unterstützung verfasst gekennzeichnet habe. Die Arbeit hat in gleicher oder ähnlicher Form noch keiner Prüfungsbehörde vorgelegen. Ich habe sichergestellt, dass durch die Verwendung generativer Modelle kein fremdes geistiges Eigentum verletzt wurde und ich kein wissenschaftliches Fehlverhalten etwa in Form von Plagiaten begangen habe.

Name: Gierse, Vorname Carolin

Matrikelnummer: 176096

Datum, Unterschrift _____

# Eidesstattliche Versicherung (Affidavit)

Gierse, Carolin
Name, Vorname
(Surname, first name)

176096
Matrikel-Nr.
(Enrolment number)

Belehrung:

Wer vorsätzlich gegen eine die Täuschung über Prüfungsleistungen betreffende Regelung einer Hochschulprüfungsordnung verstößt, handelt ordnungswidrig. Die Ordnungswidrigkeit kann mit einer Geldbuße von bis zu 50.000,00 € geahndet werden. Zuständige Verwaltungsbehörde für die Verfolgung und Ahndung von Ordnungswidrigkeiten ist der Kanzler/die Kanzlerin der Technischen Universität Dortmund. Im Falle eines mehrfachen oder sonstigen schwerwiegenden Täuschungsversuches kann der Prüfling zudem exmatrikuliert werden, § 63 Abs. 5 Hochschulgesetz NRW.

Die Abgabe einer falschen Versicherung an Eides statt ist strafbar.

Wer vorsätzlich eine falsche Versicherung an Eides statt abgibt, kann mit einer Freiheitsstrafe bis zu drei Jahren oder mit Geldstrafe bestraft werden, § 156 StGB. Die fahrlässige Abgabe einer falschen Versicherung an Eides statt kann mit einer Freiheitsstrafe bis zu einem Jahr oder Geldstrafe bestraft werden, § 161 StGB.

Die oben stehende Belehrung habe ich zur Kenntnis genommen:

Official notification:

Any person who intentionally breaches any regulation of university examination regulations relating to deception in examination performance is acting improperly. This offence can be punished with a fine of up to EUR 50,000.00. The competent administrative authority for the pursuit and prosecution of offences of this type is the chancellor of the TU Dortmund University. In the case of multiple or other serious attempts at deception, the candidate can also be unenrolled, Section 63, paragraph 5 of the Universities Act of North Rhine-Westphalia.

The submission of a false affidavit is punishable.

Any person who intentionally submits a false affidavit can be punished with a prison sentence of up to three years or a fine, Section 156 of the Criminal Code. The negligent submission of a false affidavit can be punished with a prison sentence of up to one year or a fine, Section 161 of the Criminal Code.

I have taken note of the above official notification.

Dortmund, 07.11.2025
Ort, Datum
(Place, date)

Unterschrift
(Signature)

Titel der Dissertation:
(Title of the thesis):

Transduction and feedback regulation in morphodynamic signaling networks

Ich versichere hiermit an Eides statt, dass ich die vorliegende Dissertation mit dem Titel selbstständig und ohne unzulässige fremde Hilfe angefertigt habe. Ich habe keine anderen als die angegebenen Quellen und Hilfsmittel benutzt sowie wörtliche und sinngemäße Zitate kenntlich gemacht.
Die Arbeit hat in gegenwärtiger oder in einer anderen Fassung weder der TU Dortmund noch einer anderen Hochschule im Zusammenhang mit einer staatlichen oder akademischen Prüfung vorgelegen.

I hereby swear that I have completed the present dissertation independently and without inadmissible external support. I have not used any sources or tools other than those indicated and have identified literal and analogous quotations.

The thesis in its current version or another version has not been presented to the TU Dortmund University or another university in connection with a state or academic examination.*

*Please be aware that solely the German version of the affidavit ("Eidesstattliche Versicherung") for the PhD thesis is the official and legally binding version.

Dortmund, 07.11.2025
Ort, Datum
(Place, date)

Unterschrift
(Signature)